

## INFORMATION TO USERS

This manuscript has been reproduced from the microfilm master. UMI films the text directly from the original or copy submitted. Thus, some thesis and dissertation copies are in typewriter face, while others may be from any type of computer printer.

**The quality of this reproduction is dependent upon the quality of the copy submitted.** Broken or indistinct print, colored or poor quality illustrations and photographs, print bleedthrough, substandard margins, and improper alignment can adversely affect reproduction.

In the unlikely event that the author did not send UMI a complete manuscript and there are missing pages, these will be noted. Also, if unauthorized copyright material had to be removed, a note will indicate the deletion.

Oversize materials (e.g., maps, drawings, charts) are reproduced by sectioning the original, beginning at the upper left-hand corner and continuing from left to right in equal sections with small overlaps. Each original is also photographed in one exposure and is included in reduced form at the back of the book.

Photographs included in the original manuscript have been reproduced xerographically in this copy. Higher quality 6" x 9" black and white photographic prints are available for any photographs or illustrations appearing in this copy for an additional charge. Contact UMI directly to order.

# UMI

A Bell & Howell Information Company  
300 North Zeeb Road, Ann Arbor MI 48106-1346 USA  
313/761-4700 800/521-0600



UNIVERSITY OF OKLAHOMA  
GRADUATE COLLEGE

**FLUID FLOW DIAGNOSTICS USING RAINBOW  
SCHLIEREN IMAGING AND COMPUTER  
TOMOGRAPHY**

A Dissertation  
SUBMITTED TO THE GRADUATE FACULTY  
In partial fulfillment of the requirements for the  
degree of  
Doctor of Philosophy

By  
NELSON K. BUTUK  
Norman, Oklahoma  
1997

**UMI Number: 9721056**

---

**UMI Microform 9721056**  
**Copyright 1997, by UMI Company. All rights reserved.**

**This microform edition is protected against unauthorized  
copying under Title 17, United States Code.**


---

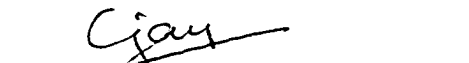
**UMI**  
**300 North Zeeb Road**  
**Ann Arbor, MI 48103**

# FLUID FLOW DIAGNOSTICS USING RAINBOW SCHLIEREN IMAGING AND COMPUTER TOMOGRAPHY

A Dissertation APPROVED FOR THE SCHOOL OF AEROSPACE AND  
MECHANICAL ENGINEERING

BY

  
Gollahalli, S. R. (Chairman)

  
Agrawal, A. K. (Co-Chairman)

  
Nollert, U. Matthias

  
Parthasarathy, N. Ramkumar

  
Rasmussen, L. Maurice

© Copyright Nelson Butuk 1997  
All Rights Reserved

## ABSTRACT

Quantitative analysis of 3-D flow fields by rainbow schlieren deflectometry is presented. The method is based on the measurement of the deflection of collimated light rays due to the gradients in the refractive index of the test flow field. In this method, the schlieren apparatus is modified by replacing the knife edge with a computer-generated continuously-graded color (rainbow) filter. This modification results in the refractive index gradients appearing in the schlieren image as gradations in color rather than irradiance.

The deflections obtained from rainbow schlieren images were inverted using computer tomography. Tomography is a multi-angular technique which involves making  $M$  line of sight measurements (deflections) at  $N$  angles. These  $M \times N$  measurements are used to reconstruct the original two-dimensional test object. Several tomographic reconstruction techniques are available. The theory of the convolution backprojection algorithm used in this work is presented.

The rainbow schlieren technique was used to measure temperature in an axisymmetric heated air jet. The Reynolds number of the jet was 570 and the jet I.D. was 7.1mm. The heated axisymmetric jet was chosen to demonstrate the technique by comparing reconstructed temperatures with thermocouple probe measurements. Because of axisymmetry of the jet, only one view was required to reconstruct the temperature field using the rainbow schlieren technique. The temperature reconstructions of the jet at several axial locations above the jet were found to agree with the thermocouple

measurements. This agreement demonstrated that the rainbow schlieren technique could be used for temperature measurements in test fields of various configurations.

Having demonstrated the technique, the round jet was tilted to provide a test field which was asymmetric. The jet exit was inclined by 30 degrees to the vertical axis, which created an asymmetric temperature field above the jet. This necessitated the use of computer tomography to reconstruct the three-dimensional temperature field. The jet Reynolds number was 380 and the jet I.D was 5.4mm. The measurements were determined by recording multi-angular views of the test field using the rainbow schlieren imaging technique. Thermocouple measurements were also made at two axial planes above the jet exit. Measurements by the two different techniques agreed with each other within the experimental errors.

Next, the technique was applied to investigate physical phenomena in an asymmetric 3-D field. The phenomenon chosen was the development of a laminar rectangular heated air jet. The rectangular jet had a cross-sectional area of 8.7mm by 3.9mm. The Reynolds number based on the width (smaller dimension) was 500. The jet exit temperature was 450 K. The temperature profiles along the minor and major planes of the rectangular jet were determined at various locations downstream of the jet. It was shown that the trend observed was consistent with published results on three dimensional jets. It was found that the spreading rate of the thermal shear layer of the jet in the plane of major axis was higher than that in the plane of the minor axis. This study shows that the quantitative schlieren measurement technique could be useful to gain understanding of the fluid/combustion dynamics.



## ACKNOWLEDGMENT

First of all, I would like to thank our Almighty Heavenly Father for taking care of me and my family. Without His blessing this work could not have been possible.

I extend my gratitude, appreciation and sincere thanks to my Co-Advisor Dr. A.K. Agrawal for his continuous guidance and assistance provided during the experimental work and writing of this dissertation. I really appreciate his availability to me at all times during the course of this work. The countless hours we spent together is deeply appreciated. This work could not have been possible at all without his support over the past eight months.

Above all, I would like to thank my major Advisor Dr. S.R. Gollahalli, Lesch Centennial Professor of Mechanical Engineering who made it all possible. I thank him for the opportunities he accorded me over the last four years. I have learned a lot from him both personally and professionally. I appreciate his guidance and support throughout the past four years.

Special thanks are extended to members of my Advisory committee Dr. M.L. Rasmussen, Dr. R. Parthasarathy and Dr. M.U. Nollert. I appreciate their time and effort while serving on my committee.

I also like to thank my colleagues Khalid Al-ammar, Anil Kumar Shenoy and Steven Cherry for the help they gave me during the course of this work. I also extend my appreciation to the staff of AME Machine shop, Mark Winn and others. To you all, I say thank you.

A special note to my wife, Mumbua, for her love, encouragement and sacrifices. Her support and understanding are deeply appreciated. I also say to her “thank you dear for typing this work”.

*This dissertation is dedicated to my late father Peter Butuk,  
and my mother Rael Butuk.  
To my daughters Jepkoech, Jepchumba, and Jepngetich,  
I did it for you so that you may strive to do better than Daddy.*

# TABLE OF CONTENTS

<b>CONTENTS</b>	<b>PAGE NO.</b>
ABSTRACT	iv
ACKNOWLEDGMENTS	vi
TABLE OF CONTENTS	ix
LIST OF FIGURES	xii
NOMENCLATURE	xvii
Chapter 1: INTRODUCTION	1
1:1 Optical Techniques	3
1:2 Line-of-Sight Measurements	9
1:3 Tomographic Reconstruction	11
1:4 Objectives	14
Chapter 2: BACKGROUND AND LITERATURE REVIEW	16
2:1 Beam Deflection Techniques	16
2.2 Inversion of 2-D axisymmetric fields	20
2.3 Tomographic Reconstruction	22
2.4 Buoyant Jets	27
Chapter 3: THEORY	34
3.1 Principle of Schlieren Technique	34
3.2 The Radon Transform and Line Integrals Data	40
3.3 Inversion of Axisymmetric or 2-D Fields	43

3.4	Inversion of Asymmetric or 3-D Fields	44
3.5	The Convolution Backprojection Method	46
3.6	The Phantom Test Objects	59
	Figures 3.1-3.16	64
Chapter 4:	EXPERIMENTAL METHODS	81
4.1	Experimental Apparatus	81
4.2	Experimental Procedures	85
4.3	Sources of Errors and Error Analysis	88
	Table 4.1	93
	Figures 4.1-4.4	94
Chapter 5:	RESULTS AND DISCUSSIONS	100
5.1	The Round Heated Jet	100
5.2	The Inclined Round Heated Jet	104
5.3	The Heated Rectangular Jet	106
	Figures 5.1-5.25	113
Chapter 6:	CONCLUSIONS AND RECOMMENDATIONS	159
	REFERENCES	161
	APPENDICES	
	Appendix A.1	168
	Appendix A.2	169
	Appendix A.3	170
	Appendix A.4	171

Appendix A.5	173
Appendix A.6	176
Appendix B.1-B.4	184

## LIST OF FIGURES

1. Figure 3.1 Basic schlieren setup using lenses
2. Figure 3.2 Filter calibration curve
3. Figure 3.3 Interaction of object field and rays and the object coordinate system and projection data rotated coordinate system
4. Figure 3.4 Beam deflection angle of a ray that has traversed an object field
5. Figure 3.5 Inversion of 2-D axisymmetric refractive index field
6. Figure 3.6 Illustration of the Fourier slice theorem
7. Figure 3.7 Radial frequency samples of the object function
8. Figure 3.8 Direct Fourier reconstruction technique
9. Figure 3.9 Interpolation of the backprojection data
10. Figure 3.10 Backprojection of interpolated values of convolved projection data
11. Figure 3.11 The convolving function for ordinary deflection data and beam deflection data
12. Figure 3.12 Length of rays through an elliptical object
13. Figure 3.13 Projection data used in reconstruction algorithm
14. Figure 3.14a Steps in reconstruction of an elliptical object of uniform density showing the projection data and the convolved data.
15. Figure 3.14b Results of reconstruction of an elliptical object of uniform density.
16. Figure 3.15 Reconstruction of refractive index field using beam deflection algorithm for 20 and 50 views. number of rays is 250
17. Figure 3.16 Reconstruction of refractive index field using beam deflection algorithm for 100 and 300 views and 250 rays

18. Figure 4.1 Overall experimental setup showing the schlieren optics and jet apparatus
19. Figure 4.2a The round jet assembly
20. Figure 4.2b The inclined jet assembly
21. Figure 4.2c Rectangular jet assembly
22. Figure 4.3 Three dimensional traversing system
23. Figure 4.4 Setup showing filter calibration. No disturbance in test section
24. Figure 5.1a Plot of hue across a scanline
25. Figure 5.1b Plot of deflection across a scanline
26. Figure 5.1c Plot of change in refractive index across a scanline
27. Figure 5.1d Plot of reconstructed temperatures across a scanline
28. Figure 5.2a Plot of hue of 10 images
29. Figure 5.2b Plot of mean hue of 10 images with error bars
30. Figure 5.3 Effect of hue averaging and temperature averaging on the results
31. Figure 5.4a Comparison of reconstruction and thermocouple measurement at  $z = 5$  mm. Reconstruction using average hue of ten images across x-axis.
32. Figure 5.4b Comparison of reconstructions and thermocouple measurements at  $z = 10$  mm across x-axis.
33. Figure 5.4c Comparisons of reconstructions and thermocouple measurements at  $z = 15$  mm across x-axis.
33. Figure 5.4d Comparisons of reconstructions and thermocouple error bars for measurements at  $z = 5$  mm across x-axis.



34. Figure 5.5a Comparison of reconstructions from single schlieren image and thermocouple measurements at  $z = 5$  mm across the x-axis.
35. Figure 5.5b Comparison of reconstruction from single Schlieren image and thermocouple measurements at  $z = 10$  mm across x-axis
36. Figure 5.5 c Comparison of reconstruction from single Schlieren image and thermocouple measurements at  $z = 15$  mm across x-axis
37. Figure 5.6a Reconstruction along the axis normal to light rays at  $z = 5$ mm.
38. Figure 5.6b Reconstruction along the axis normal to light rays at  $z = 10$  mm
39. Figure 5.7 Contour plots within a vertical plane, parallel to the light rays at  $y = 3$ mm.
40. Figure 5.8 Contour plots at the horizontal axial plane through  $z = 5$ mm
41. Figure 5.9 Contour plots at the horizontal axial plane through  $z = 10$ mm
42. Figure 5.10 Contour plots at the horizontal axial plane through  $z = 15$  mm
43. Figure 5.11 Comparisons of thermocouple measurements with schlieren reconstructions from the axial location  $z = 5$ mm and line  $x = 12$  mm
44. Figure 5.12 Comparisons of thermocouple measurements with schlieren reconstructions from the axial location  $z = 5$  mm and line  $y = 0$
45. Figure 5.13 Comparison of thermocouple measurements with schlieren reconstructions from the axial location  $z = 10$  and line  $x = 15$
46. Figure 5.14 Comparison of thermocouple measurements with schlieren reconstructions from the axial location  $z = 10$ mm, and line  $y = 0$

47.    Figure5.15a    Comparison of thermocouple measurements with schlieren reconstructions for axial location  $z = 5$  mm, major axis reconstruction.
48.    Figure5.15b    Comparison of thermocouple measurements with schlieren reconstructions for axial location  $z = 5$ mm, minor axis
49.    Figure5.16a    Comparisons of thermocouple measurements with schlieren reconstructions for axial location  $z = 10$  mm, major axis
50.    Figure5.16b    Comparison of thermocouple measurements with schlieren reconstructions for axial location  $z = 10$  mm, minor axis
51.    Figure5.17a    Comparison of thermocouple measurements with schlieren reconstructions for axial location  $z = 15$ mm, major axis
52.    Figure5.17b    Comparison of thermocouple measurements with schlieren reconstructions for axial location  $z = 15$ mm minor axis.
53.    Figure5.18a    Contour plots at axial plane through  $z = 5$  mm
54.    Figure5.18b    Contour plots at axial plane through  $z = 10$ mm
55.    Figure5.18c    Contour plots at axial plane  $z=15$ mm
56.    Figure5.19a    Contours in vertical plane parallel to the major axis, at the center of the jet
57.    Figure5.19b    Contour in vertical plane parallel to the minor axis, at the center of the jet.
58.    Figure5.20a    Plot of jet half-widths for both minor and major axis
59.    Figure5.20b    Plot of non-dimensionalized jet half-width for major axis
60.    Figure5.20c    Plot of non-dimensionalized jet half-width for minor axis
61.    Figure5.21    Comparison of jet half-widths.

- 62.    Figure5.22a    Plot of decay of centerline temperature
- 63.    Figure5.22b    Temperature decay fitted to equation suggested by Sfeir (1976).
- 64.    Figure5.23a    Temperature profiles across several z-locations for major axis.
- 65.    Figure5.23b    Non-dimensionalized temperature profiles across several z-locations for major axis. Non-dimensionalized by similarity parameters.
- 66.    Figure 5.24a    Temperature profiles across several z-locations for minor axis
- 67.    Figure5.24b    Non-dimensionalized temperature profiles across several z-locations for minor axis. Non-dimensionalized by similarity parameters.
- 68.    Figure5.25    Comparison of growth rate of round jet, plane jet and present rectangular jet.

# NOMENCLATURE

## English Symbols

a	Sample spacing
A	Dimension of test object
b	Convolved projection data
c	Velocity of light
C'	Filter transmissivity function constant
e	Ellipse view angle dependent variable
E	Fourier transform of deflection angles projection data
f	Focal length and object field function
h	Value of hue
I	Light intensity
K	Gladstone - Dale constant
K'	Filter transmissivity function constant
M	Number of rays per view angle (projection)
$\bar{n}$	Normalized refractive index difference
n	Refractive index
N	Number of view angles
$\tilde{N}$	Fourier transform of normalized refractive index difference
p	Projection (line integral value)
q	Convolution function
r	Radius

$s$	Path of a light ray
$S$	Fourier transform of projection data
$t$	Direction normal to the path of the ray
$T$	Temperature
$u$	Frequency component in Fourier space
$v$	Frequency component in Fourier space
$x$	Spatial Coordinate
$y$	Spatial coordinate
$z$	Spatial coordinate

#### Greek Symbols

$\Delta$	Difference on small change
$\delta$	Delta function
$\phi$	Phase angle
$\lambda$	Wavelength
$\mu$	Attenuation coefficient
$\epsilon$	Deflection angle
$\theta$	Projection angle or view angle
$\rho$	Density
$\omega$	Frequency in Fourier space

#### Subscripts

$a$	ambient or surroundings
$c$	center or decollimating lens

- e     exit
- i     ray number
- j     view angle number
- o     Reference or background or virtual origin

## **Chapter 1**

### **INTRODUCTION**

Flows encountered in combustion and fluid dynamics involve interactions of complex physical and chemical processes. To understand these flows, researchers have used experimental methods in the past, and more recently, computational fluid dynamics or CFD. These computational techniques still require experimental data to validate the models incorporated. Because of the rapid development of CFD, an increased need has arisen for new experimental techniques to provide the necessary data for validation of the physical models. Computational results are necessarily of high spatial and temporal resolutions and as such require similar experimental data for validation. So far, optical techniques have been proven to be quite attractive in this regard. In this work we present an optical technique, Rainbow Schlieren Imaging, for measurements of temperature (and other physical properties) in fluid flows.

The measurement of temperature is important in many processes and applications. In combustion systems, for example, the temperature provides information about combustion efficiency, the rates of formation of unwanted particulates and pollutant species, and allows one to predict the radiant heat transfer. For this reason, several different techniques have been developed to measure not only temperature, but also other properties such as density and species concentrations.

A considerable effort has gone into the development of adequate instrumentation for measuring temperature, which includes specially designed intrusive probes as well as

various optical techniques. Usually, the simplest and least costly diagnostic system utilizes probes such as thermocouples, and they are used if they meet the needed requirements. However, the temporal response of intrusive probes is poor, their size limits the spatial resolution, they introduce disturbance in the medium, and they survive with difficulty in hostile environments, for example, of combustion systems. In addition, the probe may induce chemical reactions in the flow field and hence change the properties of the medium.

Other techniques for temperature measurement include radiation thermometry and sonic thermometry. Radiation techniques make use of absorption measurements. Ultraviolet rays and X-rays are used as probing sources. These techniques offer good precision but limited spatial resolution. They are also restricted to relatively high temperature regions. Using X-rays as probing sources offers moderate spatial resolution; however, the question of safety in their use becomes important. Sonic temperature measurements are not widely used as they also suffer from poor spatial resolution, and require a prior knowledge of species present in the flow [Fristrom (1995)].

Optical measurement techniques have many advantages over other measuring methods. Besides being non-invasive they are also highly responsive to the transient phenomena and have a high spatial resolution. Depending on the measurement problem under study, optical techniques may be used to determine the physical parameters of the process being investigated. These parameters may include the temperature distribution in the fluid, the concentrations of certain substances in the flow, or the local velocity of



droplets in a combustion chamber. Many optical techniques have been developed, with their own special characteristics, suitable for measurements of these parameters.

Optical techniques to measure temperature can be classified into two groups: one providing local measurements of a parameter and the other yielding integral information of a parameter that could be related to the temperature. The methods for local measurements are based on light scattering techniques, and the methods for integral measurements are based on the line-of-sight measurements techniques. A brief discussion of these techniques is given in the following section.

### **1.1 Optical Techniques**

Light scattering techniques: Techniques that provide local measurement of a parameter relating to temperature are based on scattering of light. These techniques resulted from the development of lasers and solid state array detection devices. They include Rayleigh scattering , Raman scattering, Laser Induced Fluorescence (LIF) imaging, and methods that depend on higher order scattering such as Coherent Anti-Stokes Raman spectroscopy (CARS) [Fristrom(1995)]. All of these methods can be used to determine temperature. However, they are all complex in implementation and often require expensive laser sources.

Rayleigh scattering is the elastic (or unshifted) scattering of light by molecules in the field of study. This scattering is not specific to the molecule causing the scattering, and it does not require turning of the laser source. However, it suffers from interference from scattering from particles (Mie scattering) and from spuriously scattered laser light.

Because of this, Rayleigh scattering is restricted to environments that are pure and free of particles [Laurendeau (1991)].

LIF imaging is a highly sensitive technique for detecting population densities of atoms and molecules in specific excited states. In this method, a laser source is tuned to excite molecules of a specific species of interest. In their excited states, these molecules can lose energy to return to their original states by two ways; collisional quenching (energy lost by collisions) and radiative de-excitation (or fluorescence). It is this fluorescence, that is collected at a right angle to the incident probing laser beam and filtered spectrally at a photo-detector that is used to measure the parameter of interest. Fluorescence, therefore, is in competition with collisional quenching and internal conversions to other states. In other words, if the excited molecules lose most of their acquired energy through collisions, then the fluorescence signal will be weak. The relative rates of these two competing processes, therefore, controls the usefulness of LIF [Kohse-Honinghaus (1990)]. To obtain quantitative results, the molecular spectrum of the field must be known and it must have absorptions compatible with tunable lasers. Because of this, the applicability of LIF for quantitative measurements is limited. Depending on the arrangement of the experimental setup, this method can be used for point or planar measurements of the flow field. When used for planar measurements the technique is termed planar LIF or PLIF.

Spontaneous Raman scattering is a non-resonant method whereby the scattered light undergoes a change in frequency and random alteration in phase. Raman scattering differs in this respect from Rayleigh scattering in which the scattered light has the same

frequency as the incident light and bears a definite phase relation to it. The scattered frequencies are analyzed by spectroscopic means and a particular Raman spectrum is characteristic of the scattering medium. It does not require any turning of the laser to a particular wavelength, nor is it affected by collisional quenching. In Raman scattering, the frequency of scattered light is shifted either up (anti-Stokes) or down (Stokes); because of this, it is unaffected by interference from particles (Mie scattering) or from the incident beam. However, it requires frequency isolation using scanning monochromators (special filters placed in front of detectors) [Fristrom (1995)]. A major disadvantage of this technique is that the signal is very weak because the vibrational Raman cross-section (a measure of the intensity of the scattered light) is about 1000 times smaller than the Rayleigh cross-section [Lapp and Penny (1977)]. Higher-order scattering techniques such as CARS require more than one laser source, and are therefore very expensive and complex in operation [Attal-Tretout et al. (1990)]. In general, all of the scattering techniques rely on reflected light, and as such many spurious rays (light from different points other than the measurement volume) from different points may reach the detectors and can cause erroneous measurements to be recorded. This discussion leads to the other class of optical techniques in which an integral quantity of a parameter is determined in a line-of-sight measurement.

Line-of-sight techniques: These techniques are based on the absorption or attenuation of light rays, change in path length of the light rays, and deflection of light rays by the media.

Light absorption measurements can be used to determine absorption coefficients along the path of a light ray. These absorption coefficients can then be related to the temperature and species concentration in the flow field [Faris (1986)]. However, in most cases temperature is a function of species concentrations. Thus, it becomes necessary to use coherent light sources of two different wavelengths to determine both the temperature and species concentrations.

In interferometry, use is made of the pathlength difference between a coherent beam passed through the object field and a reference beam not passed through the object. When these two beams are combined on a screen, an interference pattern is produced containing regions of differing optical path length. The spacing between interference fringes can be used to deduce the density or temperature of the flow field. A drawback of this method is that, when high temperature gradients are present, fringe counting becomes a tedious and often an impossible task. When combined with holography, this technique is known as holographic interferometry, whereby a holograph is used to record multiple interferograms. Holography is used to record light wave patterns. Ordinary image recording techniques, such as photographic film, record the intensity of light falling on them. Holography, on the other hand, is used to record and reconstruct light waves. This means that in addition to intensity, the amplitude (brightness) and phase position are also recorded. This is made possible because a reference beam is used in conjunction with the object beam to produce an interference pattern at the recorder. For making temperature measurements the main disadvantage of holography is that it requires specialized optical components to improve the depth of field. It also requires expensive

Q-switched lasers to provide very short pulse length to avoid problems associated with vibrations.

The measurement of deflection of light rays by the media in beam-deflection techniques, also known as deflectometry, can provide an indication of the density and temperature of the medium. A practical example is the light deflection through air rising above heated objects, which is less dense than the surrounding air. This difference in density alters the refractive property of the air and, therefore, deflects light rays from their normal path. This effect has been used in the beam deflection techniques to qualitatively study normally invisible phenomena such as convection currents in air as well as the flow of air around speeding objects, including bullets and wings of modern jet airplanes. Two basic techniques belong to this class; schlieren and shadowgraph. The shadowgraph technique provides an indication of the second derivative of the density variation (or refractive index), and schlieren which is the subject of this work indicates the density or refractive index gradient of the field [Kanury (1975)]. Other techniques that can be classified as beam deflection techniques include speckle photography [Farrell and Hofeldt (1984)], and Moiré deflectometry [Stricker (1984)]. Unlike the interferometric technique, beam deflection techniques do not require a highly stable, vibration free environment. Sharp gradients of refractive index do not present difficulties. Beam deflection techniques are also not affected by the size of the object unlike the interferometric techniques.

In the conventional schlieren technique, light from a small source is collimated by a lens and focused onto a knife-edge by a second lens. The test object is placed

between these two lenses (see Figure 3.1). The knife edge is adjusted in such a way that it intercepts a part of the rays. The unobstructed rays that proceed beyond the knife edge are focused by a camera lens onto a recording plane. When the object in the test section is uniformly dense, all parts of the screen are lighted equally; the intensity of the light that reaches the screen is determined by the amount of light intercepted by the knife edge. When there are refractive index gradients in the test object, however, some of the light rays are displaced. The rays that could normally fall on the screen will be intercepted by the knife edge. Thus, the screen will appear darker or brighter (depending on the direction of the deflection). The magnitude of deflection and direction of light rays can, therefore, be inferred from the measurements of the intensity with and without the refractive index gradients in the test object. These deflections are then related to the refractive index from which the temperature can be calculated. Grids and various other devices have been used to measure these deflections. In this work, the rainbow schlieren technique, which uses variations in hue of a rainbow filter is used to quantify light ray deflections. The rainbow filter is used in place of the knife edge. Depending on the displacement of light rays, the rainbow filter will transmit different hues to the recording plane. In this way discrimination between colors (hue) is used as an indication of the light ray of deflection.

Shadowgraphy is the simplest method for implementing flow visualization. In this method, a light source illuminates the object and is intercepted on a screen placed ahead of the object. A non-uniform distribution of brightness will appear on the screen due to the deflection of light by the object. In contrast to the schlieren method, the image

on the screen and the object are not conjugate pairs (i.e., a point on the screen does not correspond to the related point in the object). The deflection of single lines or grids, images formed by parallel beams has been applied by Weinberg (1963) to determine density and temperature fields. This method is, however, less sensitive than the schlieren method.

In order to quantify the shadowgraph and schlieren methods and hence record signals equivalent to fringes in an interferogram, grids or “Ronchi” gratings have been used to measure deflections. When used in this way the grids cause a “Moiré effect” which has led to the development of beam deflection methods such as Moiré deflectometry and speckle photography. The optical system for Moiré deflectometry consists of a collimated laser beam and two parallel gratings (Ronchi rulings) mutually rotated at an angle. The system produces a Moiré pattern which is distorted when refractive index gradients are present in the test object. In speckle photography, the displacement of a speckle pattern generated by the interaction of a coherent light beam with a diffusing surface is recorded photographically. These speckles are, however, difficult to identify and evaluate. Deflections can also be measured using a laser beam technique in which a laser beam is traversed through the media and the beam deflection at each point is measured directly by a position sensitive detector.

## **1.2 Line-of-sight Measurements**

The methods of beam deflection, path length difference, or light absorption discussed above provide information about the physical observations integrated along the

path length of the light beam. The parameter measured depends on the technique used. For absorption measurements the light intensity is measured before and after the ray has traversed the test object. In beam deflection measurements, the deflection angle of the light ray as it exits the test object is measured, and in interferometry the difference in path length is measured. In order to infer the temperature field of the test object from these measurements, it is necessary to invert an integral equation. Specifically the integral equation to be solved is:

$$p_i = \int_{s_i} f(x, y, z) ds \quad (1.1)$$

where the value of  $f(x,y,z)$  is the medium characteristic that is to be determined, and  $p_i$  is the line of sight integral measurement recorded. The field distribution function  $f(x,y,z)$  depends upon the technique used for the measurements. In absorption measurements, it is the attenuation constant, in interferometric measurements it is the refractive index, and in deflectometry, it is the gradient of refractive index. The quantity  $p_i$  is commonly known as the projection for a particular light ray  $i$ . The integral is evaluated along the path  $s_i$  of the light ray as it traverses the test object.

Inversion means solving for  $f(x,y,z)$ , using the measured projection data  $p_i$ . Several techniques have been used to invert this equation. If the field is 2-D or axisymmetric, the projection data at a single view angle are sufficient to reconstruct the test object. The classic Abel inversion and the “onion peeling” techniques [Hughey and Santavicca (1982)] have been used to reconstruct axially symmetric objects. However, if the object field is 3-D (or asymmetric), projection data at a single view angle are insufficient to reconstruct the test object. This means that for an asymmetric object, the



interior flow information must be obtained from the line-of-sight measurements (or projections), at multiple view angles. Thus, techniques are required to reconstruct 3-D fields from their projections.

Tomography meets this need, to allow quantitative flow measurements from a set of line-of-sight projection data usually in the form of images. From the above classical techniques of interferometry, schlieren and light absorption, 3-D flow fields can be reconstructed using computer tomography. Several tomographic techniques have been developed for this purpose.

### **1.3 Tomographic Reconstruction**

Tomographic methods have been developed over the past 50 years in the fields of medicine, electron microscopy and radio astronomy [Faris (1986)]. In medicine tomography is widely used to obtain the density distribution within the human body from multiple-view projections. This process is known as Computerized Tomography (CT) in radiology, Single Photon Emission Computerized Tomography (SPECT) in nuclear medicine and Magnetic Resonance Imaging (MRI) in diagnosis. The aim of computer tomography is the inversion of the equation 1.1, where the projections  $p_i$  along rays in a direction  $s$  are recorded at multiple view angles. Various algorithms have been developed since Radon published his famous projection equation in 1917, and which analytically related projections to a cross-section image [Decker(1994)]. The actual form of equation 1.1 to be inverted using tomography depends on the measurement technique.

In absorption measurements, the intensity of the light ray before and after the test object is recorded. The absorption of light as a ray traverses the test object field is governed by Bouguer-Lambert-Beer Law [Santoro and Semerjian (1981)].

$$I_{out} = I_{in} \cdot e^{-\mu_1 \Delta s} \cdot e^{-\mu_2 \Delta s} \cdot e^{-\mu_3 \Delta s}$$

where  $I_{in}$  is the intensity of the beam as it enters the object field and  $I_{out}$  is the intensity as it leaves the test object field. If the object field traversed by the ray is divided into equal rectangular grids or pixels, then  $\mu_i$  are the linear attenuation constants of the successive grids (traversed by a particular ray) and  $\Delta s$  is the size of the grid. This equation is cast into the form of the integral equation 1.1 by taking the logarithm of the ratio of output signal to input signal, resulting in:

$$\begin{aligned} \log \frac{I_{out}}{I_{in}} &= -(\mu_1 + \mu_2 + \mu_3 + \dots) \Delta s \\ &= - \int \mu_i ds \end{aligned} \tag{1.2}$$

This is a simple sum of the linear attenuation coefficients in the path of each ray. The  $\mu_i$  then represent the function  $f(x,y,z)$  within the object field. The logarithms of the ratio of output to input light intensity represent the projections  $p_i$ . The attenuation coefficients once determined by inversion can then be related to the temperature of the test object.

In interferometry, the equation representing the difference in arrival times ( $\Delta t$ ) of the reference ray and the ray that traversed the test object at the recording plane is given by:

$$\Delta t = \frac{1}{c} \int_{s_1} (n(x, y, z) - n_o) ds$$

where  $c$  is the speed of light in a vacuum,  $n_o$  is the refractive index of the undisturbed field outside the test object and  $n(x,y,z)$  is the object refractive index. The time difference,  $\Delta t$ , can be converted into optical path length,  $\Delta\phi$ , via the equation:

$$\frac{\lambda\Delta\phi}{2\pi} = \int_{s_i} (n - n_o) ds \quad (1.3)$$

where  $\lambda$  is the wavelength of the light used [Merzkirch (1987)]. From interferometric data, therefore, the refractive index can be obtained by direct inversion of the integral equation 1.1 as  $f(x,y,z)$  is equal to  $[n(x,y,z)-n_o]$  and  $p_i$  is proportional to  $\Delta\phi$  measured from the interference pattern. However, as mentioned above, the evaluation of  $\Delta\phi$  by fringe counting could be tedious in some cases.

In beam deflection measurements by schlieren and similar techniques, the deflection angle of a light ray as it exits the test object is related to the refractive index  $n$ , of the test object via:

$$\epsilon = \int_{s_i} \frac{1}{n} \frac{\partial n}{\partial t} ds \quad (1.4)$$

where  $t$  is in a direction normal to the light ray path  $s_i$ . In this form,  $f(x,y,z)$  represents the gradient of refractive index of the test object and  $\epsilon$  represents the projection. We shall show in chapter 3 how this equation can be converted to the form of equation 1.1, where  $f(x,y,z)$  represents the relative refractive index directly.

When the appropriate integral form of equation 1.1 is solved for the refractive index distribution, the temperature field can be obtained using the Gladstone-Dale relationship between the refractive index and density or temperature [Goldstein (1996)].

## 1.4 Objectives

The objectives of this work are to demonstrate the beam deflection technique of rainbow schlieren imaging by making temperature measurements in axisymmetric and asymmetric objects. Computer tomography is used to invert equation 1.4 expressed in the form of equation 1.1 to reconstruct the temperature field from the beam deflection measurements.

The rainbow schlieren technique, measures the deflection angles as a ray exits an object test section. This technique is a slight modification of the conventional schlieren method. As mentioned above, discrimination between grey scales is carried out in the conventional schlieren method. The intensity in the schlieren image is proportional to the refractive index gradient and the deflections are determined from intensity measurements. Quantifying deflections from intensity measurements is, however, difficult. Quantification is possible if the knife edge is replaced by a multicolored filter (the rainbow filter). Then, the light rays refracted through different angles appear in different colors in the final schlieren image. When a color filter is used, a colored photograph is recorded. On this photograph discrimination between colors (or hue) is used as a measure of deflections. Discrimination between colors is more accurate and insensitive to brightness when compared to discriminations between grey scales of the conventional schlieren photograph. It will be shown how the light ray deflections by a test field can be quantified using the rainbow filter.

The overall optical setup in rainbow schlieren deflectometry is similar to that of the conventional schlieren with the knife edge replaced by a color filter. We shall demonstrate the rainbow schlieren technique by first making measurements in an axisymmetric heated laminar air jet. Next, we shall extend for measurements of temperature in an asymmetric test field above a heated inclined air jet. Finally, the technique developed will be used to study the development of a rectangular laminar buoyant (heated) air jet. In all cases, the temperatures obtained by the schlieren method will be compared with the thermocouple measurements at several planes.

It will be shown that the temperatures obtained by the rainbow schlieren deflectometry compare well with the thermocouple measurements to within the experimental errors. The rainbow schlieren technique also provided insight into the physical development of a rectangular heated air jet.

## Chapter 2

### BACKGROUND AND LITERATURE REVIEW

In this chapter we shall discuss beam deflection measurement techniques with particular emphasis on rainbow schlieren deflectometry. We shall review pertinent literature on inversion techniques for axisymmetric fields as well as tomographic reconstruction techniques for 3-D fields. In fluid flows, the projection data for tomographic inversion could be obtained by three basic methods; light absorption techniques, interferometric techniques, and beam deflection techniques. The literature will be reviewed with reference to these basic techniques. Finally, we shall review the background and literature on rectangular heated jets.

#### 2.1 Beam Deflection Techniques

In beam deflection measurement techniques, a beam passes through a test object and is deflected due to the refractive index gradients. The amount of deflection or the deflection angle of the beam as it exits the test section is related to the refractive index  $n(x,y)$  of the field. Consider the refractive index field shown in Figure 3.4. In this figure, let  $n_0$  = refractive index outside the object field. Then, for small deflections, the deflection angle  $\epsilon$ , of a beam at an angle  $\theta$  with the x-axis is given by

$$\epsilon(\theta, t) = \frac{1}{n_0} \int \frac{\partial n}{\partial t} ds \quad (2.1)$$

It is the measurement of this angle that is important in beam deflection techniques. The different beam deflection techniques measure this angle using different methods. Beam-deflection measurements may be performed using imaging techniques such as schlieren, Moiré deflectometry, and speckle photography. Use can also be made of a scanned laser beam. Once this angle has been determined, an inversion procedure must be performed to determine the refractive index.

#### The schlieren technique

The schlieren technique can be described as a deflectometric method or a beam-deflection optical method as opposed to the path length difference method of interferometry and holography. The schlieren method, whose principle was developed more than a century ago, is one of the simplest and most commonly used technique for flow visualization. Details of optical arrangements and applications are given by Vasil'ev (1971) and Goldstein and Kuehn (1996). Detailed theoretical analyses of the method are given by Schardin (1942) and Weinberg (1963). A beam of parallel light from a slit or point source is passed through a region of varying refractive index gradient and brought to a focus on a stop (see Figure 3.1). This stop is usually a knife edge. Regions containing varying refractive index will deflect the light waves around the knife edge. The unobstructed rays that proceed beyond the knife edge are focused by a camera objective onto a recording plane. When the object in the test section is uniformly dense, all parts of the screen are lighted equally; the intensity of the light that reaches the screen is determined by the amount of light intercepted by the knife edge. When a refractive index gradient is present in the test object, however, some of the light rays are deflected. The

rays that could normally fall on the screen will be intercepted by the knife edge. Thus, the screen will appear darker or brighter (depending on the direction of deflection) than normal in the region where these rays formerly impinged. The magnitude of deflections and directions can therefore be inferred from the measurements of intensity with and without the refractive index gradients in the test object. These deflections are related to the refractive index from which the temperature can be calculated. In actual practice, the determination of deflections via measurement of intensity (which is difficult to quantify accurately) in the recorded grey scales in the image has some limitations as discussed by, Dixon-Lewis (1954).

In its generic form, the difficulties associated with the practical aspects of the schlieren method have caused it to remain a qualitative tool, for flow visualization. Recently, Greenberg et al. (1995) demonstrated its potential for quantitative measurements when color is introduced as a dimension in the rainbow schlieren deflectometry. Color is introduced when the grey scale is changed to yield the color spectrum instead of shades of grey. In this technique, the knife edge is replaced by a rainbow filter containing color gradations. Discriminations between deflections is indicated by variations in color and represented by hue instead of variations in grey tones of the conventional schlieren photograph.

Howes (1984) first demonstrated the quantitative rainbow schlieren technique by replacing a typical knife edge with a filter containing a rainbow color spectrum (continuous spectrum, not discrete spectrum). Before this special filter was introduced, several filters had been used for color schlieren observations as summarized by Settles



(1985). The problem with these other methods of color schlieren has been mainly limited sensitivity due to a finite number of color bands and the deleterious effects of diffraction at color boundaries which degrade the spatial resolution in the schlieren image. The filter introduced by Howes (1984) allowed measurements of a flow field from observations of color rather than irradiance in a typical black and white schlieren method. Howe's filter had a transparent center and opaque surroundings.

The rainbow filters were manufactured by Howes (1984) by projecting white light through a slit, and then a diffraction grating, and onto a spinning color film. The resulting film was then reduced in size by projecting white light through them onto a screen at varying distances. This method of manufacturing the filters was cumbersome. Recently, Greenberg et al.(1995) demonstrated a far simpler method of manufacturing the color filter, and, when combined with linear solid-state imaging arrays, it represented a simple system to quantify schlieren. The linear imaging arrays eliminated the problem associated with non-linear film-based methods.

#### Other beam deflection methods

Other beam deflection methods include scanned laser beam, Moiré deflectometry and speckle photography. In the laser beam technique, a laser beam is traversed through the media and the beam deflection at each point is measured directly by a position sensitive detector. This technique was used by Fairs and Byer (1986) for temperature measurements in a methane flame and by Davis (1989) to measure refractive index fluctuations in a hydrogen flame. In speckle photography, a photograph consisting of speckles is produced in a typical schlieren apparatus by replacing the knife edge with a

ground glass (in a variation of the method the ground glass is placed upstream of the knife edge). A micro-sized reference pattern is then generated on the recording screen. The recorded speckle pattern is determined by the scattering characteristics of the ground glass. A double-exposed photograph is required. The first exposure is taken in the undisturbed flow field. The pattern that is generated on the photograph is used as a reference. The second exposure is taken with the flow containing refractive index gradients. The pattern that is generated with the second exposure is distorted with respect to the reference pattern. The displacement of individual speckles is a measure of local deflection angles  $\epsilon(\theta, t)$ . This technique has been used for temperature measurement in gases by Farrell and Hofeklt (1984) and in water by Lira (1995). In Moiré deflectometry parallel grids or Ronchi gratings are used to intercept the light beams and an essentially regular pattern is produced by the undisturbed flow field. The pattern is distorted in the presence of refractive index gradient in the flow field. By comparing the undisturbed and disturbed patterns, it is possible to measure and map the deflection of light rays by the test field. This technique was used by Keren et al. (1981) for temperature measurements in an axisymmetric flame and by Stricker (1984) to map 3-D temperature field above two heated cylinders.

## **2.2 Inversion of 2-D and Axisymmetric Fields**

As indicated above the data from schlieren line of sight measurements need to be inverted to reconstruct the refractive index field. For axisymmetric flow fields, the two methods often used are the "onion peeling" and Abel transformation mentioned in chapter

one. Using computer simulated absorption measurements, Hughey and Santavicca (1982) compared onion peeling and Abel transformation for reconstructing axisymmetric non-reacting and reacting flow fields. They showed that the two techniques could yield different results from the same set of data. They recommended a method of frequency analysis of noisy data which when used to filter the data before the reconstruction yields good results.

In the "onion peeling" and Abel transformation methods, they found that the errors are related to the accuracy of the raw and processed input data. When compared with the convolution backprojection method, (to be discussed below) they found that in the convolution method the errors are related to aliasing or under-sampling, to the choice of convolution filter and to what they termed Gibb's phenomena, which is an oscillatory overshoot that occurs at a discontinuity in the reconstructed function.

Dasch (1992) has also compared Abel, onion peeling, and convolution back projection methods. Using an analytical analysis of the method, he reported that the most common mistake in axisymmetric inversion is taking projection data too closely together or over-sampling. He reasons that if the spacing of the projections is decreased, the real difference between adjacent projections becomes smaller to the point where the difference becomes comparable to the noise in the measurements. When this happens, the inversion is inaccurate. In general, he reported that the three methods are similar when the projection data are taken at equal spacing. Overall, however, for axisymmetric data, he recommended the Abel inversion method using a three-point technique because of its speed of implementation.

### 2.3 Tomographic Reconstruction

Tomographic methods have been developed over the past 50 years in the fields of medicine, electron microscopy, and radio astronomy [Faris (1986)]. In medicine it is widely used to obtain the density distribution within the human body from multiple-view projections. Tomography has also been developed and used in several other fields including electrography, geology, ocean acoustic tomography, industrial imaging [Williams (1995)], and non-destructive testing of materials [Hefferman and Robb (1985)]. The computer tomography for fluid flow measurements has been used in the past 30 years, beginning in the late sixties and early seventies. An overview of the use of tomography for fluids flow diagnostics is given by Decker (1994).

Tomographic reconstruction techniques can be classified into iterative methods and Fourier transform based methods [Censor (1983)]. Fourier based methods reconstruct the image from their projections by using each projection only once. Examples in this category include convolution backprojection and direct Fourier transform methods. Iterative methods on the other hand pass through the projection sets several times and find the best reconstruction under a set of constraints. Examples of such techniques include algebraic reconstruction techniques (ART), series expansion methods, and maximum-entropy methods. By far the most popular technique has been the convolution backprojection technique sometimes called the “filtered backprojection reconstruction technique” which is also used in this work and described in detail in chapter 3.

Verhoeven (1993) discusses the various algorithms for tomographic reconstruction. He discusses both the transform based algorithms and the series-expansion algorithms. The series expansion techniques are algebraic techniques based on the Algebraic Reconstruction Technique (ART) first proposed by Gordon et al. (1970). He compares five ART-based techniques using computer simulated data, with and without noise. For limited-view data, he discusses a method of filling in the missing data to be able to use the Fourier transform reconstruction methods.

In fluid flows, tomography has been used with line-of-sight measurements of absorption, holographic interferometry and beam deflection techniques. Semerjan et al. (1981) and Santoro et al. (1981) reported the use of absorption tomography to diagnose concentration fields in a turbulent methane air jet and a laminar methane diffusion flame. They studied a turbulent methane-air jet expanding into ambient air under steady flow conditions. The jet was located away from the center line of rotation to introduce asymmetry upon rotation of the jet for acquisition of multiple views. They used absorption measurements and the convolution backprojection algorithm to obtain excellent agreements of the concentration profiles in the turbulent jet with previous workers. For the laminar flame, their concentration measurements indicated a strong dependence of methane absorption coefficient on temperature, and, as such, they concluded that for accurate reconstruction simultaneous measurements of temperature and concentrations were required. Emmerman et al. (1980) describe the details of reconstructing flow fields from absorption tomography and multiangular scanning.

Ray and Semerjan (1984) describe the measurement of temperature and concentration using multiple view absorption spectroscopy. They present results for both computer simulated data and experimental results using two optical configurations. For their experimental measurements, they used a laminar axisymmetric premixed flame of methane seeded with sodium atoms and measured the absorption of light at 589nm wavelength by the seeded sodium. In this experiment a single laser beam was translated through the flame to obtain the required number of rays. In a second configuration, they used a sheet of laser light and a linear array detector to obtain whole field real-time measurements. The measurements were performed with a repetition rate of 2 kHz and a temporal resolution of 10ns. In all of their reconstructions, they used the convolution backprojection algorithm. They report that reconstruction from noisy data could be improved by first filtering the data with an appropriate filter. The filtering technique was a spatial filtering using a *priori* knowledge about the flow field.

Hall and Bouczyk (1990) have recently performed absorption/emission tomography on an axisymmetric ethylene-air diffusion and iso-octane air diffusion flame. Because the flames were axisymmetric, all projections at different angles of incidence were the same and only one angle of incidence was determined experimentally. In this method, the deconvolution of the projection data yields the product of absorption coefficient and the Planck function. Using the derived absorption coefficients, one calculates the Planck function from which the local temperature was determined.

Sweeney (1973) discussed interferometric reconstruction of 3-D refractive index fields using Fourier transforms and series expansion techniques. He gives a direct

inversion formula, which is the basis of the popular convolution backprojection algorithm used in the present study. This algorithm was first proposed by Ramachandran and Lakshminarayanan (1971). Vest (1979) describes details of the reconstruction procedure using interferometric data.

A widely quoted paper showing a real practical application of interferometry is that of Snyder and Hesselink (1984). They reconstructed the density field around a revolving helicopter rotor blade. Because of the rotating geometry, conventional probes were not suited for this application. Using optical path length data, they recorded several interferograms over  $180^\circ$  viewing angle. They used the convolution backprojection algorithm with a Shepp-Logan filter [Shepp and Logan(1974)]. They found this algorithm to be the fastest among the algorithms described by Herman (1980). Snyder and Hesselink (1988) have studied mixing in fluids and the review paper of Hesselink (1988) describes several applications of interferometry with tomography.

Dufong et al.(1995) have carried out studies on fast tomographic reconstruction of holographic-interferometry data. The reconstruction algorithm of interferometric data is the same as that for absorption tomography. They demonstrated reconstruction using the Simultaneous Algebraic Reconstruction Technique (SART). They also mention reconstruction using the convolution backprojection algorithm. They reconstructed temperatures of heated air above a rectangular jet and found that the reconstructed temperature was consistent with the temperature measured by a thermocouple at a single point. In the present work, temperature comparisons will be made with reconstructions not at a single point only but over complete crosssections.

Faris and Byer (1988) investigated a 3-D supersonic jet using the beam-deflection method. Measurements of density were obtained in the supersonic expansion. They developed the theory of tomographic reconstruction for beam-deflection measurements. They reported good agreement between reconstructions and direct measurements. Faris (1986) also investigated a methane-air diffusion flame using beam deflection tomography and found that the reconstructed temperature field compared well with the thermocouple temperature measurements, again at a single point. Faris (1986) also demonstrated absorption tomography in a supersonic jet of chlorine and found that measurements based on beam-deflections (the subject of this work) were more sensitive than those based on the absorption measurements.

From the above literature survey, it is apparent that very little work has been done on beam deflection tomography, which is the subject of the present work, as compared to the absorption tomography or holographic interferometry for asymmetric flow fields.

The aim of this work is to apply rainbow schlieren deflectometry, a beam deflection measurement technique, to reconstruct temperatures above heated flow fields. In addition to demonstrating the technique, we also show how the technique can be used to investigate a physical phenomenon. In particular we studied the development of a laminar rectangular heated air jet. The rectangular jet was chosen because of its simple geometry and asymmetry, necessitating the use of the 3-D tomography for reconstruction. To interpret the results properly, we present a background and review of the literature on buoyant (heated) jets.



## 2.4 Buoyant Jets

### Background

The two extreme cases of jet flows, the plume and jet have received considerable attention in the literature. However, little work has been directed towards the buoyant jets. The main reason for this is the complexity of the buoyant jet because of the presence of both natural and forced convection mechanisms. Most of the buoyant jets encountered in nature are turbulent. As a result, the limited studies found on buoyant jets have considered turbulent flows. There have been few studies of laminar buoyant jets despite their importance in practical applications. Laminar flows arise at low Reynolds numbers in high viscosity flows such as sensible energy storage in solar energy systems, in lubrication systems and in wakes generated by heated bodies. In most turbulent flows, the flow near the jet exit location is often laminar and undergoes transition to turbulence as it develops downstream [Hussain (1989)]. It is, therefore, important to develop a basic understanding of laminar buoyant jets because they have practical application in some real flows.

Besides the above categories of jets classified on the basis of whether they are turbulent or laminar and whether they are buoyant or nonbuoyant, one other classification is widely used. This classification is based on geometry at the exit location. The jet may be discharged from a circular exit. The resulting flow is axisymmetric if the flow is discharged vertically. The other possibility, is when the jet is discharged from a long slender slit, giving rise to a two-dimensional flow. The slit is generally considered as a line source and the jet is termed a plane or two dimensional jet. Buoyant jets may also be

classified as vertical, inclined, or horizontal. When the flow is discharged from a non-circular or non planar geometry, the jet is termed a 3-D jet. We study in this work the development of a laminar buoyant jet discharging from a rectangular exit of small aspect ratio.

### Literature review

Turbulent round and plane jets have been the topic of many studies [Pai (1954), Crow and Champagne(1971), and Evertt and Robins (1978)]. Gouldin et al. (1986) have presented a thorough review of nonreacting shear flows including the plane and round jets. Brand and Lahey (1967) and Gebhart (1986) have presented analytical solutions for these (axisymmetric and plane) buoyant and nonbuoyant jets. A few studies have dealt with non buoyant rectangular jets of large aspect ratio [Zijnen (1958) and Krothapalli et al. (1981)] and elliptic jets of small aspect ratios [Chih-ming (1987) and Hussain and Hussain (1989)]. Buoyant jets of rectangular crosssections with large aspect ratios have been studied by Sfeir (1976) and Zijnen (1958). Antonia et al. (1984) have discussed the comparison of temperature and velocity turbulent spectra in a slightly heated plane jet. Numerical computations of jets issuing from non circular geometries have been reported by McGuirk and Rodi (1977), Miller et al. (1995), and Grinstein and Kailasanath (1995).

Pai (1954) has discussed the jet problem in details. He divided certain jet flows into two regions, the potential core region and the mixing region. The potential core is the region closer to the nozzle exit. He noted that the viscous effects are negligible in the potential core region, provided the jet is designed to have a flat exit velocity profile. The first part of the mixing region is on the boundary of the jet near the exit of the nozzle.

This mixing region widens as the flow develops downstream. Far downstream, the entire jet evolves into a viscous mixing region. In this mixing region, there are large variations of velocity and possibly density. Here it is necessary to include the viscous terms in the analysis, and also the heat transfer effect for buoyant jets. The jet entrains a part of the fluid at rest owing to the viscous effects, thereby, sweeping an ever increasing mass along.

Schlichting (1968) was among the first to present an analytical solution of the laminar non-buoyant jet for both two-dimensional and axisymmetric geometries. Brand and Lahey(1967) and Gebhart(1986) extended the analysis to include solutions for buoyant jets. The theoretical analyses of these limiting jets were studied in detail in 1950's and 60's. The theoretical approach was in most cases based on the similarity method, in which the independent variables in the governing equations are reduced to only one independent variable. The boundary-layer assumptions are assumed valid in thin jet regions which are not influenced by rigid boundaries but in which the viscous stresses are important. The analyses were based on the assumption of two dimensional flow. Kanury (1975) has presented a much simplified solution for both buoyant and non-buoyant axisymmetric and plane jet problems. He presented analytical solutions for both laminar and turbulent jets.

In general, extensive theoretical and experimental investigations have been conducted on circular jets and the literature on these jets is extensive [Kamal (1995)]. On the other hand very few studies have focused on jets issuing from non-circular geometries. Chih-ming and Gutmark (1987) in their study of small aspect ratio elliptic

jets found that in the major axis plane, the shear layer mainly spreads into the potential core of the flow, while the shear layer spreads more into the surrounding fluid in the minor axis plane. They found that in some cases the growth of the jet in the major axis actually decreased initially to some point; then it began to grow. In most cases the growth rate in the major axis remained constant before increasing. The faster growth of the minor axis was responsible for the axis-switching phenomena. The phenomena of axis switching is said to occur when the growth of the minor axis becomes equal to the growth of the major axis.

Hussain and Hussain (1989) performed a thorough experimental study of elliptic jets. They found that during the development of the jet axis switching between the minor and major axis can occur several times downstream of the jet. They pointed out that the axis-switching, which is typical of non-circular geometries, is responsible for the enhanced mixing that occurs in these jets and that by controlling this switching action passive control of some processes can be realized. They found that the jet spreads at a much higher rate in the minor axis direction than in the major axis direction causing the axes of the elliptic cross section to switch at some downstream location, where the jet-half widths in both the major and minor axes becomes equal. They also found that for elliptic geometries the best scaling parameter is the equivalent diameter of the jet, which they defined as the diameter of a circular jet with a momentum flux equal to that of an elliptic jet. Hussain and Hussain (1989) have also noted that the two dimensional plane jet and axisymmetric jet represent two limiting cases of elliptic jets (and possibly other 3-D jets) whose spread lies in between these two limiting cases.

Krothapalli et al. (1981) also found similar behavior of growth rate in their study of rectangular jets of various aspect ratios. They compared rectangular jets of aspect ratios 5.5, 8.3 and 12.5 and found that the growth rate in the minor axis increased linearly for all aspect ratios but the growth rate was lower for the smaller aspect ratios.

Excellent detailed experiments with a heated rectangular jet were carried out by Fijnen (1958). He carried out temperature measurement in a jet from a slit of 0.5 cm x 10 cm at a Reynolds number of 13300. His measurements indicated that the temperature profiles perpendicular to the major axis of the jet were 2-D and could be compared with 2-D theoretical results. He also found that when temperature profiles across the plane of the minor axis at various downstream distances are plotted in non-dimensional similarity parameters, they collapse into a single curve. This fact justified the use of simple similarity solution in solving the 2-D jet problem.

Follow-up work on heated rectangular jets includes that of Sfeir (1976), who measured both velocity and temperature in rectangular jets of various aspect ratios. He noted that the flow field for both velocity and temperature of the rectangular jet can be divided into three distinct regions referred to as the potential core, the two dimensional region, and the axisymmetric region. He found that the extent of these regions depended on the nozzle aspect ratio. At large distances from the nozzle exit, both velocity and temperature profiles were found to be similar to those of a circular jet. He also found that the flow in the 2-D region was practically independent of the nozzle aspect ratio. He used rectangular nozzles of aspect ratio 10, 20, and 30 and studied flow of a Reynolds number of 122,200 based on the length (shorter side) of the rectangular nozzle.

Sfeir (1976) also found that the three main regions of the jet flow mentioned above can be determined in terms of the centerline temperature decay. In the potential core region, the centerline temperature  $T_c$  was constant. This was followed by the 2-D region where  $(T_c)^2 \sim x^{-1}$  and finally the region corresponding to the circular jet where  $T_c \sim x^{-1}$ . Recently, Tarasov and Tolevor (1993) have presented results for a heated turbulent rectangular jet of aspect ratio 2.66. Their results are comparable to those of Sfeir (1976).

In summary, it is clear that an overwhelming majority on studies of non circular jets have considered turbulent flow conditions and geometry's of large exit dimensions (one cm and larger). Laminar flow conditions have been studied theoretically, and experimental data on laminar jets are scarce. In this study, we investigate the thermal development of a laminar buoyant rectangular jet.

The importance of the study of non-circular jets lies in their role in passive control of physical and chemical processes. Shadow et al. (1984) have presented a review on the role of active and passive control devices on combustion dynamics. Passive control was obtained by changing the initial conditions of the jet using non-circular 3-D geometries. Active control was achieved by an input of energy in the form of periodic waves of known frequencies. They have reported, using 2-D imaging techniques (for example Planar Laser Induced Fluorescence or PLIF) the presence of 3-D effects at low Reynolds numbers. They found that the effects of these 3-D interactions between vortices in simple axisymmetric combustion systems are a major mechanism in the breakdown of 2-D (axisymmetric) larger-scale structures into fine-scale 3-D turbulent structures.

Detailed understanding of these flames was possible using expensive laser based techniques such as PLIF and others (Chapter 1). Similar information can be extracted as shown in this work using the simpler rainbow schlieren technique (when extended to turbulence studies) in conjunction with modern image processing methods. The rainbow schlieren technique can be used to study the role of different passive or active control devices by studying the flames issuing from various geometries in the laboratory and then applying the results to real combustors to implement their beneficial effects. Studies on pollutant control are especially important. In the past it has been found that the non-circular geometries when applied to combustors suppressed pressure oscillations and extended the flammability limits [Shadow et al.(1984)].

Among the earlier numerical computations of free jets was the work of McGuirk and Rodi (1977) who applied the  $k-\epsilon$  turbulence model to the problem of jets issuing from rectangular nozzles. Using modern CFD techniques Givi (1989) has presented Direct Numerical Simulations (DNS) of reactive turbulent flows without using any turbulence model. Miller et al. (1995) have reported DNS of non-circular momentum jets. They considered elliptic, rectangular, and triangular jets of aspect ratio 1:1 and 2:1. They predicted axis-switching phenomenon in all non-unity aspect ratio jets. Grinstein and Kailasanath (1995) have presented a study on turbulent reactive square jets. The downstream development of the jet was evaluated with and without chemical reactions.. Once again the schlieren technique could be used to validate the models used in some these numerical simulations and to validate the results obtained.

## Chapter 3

### THEORY

In this section we discuss the principles of the rainbow schlieren technique with special reference to the form of projection data required for beam deflection tomographic algorithms. The application of the technique to 2-D axisymmetric objects will be discussed followed by the application of the technique to 3-D objects. The reconstruction algorithm applicable for schlieren data (beam deflection data) will be derived from the basic algorithm of the ordinary projection data.

#### 3.1 Principle of Schlieren Technique

The conventional schlieren technique depends on the deflection of light rays passing through a medium with a gradient of refractive index normal to the ray. The path of the ray is proportional to the refractive index gradient in the direction normal to the ray. Figure 3.1 shows a typical schlieren arrangement using lenses. The coordinate system is shown with the x-axis in the direction of the ray. With this coordinate system, the paths of the light ray in the xz and xy planes respectively are given by Merzkirch (1987) as

$$\frac{\partial^2 z}{\partial x^2} = \frac{1}{n} \frac{\partial n}{\partial z}$$

$$\frac{\partial^2 y}{\partial x^2} = \frac{1}{n} \frac{\partial n}{\partial y}$$



The total angular deflections in the  $z$  and  $y$  directions at the exit of the test sections become (see Appendix A.4 for derivation):

$$\begin{aligned}\epsilon_z &\simeq \frac{1}{n_o} \int \frac{\partial n}{\partial z} dx \\ \epsilon_y &\simeq \frac{1}{n_o} \int \frac{\partial n}{\partial y} dx\end{aligned}\tag{3.1}$$

where  $n_o$  is the refractive index of the surrounding medium. These deflections are in the direction of the increasing refractive-index gradient (i.e. towards the region of higher density). In this work, displacements were detected only in the  $y$  direction (all references to displacement in the rest of this dissertation will therefore correspond to the  $\epsilon_y$  deflection angle and the subscript  $y$  will be dropped).

In Figure 3.1, the source  $S$  is placed at the focus of the collimating lens  $C$  so that the test section is illuminated by a parallel beam of light. A second decollimating lens  $D$ , placed beyond the test section, produces an image of the source at its focal point,  $F$ , (or filter plane) beyond which a camera lens  $L$  is used to give an image of the test section at the recording plane of the camera. The light coming from every point in the test section in the  $yz$  plane gives an image of the source at the filter plane. If no gradients of refractive index are present in the test section, the images of the source formed by each ray from different points in the  $yz$  plane of the test section will coincide. However, if the refractive index of the medium differs from that of the surroundings, the deflection of the light will cause the corresponding source image at  $F$  to shift by an amount given by

$$d = f_c \tan \epsilon \simeq f_c \epsilon\tag{3.2}$$

where  $f_c$  is the focal length of the decollimating lens.

To obtain quantitative results using the conventional schlieren method, discrimination between grey scale levels is carried out. A schlieren photograph contains zones of grey tones varying in intensity from a maximum brightness to complete darkness depending upon the direction of deflection of the light rays. To determine these deflections quantitatively, it is necessary to evaluate the illumination density on the grey-scale schlieren photograph by means of photometry. In addition, a quantitative relationship between the intensity distribution and light deflection must be determined. This method, as pointed out in chapter 2, has some drawbacks including the fact that the grey scale is difficult to calibrate and read precisely and an unknown amount of error creeps in through the film processing of the recorded image. Also, the optics of the system must be flawless to reproduce the same light intensity at a given point accurately.

In the rainbow schlieren technique, a rainbow color filter is placed at the focal point F to measure the light ray displacements. A rectangular slit of sides  $a$  and  $b$  is used at the source. The image of this source of dimensions  $a$  and  $b$  is then formed at the focal point F. In the absence of any disturbances in the test section, the filter is adjusted such that the transmitted light through the filter to the recording plane is of a uniform hue. This is called the background hue, and the position of this hue on the filter is arbitrarily denoted by  $y_0$ . When disturbances are introduced in the test section, the image of the source shifts at the focal point as shown in Figure 3.1. This shifting results in the transmitted hue being different from the background hue, because now the source image falls at a different position on the filter. Depending on the orientation of the filter, deflections in the  $y$  and  $z$  directions can be detected. In this work, the filter orientation

was such that the displacements were detected only in the  $y$  (lateral) direction as mentioned above. Using a previously calibrated filter it is then possible to determine the displacement distance,  $d$ , from which the deflection angle,  $\epsilon$ , can be calculated. The procedure of manufacturing the filter and its optimization will be discussed in chapter 4 on experimental methods.

Hue,  $h$ , is a parameter describing color. The most popular model to describe color is the red, green, and blue (RGB) model. In the RGB model, the color is quantified in terms of the percentages of its red, green, and blue components. To describe color by a single parameter, instead of RGB, the hue, saturation, and intensity (HSI) model is used. In the HSI model, the hue describes a color in the color spectrum, or on a color wheel in degrees or radians varying from 0 to  $2\pi$ . Each number represents a particular color mix of the RGB. Greenberg et al.(1995) give the equation relating RGB to hue as:

$$h = \cos^{-1} \left[ \frac{0.5 [(R - G) + (R - B)]}{[(R - G)^2 + (R - B)(G - B)]^{\frac{1}{2}}} \right] \quad (3.3)$$

In the HSI color model, a cylindrical system of coordinates is chosen for all colors. In this coordinate system, the radius represents saturation, the angle represents hue and the  $z$ -coordinate represents the intensity [William (1972)]. A filter is thus created with the hue linearly distributed across the width of the filter, while keeping the intensity and saturation at any arbitrarily fixed value. This means that a light ray falling on any point in the filter will transmit a unique hue, independent of the intensity and saturation on to the image plane. By relating this hue to displacements (via the calibration curve), the

deflection angle  $\epsilon$  can be determined. A photograph of the asymmetric filter is shown in Appendix B.1.

Sensitivity of rainbow schlieren: The filter was created such that the hue transmitted,  $h$  varied linearly in the operating range of the filter. Thus:

$$\frac{dh}{dx} = \text{constant} = -\frac{2\pi}{y_{\max}}$$

where  $y_{\max}$  is the overall desired dimension of the filter or width of the filter region.

The sensitivity of the rainbow schlieren can be determined using the procedure described by Weinberg (1963). Let the hue transmissivity of the filter after optimization, as described by Greenberg et al. (1995), be given by the equation:

$$h = K'y + C'$$

where  $K'$  and  $C'$  are constants and  $y$  is the lateral position on the filter with an arbitrarily chosen origin. Let the background hue be denoted by  $h(y_o)$ . Then, for an undisturbed index field the transmitted hue becomes:

$$h(y_o) = K'y_o + C'$$

With disturbance, the transmitted hue becomes

$$h = K'(y_o + d) + C'$$

The change in hue is :

$$\Delta h = K'd$$

$$\Delta h = K'f_c\epsilon \quad (3.4)$$

The sensitivity of the schlieren system is then given by:

$$\frac{d(\Delta h)}{d\epsilon} = K' f_c \quad (3.5)$$

The factors that affect the sensitivity are the size of the filter in relationship to the size of the slit source, and the focal length of the decollimating lens. By increasing the slope ( $K'$ ) of the calibration curve of the filter, the sensitivity can be increased. The calibration curve used in this study is shown in Figure 3.2. It had a  $K'$  value of 261 degrees/mm. This was determined with a least squares linear fit with a correlation coefficient of 0.995.

The  $y_0$  position corresponding to the undisturbed image hue  $h(y_0)$  given above should ideally be a single point on the filter for a point source of light. Since the source is finite, the filter should be adjusted such that  $y_0$  is within a region on the filter of a uniform hue. This means that the size of the slit source image should cover a uniform hue region on the filter. Therefore, the size of the source slit and the size of the filter are two important parameters that affect the performance of a given filter. The design of these two parameters will influence the desired color contrast, color coding, resolution, sensitivity and measurement range of any given system [Settles(1985)].

Before discussing the inversion of schlieren data, the basic problem of inversion of data for a general object function  $f(x,y)$  will be discussed and the form of the integral equations to be solved will be shown. The equations for the inversion of schlieren data will then be derived with reference to these basic integral equations.

### 3.2 The Radon Transform and Line Integral Data

In Figure 3.3 an object whose property  $f(x,y)$  is to be determined is divided into rectangular fine grids, or pixels. The property  $f(x,y)$  is assumed constant at each grid (pixel) point. The property  $f(x,y)$  is to be determined from projections of a set of rays passing through the object and recorded on the image plane. The recording represents the total integral (or line integral) of the property interaction with the ray traversing the object. The data recorded for each ray are given by  $p(\theta,t)$  where  $\theta$  is the direction of the ray and  $t$  is the distance from the origin in the object plane as shown in Figure 3.3. The measured data,  $p(\theta,t)$  like the object are given by a 2-D function. However, the independent variables for the projection data are different from those for the object. The problem of reconstruction is complicated by the fact that the object cross-sectional field and projection data are defined in different coordinate systems.

The projection data are defined by a one dimensional coordinate for a given angle of view,  $\theta$ . The object cross sectional field is defined by a 2-D function  $f(x,y)$  in rectangular coordinates. Figure 3.3 also shows the schematic representation of these two coordinate systems. The problem of computer tomography is to reconstruct the object field function values  $f(x,y)$  from projection data,  $p(\theta,t)$ , taken at various viewing angles. The projection data are a linear combination of the object values. Therefore, the process of collecting projection data can be considered as a transform in which the object data are linearly combined to obtain the projection data [Dean(1983)]. This transform is termed as the Radon transform. The process of reconstructing the object from projection data is then the inverse Radon transform. We can say that the Radon transform, transforms a

signal from the coordinate system of the object domain into the coordinate system of the projection (ray sum) domain.

In Figure 3.3, if the rays are parallel to the x-direction, i.e.  $\theta=0$ , then the recording image plane will be in the y direction. We then have:

$$p(0, y) = \int_{-\infty}^{\infty} f(x, y) dx \quad (3.6)$$

where x represents the ray path through the object.

If the rays are not along the x-axis but form an angle  $\theta$  with it, then the integrals will be computed along 't' given by

$$-x \sin \theta + y \cos \theta = t$$

where t is the distance of the ray from the origin. Then we have

$$p(\theta, t) = \int_{-\infty}^{\infty} \int_{-\infty}^{\infty} f(x, y) \delta(-x \sin \theta + y \cos \theta - t) dx dy \quad (3.7)$$

The delta function  $\delta$  is used to account for the fact that the locations where the ray does not pass through will contribute zero to the integral. Analytically, the image reconstruction process is simply solving a set of line integral equations at different angles of  $\theta$  and finding the distribution function  $f(x, y)$  within the object. A set of  $p(\theta, t)$  functions results from obtaining many projections of the source function  $f(x, y)$  at incremental values of angular rotation  $\theta$ .

Beam deflection data: In the rainbow schlieren technique, when a beam passes through a test object and is deflected due to the refractive index gradients, the amount of deflection or the deflection angle of the beam as it exits the test section is related to the

refractive index  $n(x,y)$  of the field. Consider the refractive index field shown in Figure 3.4. In this figure, let  $n_o$  = refractive index outside the object field. Then define

$$n_d = n - n_o$$

where  $n$  is the refractive index within the object.  $n$  and  $n_d$  are functions of  $t$ , and  $s$  (referring to rotated coordinates of Figure 3.4)

$$n = n_d + n_o$$

$$n = n_o \left( \frac{n_d}{n_o} + 1 \right)$$

$$n = n_o (\bar{n} + 1)$$

where  $\bar{n}$  is the normalized refractive index difference. From Figure 3.4, it can be shown that equation 3.1 becomes.

$$\epsilon(\theta, t) \simeq \frac{1}{n_o} \int_{-\infty}^{\infty} \frac{\partial n}{\partial t} ds \quad (3.8)$$

From the above definition of the normalized refractive index difference this equation becomes

$$\epsilon(\theta, t) \simeq \int_{-\infty}^{\infty} \frac{\partial \bar{n}(t, s)}{\partial t} ds \quad (3.9)$$

Interchanging the order of integration and differentiation we obtain:

$$\epsilon(\theta, t) \simeq \frac{d}{dt} \int_{-\infty}^{\infty} \bar{n}(t, s) ds \quad (3.10)$$

Comparing this equation with equation 3.6 or 3.7, we note that the projection data are obtained by a linear combination of object values followed by its derivative in a direction



normal to the rays. Performing the normal Radon transform, we obtain the ordinary projection data equation:

$$p(\theta, t) = \int_{-\infty}^{\infty} \bar{n}(t, s) dt \quad (3.11)$$

The basic inversion problem then becomes that of inverting equation 3.11 (which is similar to equation 3.6 applicable for any arbitrary object function  $f(x,y)$ ) and taking the derivative of the result. Inversion of equation 3.11 is the basic tomographic reconstruction problem which we will term the problem of ordinary projection data. The inversion of equation 3.10 will be called the problem of beam deflection data. Several techniques have been developed for inverting equation 3.11. We shall show how the algorithms for inverting equation 3.11 can be modified to invert the beam deflection data. Equations 3.10 and 3.11 are applicable for symmetric or asymmetric test objects. For axisymmetric objects, simpler techniques of inversion can be used.

### 3.3 Inversion of Axisymmetric or 2-D Fields

When equation 3.9 is written in rectangular coordinates  $(x,y)$  it becomes

$$\epsilon = \int_{-\infty}^{\infty} \frac{\partial \bar{n}(y)}{\partial y} dx$$

For an axisymmetric refractive index field, the inversion of this equation has the form of the classical Abel inversion formula. When this equation is transformed into cylindrical coordinates (see Figure 3.5) we obtain following, Song and Guo (1993):

$$\epsilon = 2y \int_y^{\infty} \frac{d\bar{n}}{dr} \frac{dr}{(r^2 - y^2)^{\frac{1}{2}}}$$

The inverse transform of this equation is given by

$$\tilde{n}(r) - 1 = -\pi \int_r^{\infty} \frac{\epsilon dy}{(y^2 - r^2)^{\frac{1}{2}}} \quad (3.12)$$

Equation 3.12 is used in the Abel transform method. The other method used for inverting the axisymmetric fields is the onion peeling reconstruction technique which is a numerical method [Dasch (1992)]. In this method, the field is divided into concentric rings. Within each ring the flow field is assumed to be uniform and a group of algebraic equations is set up and solved simultaneously for the unknown refractive index. The Abel transform and onion peeling methods are suitable only for axisymmetric fields. Actual implementation of the integrations could be difficult because of the singularity of equation 3.12 at  $y=r$ .

### 3.4 Inversion of Asymmetric or 3-D Fields:

Equation 3.11 can be written in the form of equation 3.7 as

$$p(\theta, t) = \int_{-\infty}^{\infty} \int_{-\infty}^{\infty} \tilde{n}(x, y) \delta(-x \sin \theta + y \cos \theta - t) dx dy \quad (3.13)$$

In general, tomographic methods can be classified into four groups [Xie (1995)]:

1. Matrix inversion
2. Algebraic reconstruction techniques (ART)
3. Fourier Transform method
4. Convolution Backprojection method.(CBP)

Matrix inversion involves dividing the region of interest into cells (pixels), setting up linear equations relating the object value at each cell location  $\tilde{n}(x,y)$  to the experimental projection data at each angle of view  $p(\theta,t)$ . The resulting equations are then solved by direct matrix inversion techniques. This method cannot be applied where there is no exact solution, such as when there are more projections than cells and the data contain noise. Such over-determination with noisy data is common in tomography, so this method is generally not used. Another disadvantage of the matrix inversion method is the very large size of the array of the coefficients of the unknowns.

Algebraic reconstruction techniques (ART) including series expansion techniques start with a set of cell locations and linear equations, similar to the matrix inversion technique. However, the solution is found by iteration rather than by direct matrix inversion. An initial guess is made for the object values  $\tilde{n}(x,y)$  in each cell. The corresponding projection for the ray paths is then calculated and compared with the experimental data. The differences between the calculated and experimental projection data are used in calculating correction factors to be applied to the initial guesses. This procedure is repeated until some convergence or limit criterion is reached.

Fourier transform reconstruction takes advantage of the relation between the Fourier transform of the projection data and the object. The Fourier slice theorem Herman (1980) serves as a basis for direct Fourier reconstruction algorithm. This theorem is based on the fact that 1-D projections of an object field provide information about spatial frequencies present in the object. Many projections appropriately chosen may then be used to determine the spatial frequency representation of the entire object. Once the

spatial frequency distribution of the object has been determined, an inverse Fourier transform of these frequency distributions will yield the desired reconstruction of the object.

The convolution backprojection (CBP) method involves taking the projections  $p(\theta, t)$ , and convolving them with a suitably chosen weighting function. The weighting function usually depends upon the spatial coordinate. The choice of the weighting function is based on the Fourier inversion formula. After convolving with the weighting function, the resulting “filtered” projections are backprojected onto the object plane.

The commonly used techniques for reconstruction are the ART and CBP. If the Nyquist sampling criteria can be met, (i.e. projections are available over all view angles), the CBP technique gives better accuracy and spatial resolution than do the ART techniques [Oppenheim (1977)]. However, for certain oscillatory functions and noisy measurements and in case of limited view projections, the iterative methods produce more accurate reconstructions [Oppenheim (1977)]. With the direct Fourier transform method, a major difficulty is in the choice of the interpolation function to convert from polar samples to Cartesian coordinates. In this work the CBP reconstruction technique was, therefore, chosen.

### **3.5 The Convolution Backprojection Method**

The convolution backprojection (CBP) algorithm is related to the direct Fourier reconstruction algorithm. For this reason, we shall first describe the direct Fourier algorithm and then derive the convolution backprojection algorithm.

The Radon transform [Deans (1983)] or the line integral, and the Fourier slice theorem serve as the basis of the direct Fourier reconstruction algorithm. We shall define the Fourier transform, briefly describe the Fourier slice theorem and then show how they are used in the direct Fourier reconstruction algorithm.

The 2-D Fourier transform of an object function  $\tilde{n}(x,y)$  is defined by Weaver(1983):

$$\tilde{N}(u, v) = \int_{-\infty}^{\infty} \int_{-\infty}^{\infty} \tilde{n}(x, y) e^{-i2\pi(ux+vy)} dx dy \quad (3.14)$$

where  $u$  and  $v$  are the frequency components in the frequency domain.

The 2-D inverse Fourier transform is given by

$$\tilde{n}(x, y) = \int_{-\infty}^{\infty} \int_{-\infty}^{\infty} \tilde{N}(u, v) e^{i2\pi(ux+vy)} du dv \quad (3.15)$$

Equation 3.15 suggests that, if we know the Fourier transform of the object field, we can determine the unknown function  $\tilde{n}(x,y)$  by taking its inverse Fourier transform. The Fourier slice theorem helps us determine  $\tilde{N}(u,v)$  from projections  $p(\theta,t)$ .

The Fourier slice theorem: The Fourier slice theorem can be stated as follows: the Fourier transform of a projection through an object function  $\tilde{n}(x,y)$  taken at an angle  $\theta$  with the  $x$ -axis gives a slice of the 2-D Fourier transform,  $\tilde{N}(u,v)$ , subtending an angle  $(\theta+90)$  with the  $u$ -axis [Dudgeon and Mersereau (1984)]. In other words, the Fourier transform of  $p(\theta,t)$  defined as

$$S(\theta, \omega) = \int_{-\infty}^{\infty} p(\theta, t) e^{-i2\pi\omega t} dt \quad (3.16)$$

where

$$\omega = \sqrt{u^2 + v^2}$$

gives the values of  $\tilde{N}(u,v)$  along line AA' in Figure 3.6 at an angle of  $(\theta+90)$  with the u-axis. Consider the Fourier transform of the object along the line in the frequency domain given by  $u=0$ . The Fourier transform integral becomes

$$\tilde{N}(0, v) = \int_{-\infty}^{\infty} \int_{-\infty}^{\infty} \tilde{n}(x, y) e^{-i2\pi(0x+v.y)} dx dy$$

The order of integrals may be rearranged to obtain;

$$\tilde{N}(0, v) = \int_{-\infty}^{\infty} \left[ \int_{-\infty}^{\infty} \tilde{n}(x, y) dx \right] e^{-i2\pi v y} dy$$

the term in brackets is the formula for a projection along lines of constant y i.e.  $p(\theta=0,y)$  as shown by equation 3.6. Substituting for these projections we obtain

$$\tilde{N}(0, v) = \int_{-\infty}^{\infty} p(\theta = 0, y) e^{-i2\pi v y} dy$$

The right hand side of this equation represents the 1-D Fourier transform of the projection  $p(\theta=0,t)$ . Thus, the relationship between the projections and its 2-D Fourier transform of the object function can be expressed by the Fourier slice theorem as

$$\tilde{N}(0, v) = S(0, v)$$

This proves the Fourier slice theorem. If as shown in Figure 3.3 the coordinate system is rotated by an angle  $\theta$ , the Fourier transform of the projection is equal to the two-dimensional Fourier transform of the object along a line rotated by  $\theta$  as shown in Figure 3.6.

To reconstruct an image from projections using the direct Fourier algorithm, projections at a number of different angles are required to obtain the frequency samples at different radial lines using the 1-D Fourier transform of each projection. By taking the 1-

D Fourier transform of the measured projection data  $p(\theta, t)$  (equation 3.16 above) one can determine a 2-D polar form of frequency samples in the Fourier space. At this point, the spatial frequency values are known along the radial lines in frequency domain. These frequency values, therefore, can be defined as frequency samples of the original object. Essentially, the spatial frequency function has been sampled in a manner determined by the angle  $\theta$  between individual rotation views. The value at the origin  $S(0, 0)$  will, however, be  $N$  times too large (because each radial line passes through it) for  $N$  being the number of rotation angles or views. This can be corrected by dividing this point value by  $N$ . The frequency samples determined in this way are shown in Figure 3.7.

This suggests that by taking the projections of an object function at angles  $\theta_1, \theta_2, \dots, \theta_i, \dots, \theta_N$  and Fourier transforming each of the projections, one determines the frequency values  $\tilde{N}(u, v)$  along radial lines as shown in Figure 3.7. If an infinite number of projections are taken, then  $\tilde{N}(u, v)$  would be known at all points in the frequency domain. Therefore, knowing  $\tilde{N}(u, v)$ , the original object function  $\tilde{n}(x, y)$  can be recovered by performing a 2-D inverse Fourier transform using equation 3.15. In practice a discrete inverse Fourier transform of equation 3.15 is used. If we assume  $M$  to be an even integer, determining the size of a square image matrix, then

$$\tilde{n}(x, y) = \frac{1}{A^2} \sum_{m=-M/2}^{M/2} \sum_{n=-M/2}^{M/2} \tilde{N}\left(\frac{m}{A}, \frac{n}{A}\right) e^{i2\pi\left(\left(\frac{m}{A}\right)x + \left(\frac{n}{A}\right)y\right)}$$

where  $A$  is the physical measure of the object. For example  $-A/2 < x < A/2$  and  $-A/2 < y < A/2$ . This summation can be rapidly implemented by using the Fast Fourier

Transform (FFT) technique provided the  $N^2$  Fourier coefficients  $\tilde{N}(m/A, n/A)$  are known [Mersereau and Oppenheim(1974)].

Figure 3.8 illustrates the concept of the direct Fourier reconstruction process. One of the difficulties in this method is the choice of the interpolating function to convert the polar samples to a rectangular coordinate system. Interpolation technique, therefore, is an important component for implementing the direct Fourier reconstruction algorithm to achieve the desired imaging quality.

In general, the method involves taking the 1-D Fourier transform of the measured projection data  $p(\theta, t)$  and interpolating the data to a rectangular grid. After interpolating the frequency data, a standard FFT algorithm is used to invert the frequency data to the object space domain values. We shall now show the relationship between this algorithm and the convolution backprojection algorithm (CBP).

To derive the convolution backprojection (CFB) algorithm, we begin with equation 3.15. Transforming the rectangular coordinate system in the frequency domain  $(u, v)$ , to a polar coordinate system  $(\theta, \omega)$ , by making the substitutions  $u = \omega \cos \theta$ ,  $v = \omega \sin \theta$  and  $du dv = \omega d\omega d\theta$ ,

$$\begin{aligned}\omega &= \sqrt{u^2 + v^2} \\ \theta &= \arctan\left(\frac{v}{u}\right)\end{aligned}\tag{3.17}$$

Then the object function is defined in polar coordinates as

$$\tilde{n}(x, y) = \int_0^{2\pi} \int_0^\infty S(\theta, \omega) e^{i2\pi\omega(y\cos\theta - x\sin\theta)} \omega d\omega d\theta$$



This integral can be solved in two parts by considering  $\theta$  from 0 to  $\pi$  and then from  $\pi$  to  $2\pi$ , [Kak and Slaney, (1988)]

$$\begin{aligned}\bar{n}(x, y) = & \int_0^\pi \int_0^\infty S(\theta, \omega) e^{i2\pi\omega(y\cos\theta - x\sin\theta)} \omega d\omega d\theta \\ & + \int_0^\pi \int_0^\infty S(\theta + \pi, \omega) e^{i2\pi\omega(y\cos(\theta+\pi) - x\sin(\theta+\pi))} \omega d\omega d\theta\end{aligned}$$

now using the property

$$S(\theta + \pi, \omega) = S(\theta, -\omega)$$

the above equation may be written as

$$\bar{n}(x, y) = \int_0^\pi \int_{-\infty}^\infty [S(\theta, \omega) |\omega| e^{i2\pi\omega t} d\omega] d\theta \quad (3.18)$$

At this point we have two possibilities to determining for  $S(\theta, \omega)$ . For ordinary projections, the frequency spectrum  $S(\theta, \omega)$  is the Fourier transform of projections  $p(\theta, t)$

$$S(\theta, \omega) = \int_{-\infty}^\infty p(\theta, t) e^{-i2\pi\omega t} dt \quad (3.19)$$

where,  $p(\theta, t)$  are given for an arbitrary object function  $f(x, y)$ , by equation 3.7. For beam deflection data, the projection data is given by  $\epsilon(\theta, t)$ , of equation 3.10 and repeated below as

$$\epsilon(\theta, t) \simeq \frac{d}{dt} \int_{-\infty}^\infty \bar{n}(t, s) ds \quad (3.10)$$

Take the Fourier transform of both sides of equation 3.10. To do this we use the derivative property of the Fourier transforms. This property states that if  $f(x)$  has the Fourier transform  $F(s)$  then its derivative  $f'(x)$  has the Fourier transform  $i2\pi sF(s)$  [Bracewell (1986)], thus;

$$E(\theta, \omega) = i2\pi\omega S(\theta, \omega) \quad (3.20)$$

where  $E(\theta, \omega)$  is the Fourier transform of deflection angles  $\epsilon(\theta, t)$ .

Now substituting for  $S(\theta, \omega)$  in equation 3.18 from equation 3.20 we obtain

$$\tilde{n}(x, y) = \int_0^\pi \int_{-\infty}^{\infty} E(\theta, \omega) e^{i2\pi\omega t} K(\omega) d\omega d\theta \quad (3.21)$$

where

$$K(\omega) = \frac{-i|\omega|}{2\pi\omega} = \begin{cases} \frac{i}{2\pi} & \omega < 0 \\ \frac{-i}{2\pi} & \omega > 0 \end{cases}$$

The inner integral in equation 3.21 is equivalent to taking the convolution of the inverse Fourier transform of  $E(\theta, \omega)$  which is the projection angles  $\epsilon(\theta, t)$  with the inverse Fourier transform of  $K(\omega)$ .

That is:

$$\tilde{n}(x, y) = \int_0^\pi \int_{-\infty}^{\infty} \epsilon(t, \theta) q(y\cos\theta - x\sin\theta - t) dt d\theta \quad (3.22)$$

where the function  $q(\cdot)$  is the inverse Fourier transform of  $K(\omega)$ . The inner integral represents the convolution (defined next) of the deflection data with the convolving function  $q(\cdot)$ .

Convolution function: The convolution between two functions  $f(x)$  and  $g(x)$  is given by

$$h(x) = \int_{-\infty}^{\infty} f(u)g(x - u)du$$

This is often denoted by

$$h(x) = f(x) * g(x)$$

$h$ ,  $f$  and  $g$  are functions of the same variable  $x$ , which can be a time or spatial coordinate.

For discrete functions, the convolution is evaluated as follows [Bracewell (1986)]:

consider two functions, each representing a series in integers

$$f(x) = a_x \quad x = 0, 1, 2, \dots, m$$

and

$$g(x) = b_x \quad x = 0, 1, 2, \dots, n$$

The convolution between these two functions is given by:

$$h_{i+1} = \sum_{j=1}^m a_j b_{i-j} \quad (3.23a)$$

The number of terms in the convolution function is one less than the sums of the numbers of terms in  $f$  and  $g$  (i.e.  $i=0 \dots m+n-2$ ).

Now consider the function  $q(\cdot)$ , which is the inverse Fourier transform of  $K(\omega)$ .  $K(\omega)$  is not a well behaved function for its inverse Fourier transform to exist. In practice, however, the object field is band-limited by the measuring system. i.e. the frequency extent of the projection data is limited. So if the maximum frequency component of

$S(\omega, \theta)$  is  $\omega_{\max}$ , then  $K(\omega)$  can be similarly truncated. Thus, we need the inverse Fourier transform  $q(t)$  of  $K(\omega)$ , where

$$K(\omega) = 0 \quad \omega \geq |\omega_{\max}|$$

and

$$K(\omega) = \begin{cases} \frac{t}{2\pi} & -\omega_{\max} < \omega < 0 \\ \frac{-t}{2\pi} & 0 < \omega < \omega_{\max} \end{cases}$$

or

$$q(t) = \int_{-\omega_{\max}}^{\omega_{\max}} K(\omega) e^{2\pi i \omega t} d\omega$$

Integration of this equation gives:

$$q(t) = \frac{1}{\pi^2 t} \sin^2(\pi t \omega_{\max}) \quad (3.23b)$$

For discrete values of  $t=ma$ , where  $a$  is the sample spacing, this equation becomes:

$$\begin{aligned} q(ma) &= 0 & m &= 0 \\ q(ma) &= (\pi^2 ma)^{-1} & m &= \text{odd} \\ q(ma) &= 0 & m &= \text{even} \end{aligned} \quad (3.24)$$

The samples must meet the Whittaker-Shannon sampling theorem [Bracewell (1986)] which states that a band-limited function with maximum frequency component  $\omega_{\max}$  can be completely represented by, and reconstructed from, a set of uniform samples at spacing 'a', where  $a \leq (2\omega_{\max})^{-1}$ . Using  $a = (2\omega_{\max})^{-1}$ ,  $ma$ , denotes the positions along  $t$  (refer to coordinate system of Figure 3.3) at which the discrete convolution function is defined. The projection data are sampled at uniform intervals, so that equation 3.22 can be replaced by its discrete counterpart.

$$n - n_o = n_o \sum_{n=1}^N \frac{\pi}{N-1} \sum_{m=1}^M \epsilon\left(ma, \frac{n\pi}{N-1}\right) q(y\cos\theta - x\sin\theta - ma)a \quad (3.25)$$

for N projections of M rays each.

Equations 3.24 and 3.25 represent the convolution backprojection algorithm for beam deflection data. This last equation represents two steps: first, the convolution given by the inner integral and then, the backprojection at angles from 0 and  $\pi$  represented by the outer integral. Since the sampled projection data are used in the practical implementation, a one-dimensional interpolation is required before backprojection because the projection samples cannot be back projected to the exact Cartesian grid (see Figure 3.9).

Implementation of the algorithm: The basic algorithm for reconstruction of the object function from projections,  $\epsilon(\theta, t)$ , at multiple views starts with convolving the projection data with the convolution function discussed above and given by equation 3.25. Let the number of rays at each projection angle be represented as  $t_1, t_2, t_3, \dots, t_l, \dots, t_M$  where M is the number of rays per projection. Then, the convolved projection data become:

$$b(\theta, t_l) = \sum_{k=-\frac{M}{2}}^{\frac{M}{2}} \epsilon(\theta, t_l) q(t_l - t_k) \quad (3.26)$$

which is equivalent to the inner integral of equation 3.22. This step is also known as the convolution step and is implemented as given by equation 3.23. Now, we wish to reconstruct the object values,  $\tilde{n}_{ij}$  from the convoluted projections  $b(\theta, t)$ . It is seen from

Figure 3.9 that the sampled projection data  $b(\theta, t)$  cannot be back projected to the exact Cartesian grid of the object matrix. Because of this, one-dimensional interpolation is required before backprojection. The interpolated values of  $b(\theta, t)$  are then backprojected as shown in Figure 3.10. The new interpolated values of projection  $b'(\theta, t)$  are calculated for a fixed  $\theta$  from the equation:

$$b'(t) = \sum_{k=-\frac{M}{2}}^{\frac{M}{2}} h(t_k - t)b(t_k)$$

where  $h(t)$  is an interpolation kernel. Using linear interpolation we obtain

$$b'(\theta, t) = \frac{a}{t_{l+1} - t_l} [(t_{l+1} - t)b(t_l, \theta) + (t - t_l)b(t_{l+1}, \theta)] \quad (3.27)$$

where  $a$  is the sample spacing and;

$$t_l < t \leq t_{l+1}$$

$b'(t, \theta)$  is the value that is backprojected to the  $(x, y)$  coordinate of the object array for a particular value of  $t$ . The final reconstructed estimate of  $\tilde{n}(x, y)$  is obtained by summing the interpolated convolutions over the viewing angles from 0 to  $\pi$  as given in equations 3.22 and 3.25.

As a final step, the refractive index is related to density using the Gladstone-Dale constant equation

$$n - 1 = K\rho \quad (3.28)$$

where  $n$  is the refractive index,  $K$  is the Gladstone-Dale constant and  $\rho$  is the density [Merzkirch (1987)]. The temperature is then related to the density using the ideal gas law.

Ordinary projection data: The convolution backprojection algorithm was programmed, and its performance validated by reconstruction of simple test objects (phantoms). The reconstruction algorithm for ordinary projections was also derived following similar steps with a slight modification. The starting point for the derivation is equation 3.18.

$$f(x, y) = \int_0^\pi \int_{-\infty}^{\infty} S(\theta, \omega) e^{i2\pi\omega(y\cos\theta - x\sin\theta)} |\omega| d\omega d\theta \quad (3.18)$$

The frequency spectrum  $S(\theta, \omega)$  can be substituted by the Fourier transform of projections  $p(t, \theta)$

$$S(\theta, \omega) = \int_{-\infty}^{\infty} p(\theta, t) e^{-i2\pi\omega t} dt \quad (3.19)$$

after changing the order of integration

$$f(x, y) = \int_0^\pi \int_{-\infty}^{\infty} p(\theta, t) \int_{-\infty}^{\infty} e^{i2\pi\omega(y\cos\theta - x\sin\theta - t)} |\omega| d\omega dt d\theta$$

In the spatial domain, using the convolution theorem this is equivalent to

$$f(x, y) = \int_0^\pi \int_{-\infty}^{\infty} p(\theta, t) q(y\cos\theta - x\sin\theta - t) dt d\theta \quad (3.29)$$

where  $q(y\cos\theta - x\sin\theta - t)$  is the inverse Fourier transform of  $|\omega|$  also called the ramp function. This last equation again represents two steps: first, the convolution of the inner integral and then, the backprojection at angles from 0 and  $\pi$ . A one dimensional interpolation is required before backprojection because the projection samples cannot be back projected to the exact Cartesian grid (see Figure 3.9).

Now consider the convolution function  $q(t)$ , which is the inverse Fourier transform of the ramp function,  $|\omega|$ .  $|\omega|$  is not a well behaved function for its inverse Fourier transform to exist. In practice, however, the object field is band-limited by the measuring system. i.e the frequency extent of the projected data is limited. So if the maximum frequency component of  $S(\theta, \omega)$  is  $\omega_{\max}$  then  $\omega$  can be similarly truncated. Thus, we need the transform  $q(t)$  of  $K(\omega)$ , where

$$\begin{aligned} K(\omega) &= 0 & \omega &\geq \omega_{\max} \\ K(\omega) &= \omega & \omega < \omega_{\max} \end{aligned}$$

or

$$q(t) = \int_{-\omega_{\max}}^{\omega_{\max}} |\omega| e^{2\pi i \omega t} d\omega$$

Integration by parts of this equation gives:

$$q(t) = \omega_{\max}^2 [2\text{sinc}(2\omega_{\max}t) - \text{sinc}^2(\omega_{\max}t)]$$

where the function sinc is defined as :

$$\text{sinc } x = \sin \pi x / \pi x$$

and its properties are such that

$$\text{sinc } 0 = 1$$

$$\text{sinc } n = 0 \quad n = \text{nonzero integer}$$

$$\int_{-\infty}^{\infty} \text{sinc } x dx = 1$$

This function contains components of all frequencies up to  $\omega_{\max}$  or the cut off frequency. During convolution it removes all frequency components above its cut off and leaves all below unaltered, [Bracewell (1986)]. The convolution ramp function used for ordinary projection is shown in Figure 3.11 together with the convolution function used



with beam deflection data. These functions represent the differences between the reconstruction algorithm for ordinary projections and for the beam deflection algorithm.

Now the practical implementation of the convolution backprojection (CBP) algorithm requires that the integral in equation 3.29 be replaced by a discrete summation because the projection data are discretely sampled. Following the procedure used for beam deflection data, the ramp function for the ordinary projection data becomes.

$$\begin{aligned} q(ma) &= 0 & m \text{ even, } m \neq 0 \\ q(ma) &= -(\pi ma)^{-2} & m \text{ odd} \\ q(ma) &= -(2a)^{-2} & m = 0 \end{aligned} \quad (3.30)$$

where,  $ma$ , denotes the position along  $t$  at which the discrete function  $q(\cdot)$  is defined. The projection data are sampled at uniform intervals so that equation 3.29 can be replaced by its discrete counterpart.

$$f(x, y) \cong \sum_{n=1}^N \frac{\pi}{N-1} \sum_{m=1}^M p(ma, \frac{n\pi}{N-1}) q(y \cos \theta - x \sin \theta - ma) a \quad (3.31)$$

for  $N$  projections of  $M$  rays each.

Backprojection: Now the outer summation of equation 3.31 represents the process of backprojection in which convolved projections are distributed over the  $(x, y)$  space. From the single ray sum (projection) value, there is no information about which pixels in the object field along the ray contributed how much to the sum. Therefore, during backprojection, the value of the ray sum is distributed equally to each pixel along the ray. At a single projection angle, the backprojected data will vary along the  $t$  direction, but not along the  $s$  direction. In other words, the curve in the  $P$ - $t$  plane (image projection plane) is translated along the direction of the  $t$ -axis onto the object field to create a cylindrical

surface. The resulting surface above the object cross-section is viewed as a function of two variables,  $x$  and  $y$  and is termed the backprojection. The reconstruction for each point  $(x,y)$  is obtained by summing the backprojection values for all the view angles as shown in equation 3.31. The backprojection for each point  $(x,y)$  is determined by interpolation as described above for the beam deflection algorithm.

### 3.6 The Phantom Test Objects

In this section, we present the test objects used to validate the reconstruction algorithms. The two algorithms, one for the ordinary projection data and the other for the beam deflection data, were validated using appropriate phantom data. To avoid numerical integration errors along rays through the objects, the test objects were chosen such that their projections could be determined analytically.

Ordinary projection data: The phantom object chosen to validate the ordinary projection algorithm of equation 3.31 was an elliptic cross-sectional object of uniform density. The projection data through the object are then simply the lengths of the rays inside the ellipse, normalized appropriately. For an elliptic cross-section object, the length of straight rays passing through the object can be written analytically. Let  $g(x,y)$  describe the density of the elliptical object of major axis dimension  $A$  and minor axis dimension  $B$ , see Figure 3.12

$$g(x, y) = \begin{cases} \rho & \text{for } \frac{x^2}{A^2} + \frac{y^2}{B^2} \leq 1 \\ 0, & \text{otherwise} \end{cases}$$

The projection, or the length of each ray inside the ellipse is given by Kak and Slaney (1988)

$$p(\theta, t) = \begin{cases} [2\rho AB/e^2] \sqrt{e^2 - t^2} & \text{for } |t| \leq e \\ 0, & \text{for } |t| > e \end{cases} \quad (3.32)$$

where

$$e^2 = A^2 \cos^2 \theta + B^2 \sin^2 \theta$$

Note that, the variable  $e$  is a function of the projection angle  $\theta$ . Using these equations, the projections were computed and stored in a two dimensional array,  $p(i,j)$  where  $i$  represents the ray and  $j$  represents the projection angle. These projections are shown in Figure 3.14a.  $N$  number of projections and  $M$  number of samples (or rays in each projection) were generated for the ellipse. The projection data were read in and then centered about the origin as shown in Figure 3.13. The projection data were then convolved using the convolution function equation 3.30. The convolved projection data are shown in Figure 3.14a. Backprojection of the convolved data using equation 3.31 results in Figure 3.14b which shows the reconstruction of the ellipse of dimension  $A=30$  units and  $B = 15$  units. The major steps of the reconstruction algorithm are shown in Appendix A.3. The number of rays used was 64 and the number of angles used was 96. As can be seen the reconstruction accurately produced the elliptical object of a uniform density.

Beam Deflection algorithm: To test the algorithm for beam deflection data, a refractive index distribution function with an analytical expression for deflection angles was chosen [Rubinstein and Greenberg (1994)]. The deflection angles representing an

axisymmetric refractive index field could also be used with Abel inversion formulae to obtain an exact analytical solution for the refractive index distribution.

Figure 3.5 shows the coordinate system for the chosen refractive index field given by

$$\delta(r) = n - n_o = Ae^{-r^2}$$

such that

$$\frac{d\delta}{dr} = -2rAe^{-r^2}$$

From the Abel formula:

$$\begin{aligned}\epsilon(y) &= 2y \int_y^\infty \frac{d\delta}{dr} \frac{dr}{[r^2 - y^2]^{\frac{1}{2}}} \\ &= -4yA \left[ \int_y^\infty \frac{r \exp(-r^2)}{\sqrt{r^2 - y^2}} dr \right]\end{aligned}$$

Let  $A=1/\pi^{0.5}$  then:

$$\epsilon(y) = -2ye^{-y^2} \quad (3.33)$$

$$\delta(r) = n - n_o = \frac{1}{\pi^{\frac{1}{2}}} e^{-r^2} \quad (3.34)$$

The beam deflection algorithm was validated using the deflection data from equation 3.33. The algorithm of equation 3.25 reconstructed the relative refractive index field, which was then compared with the analytical solution for  $\delta(r)$  given by equation 3.34.

Figure 3.15 shows the reconstructions along the y-axis using 20 and 50 views (or projections) and 250 rays. It is seen that the reconstructions are accurate everywhere

except near the center where the reconstructions over predict the relative refractive index. As noted by Faris (1988), reconstructions with the CBP algorithm in the absence of noise can be made as accurate as desired by increasing the number of samples per projection and/or by increasing the number of views. Figures 3.15 and 3.16 demonstrate the validity of this statement. The reconstructions corresponded exactly with the analytical solution when the number of views was increased from 100 to 300 as seen in Figure 3.16. At 50 views, the reconstruction is reasonably accurate everywhere except near the center. In actual experiments, discussed in the next chapter, it was decided to use 50 views. Greater number of views required more time to acquire the images as well as increased the storage and computational requirements.

The beam deflection algorithm was successfully validated and could be used to reconstruct refractive index fields from actual data using the rainbow schlieren technique. The experimental procedures for acquiring the data will be described in chapter 4 and the reconstructed fields will be compared with direct measurements.

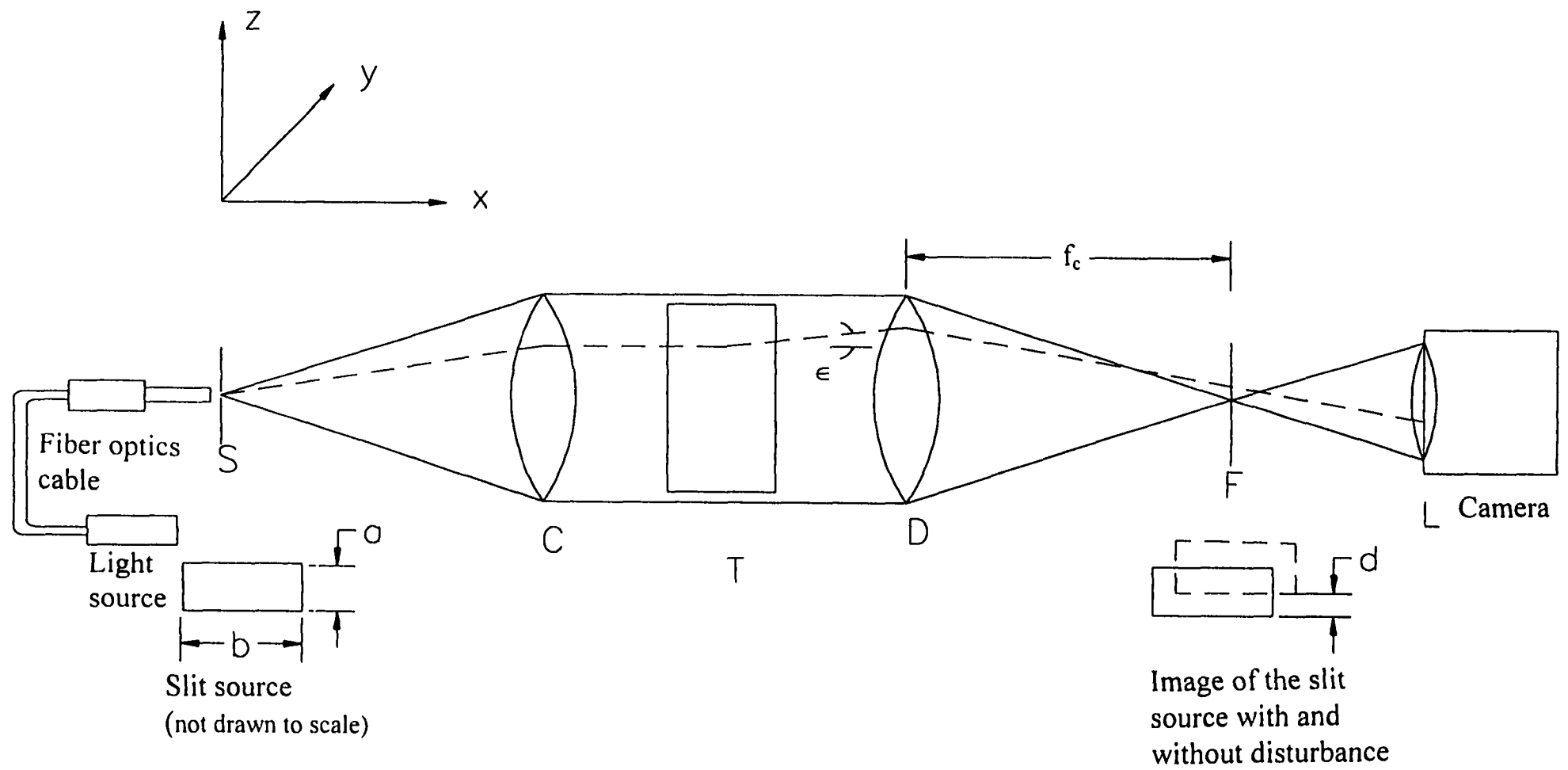


Figure 3.1 Basic schlieren setup using lenses

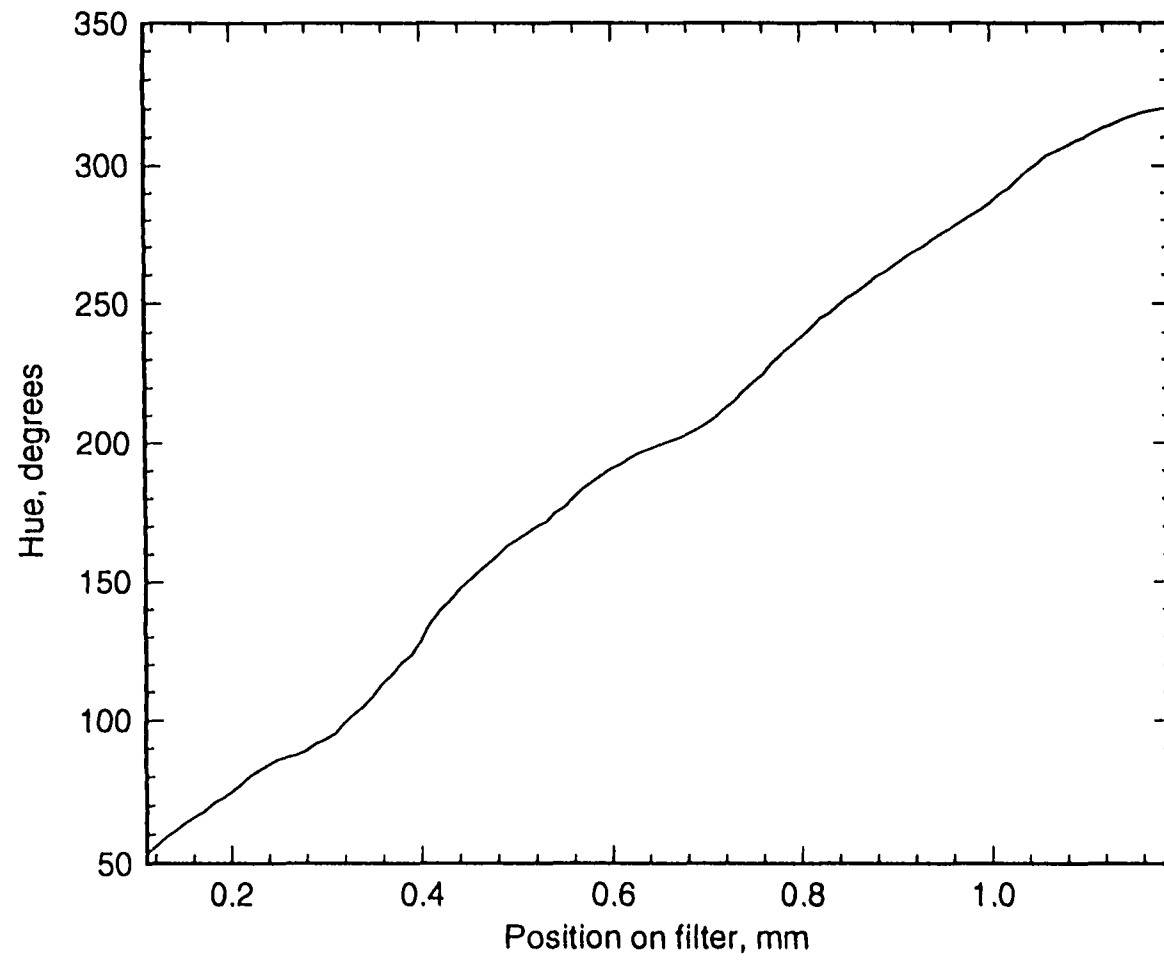


Figure 3.2 Filter calibration curve

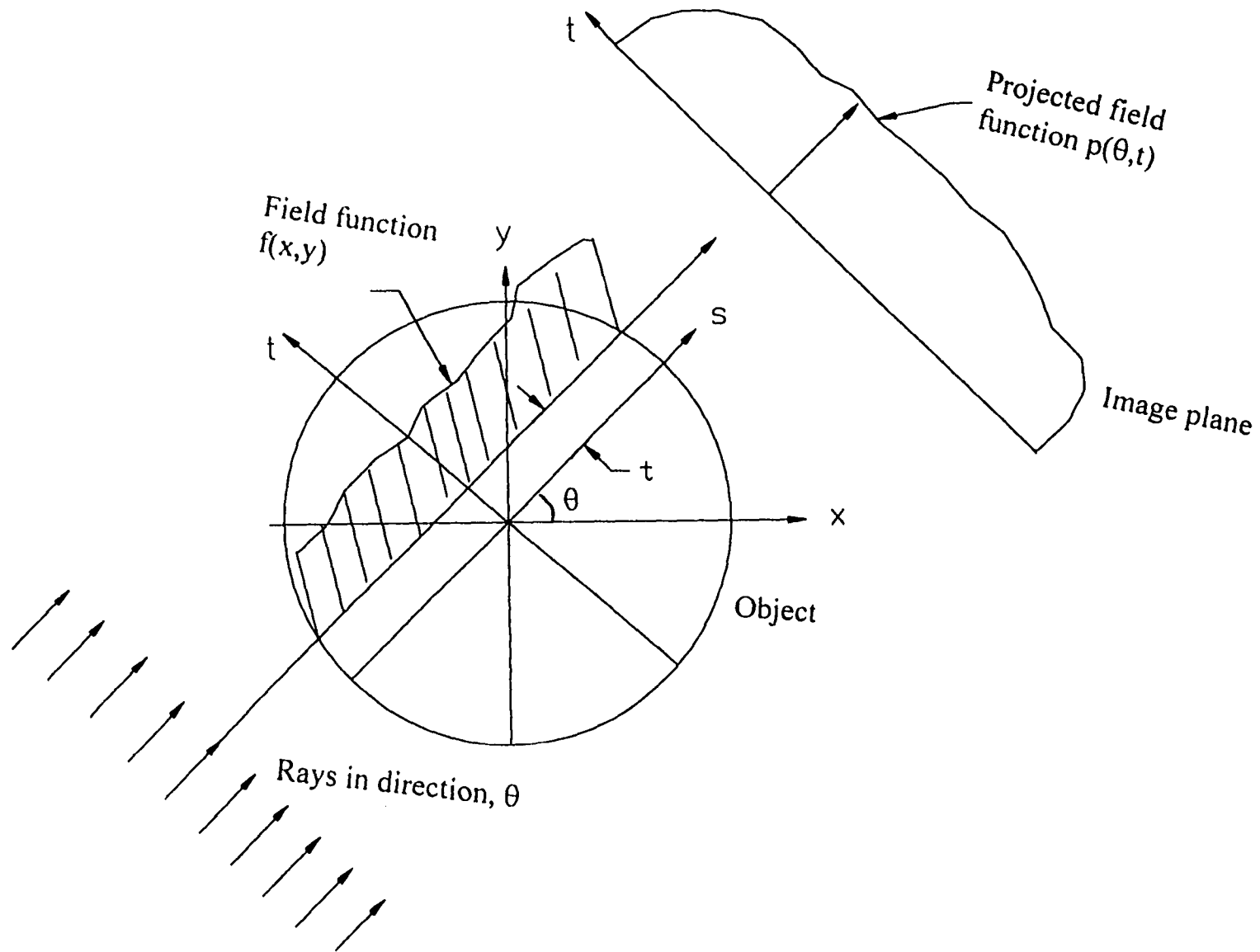


Figure 3.3 Interaction of object field and rays and the object coordinate system and projection data rotated coordinate system



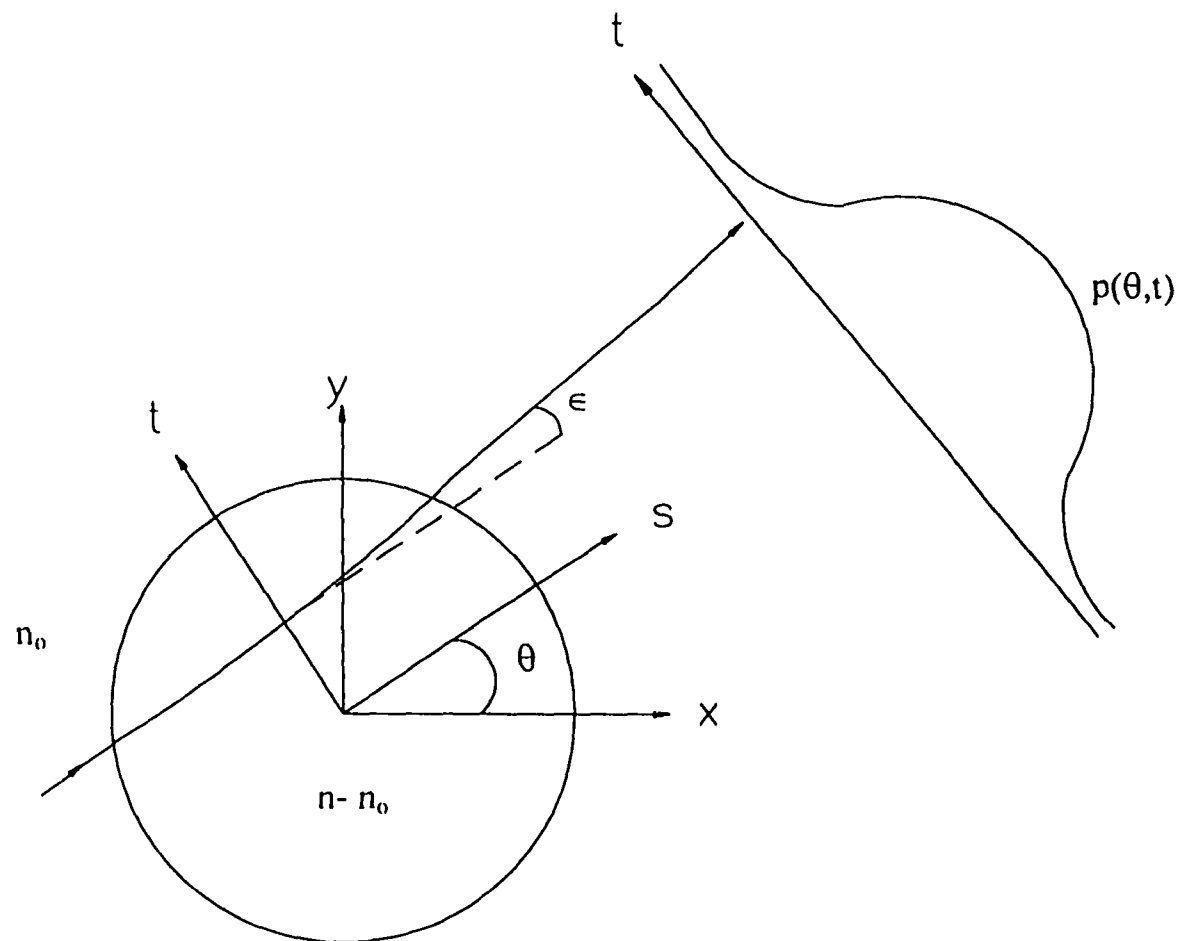


Figure 3.4 Beam deflection angle of a ray that has traversed an object field

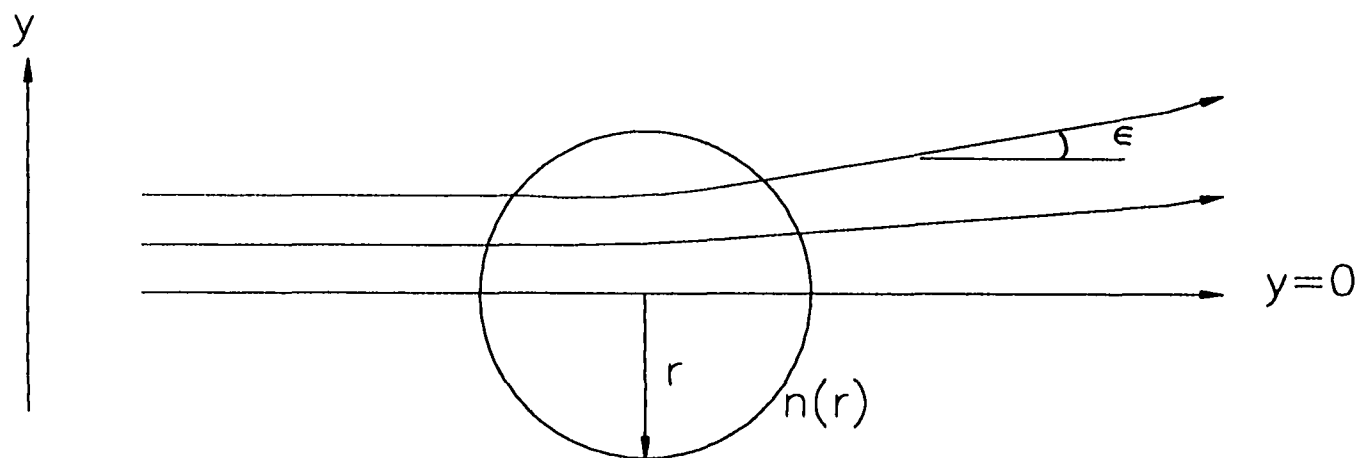


Figure 3.5 Inversion of 2-D axisymmetric refractive index field

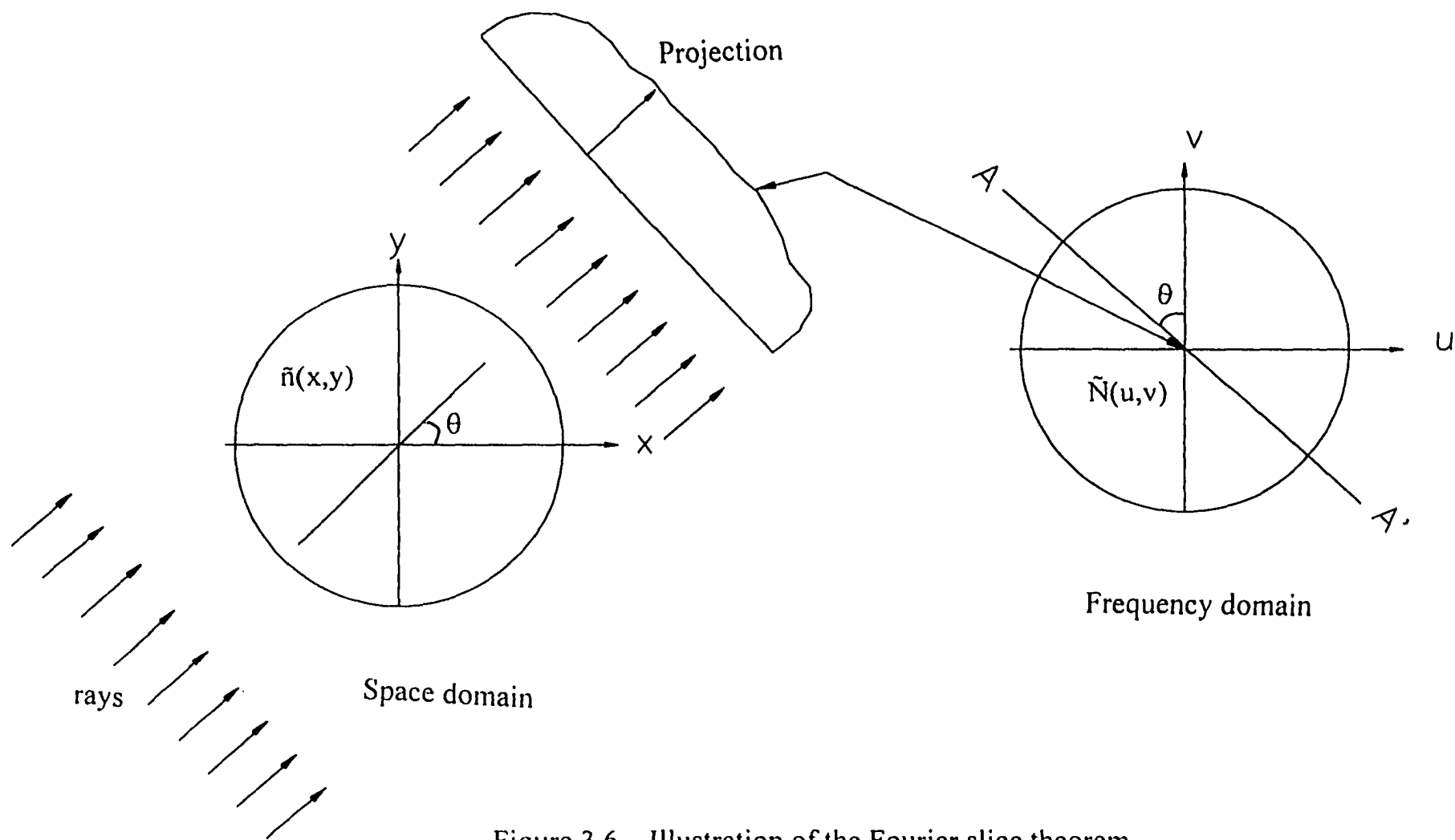


Figure 3.6 Illustration of the Fourier slice theorem

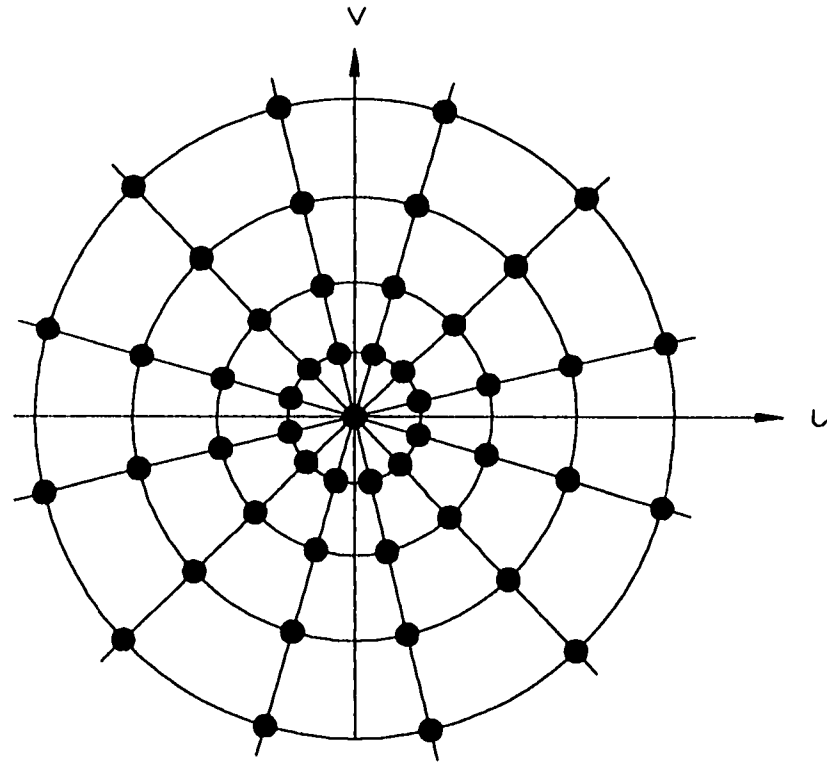


Figure 3.7 Radial frequency samples of the object function

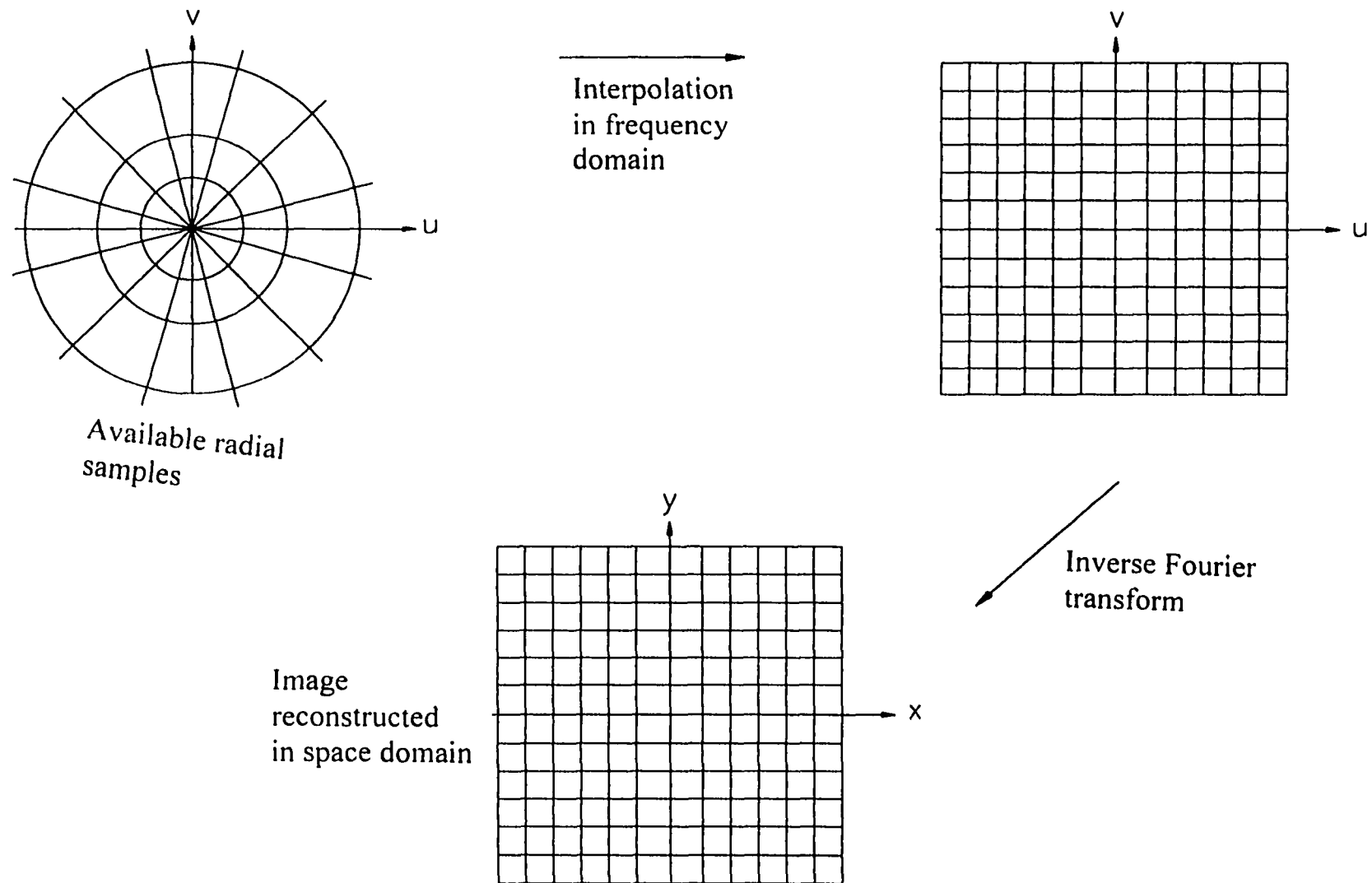


Figure 3.8 Direct Fourier reconstruction technique

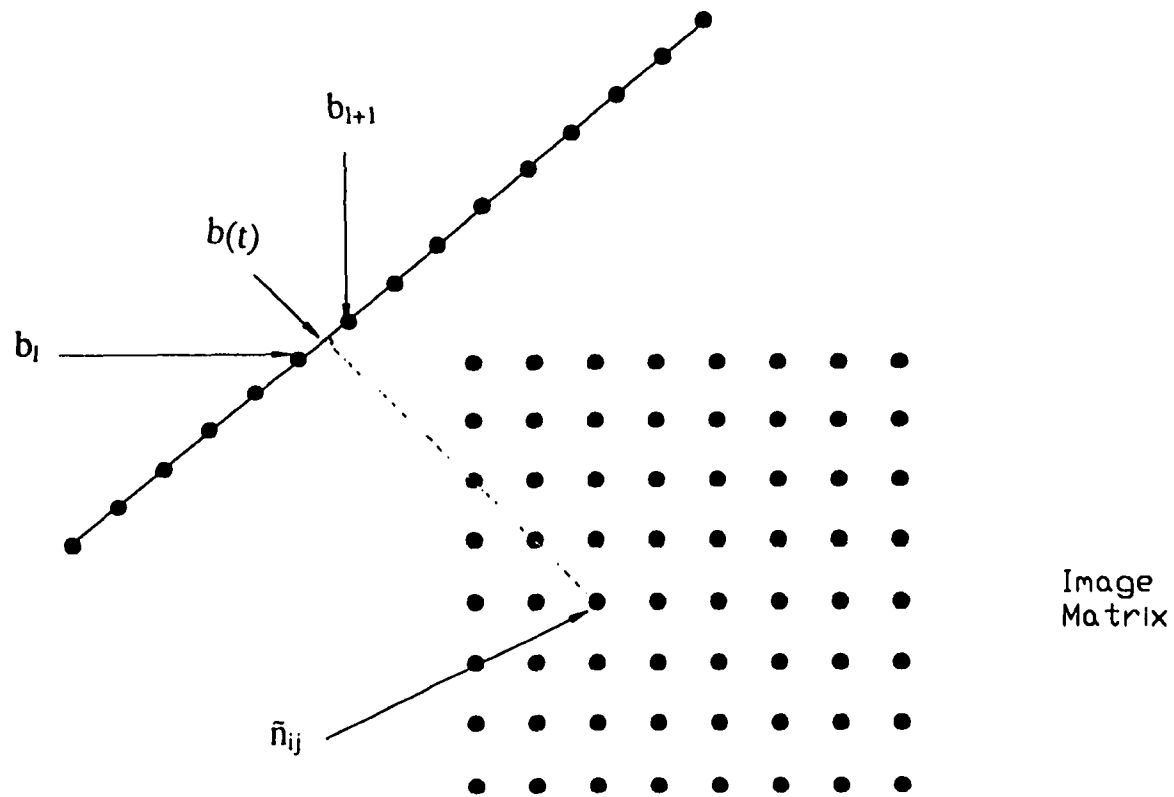


Figure 3.9 Interpolation of the backprojection data

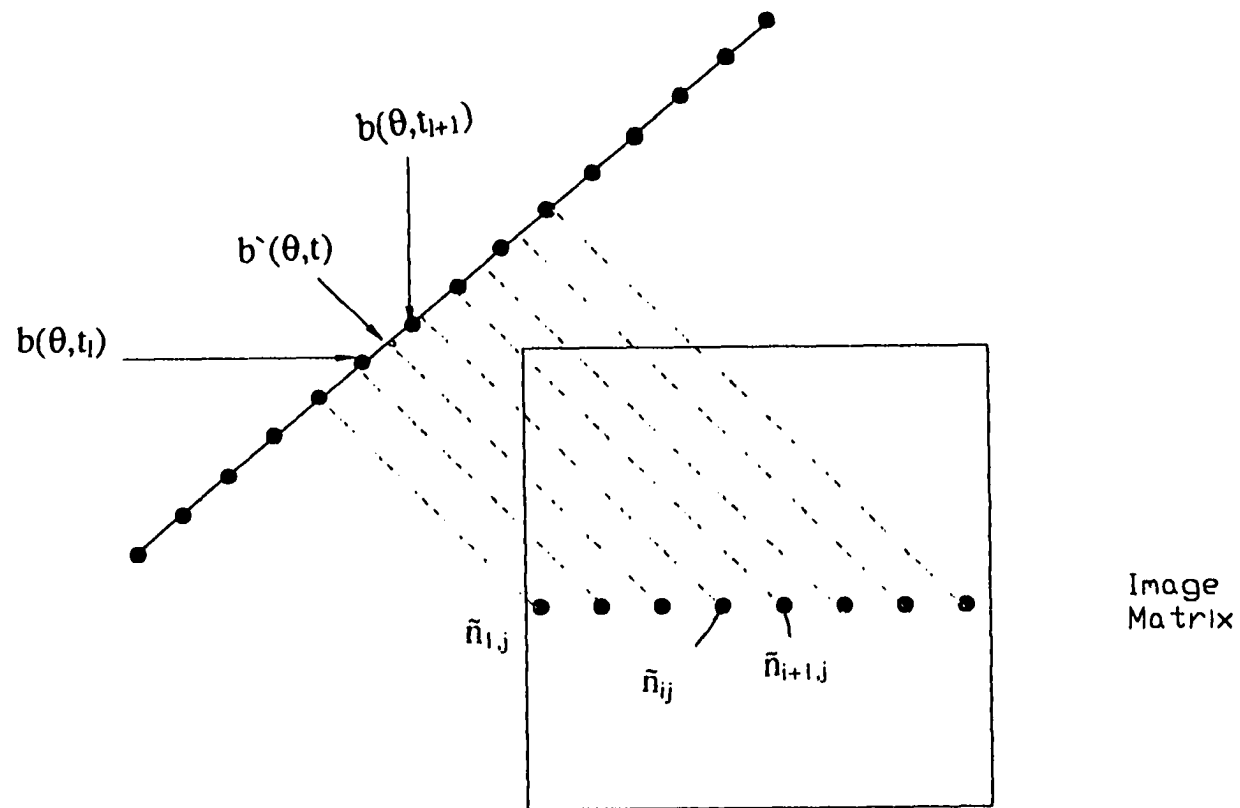
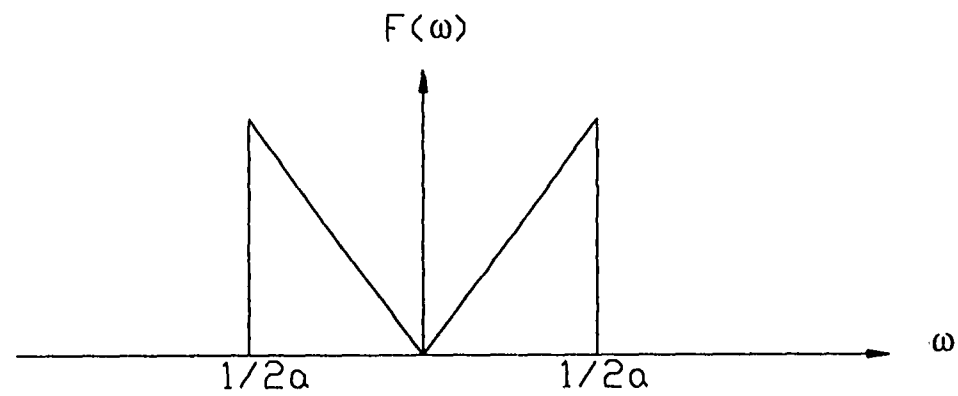
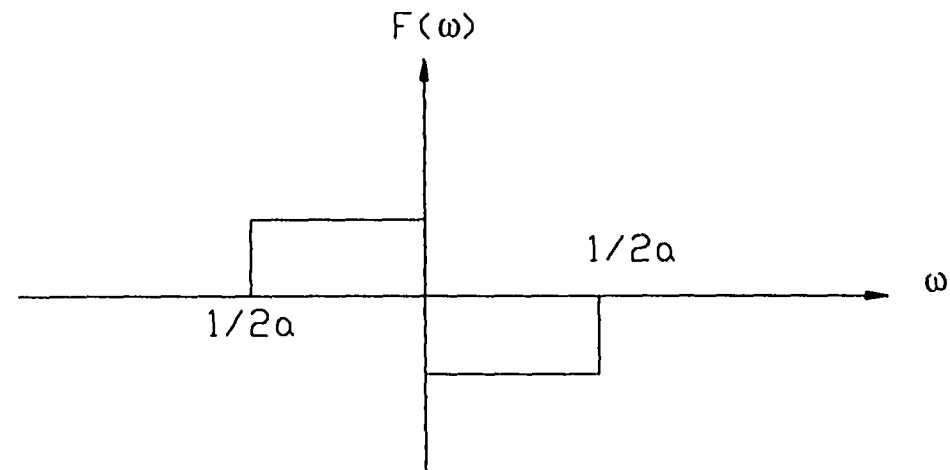


Figure 3.10 Backprojection of interpolated values of convolved projection data



Convolution function used for ordinary projection data



Convolution function used for beam deflection data  $a$  is the spacing between samples in each projection

Figure 3.11 The convolving function for ordinary deflection data and beam deflection data



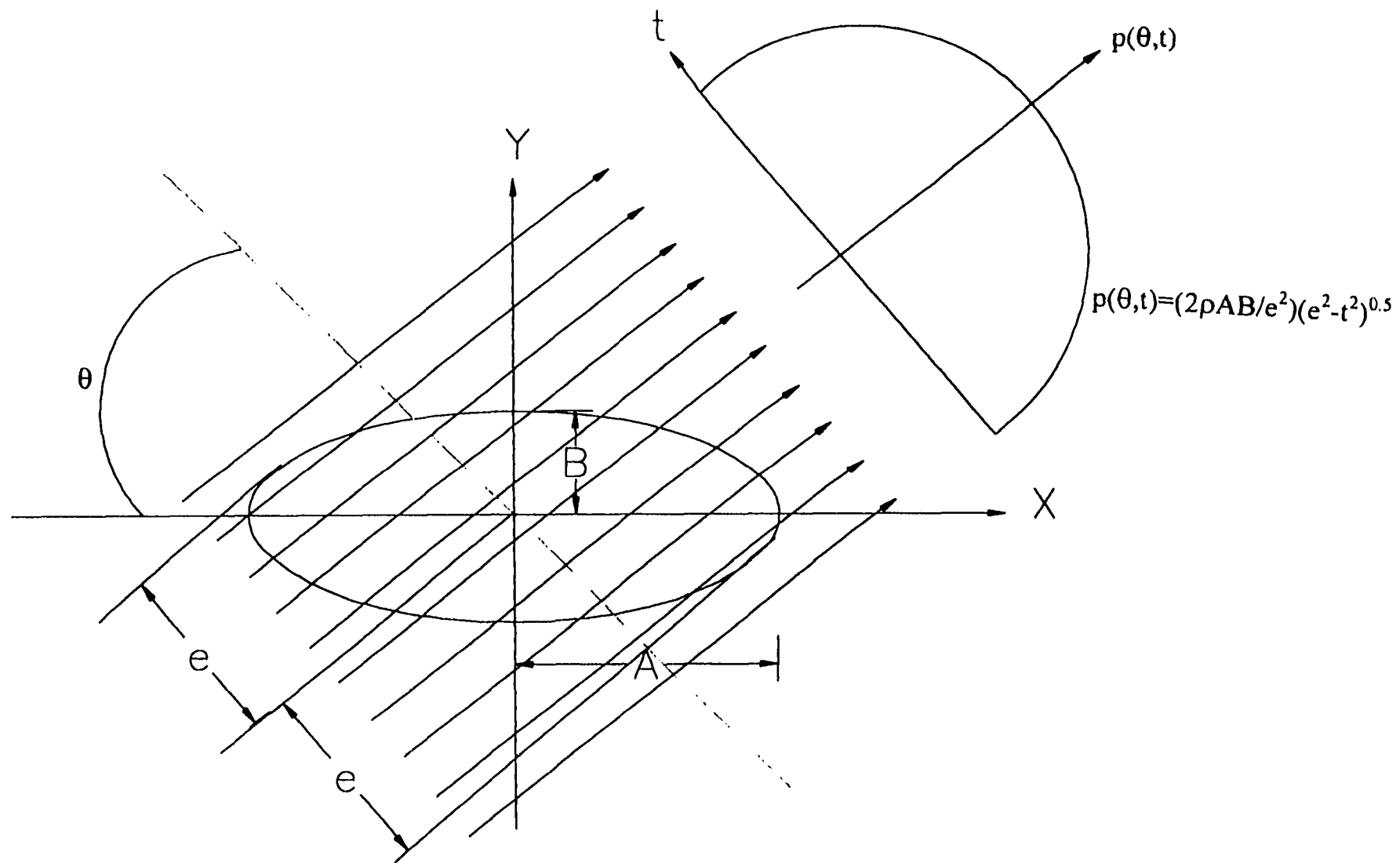


Figure 3.12 Length of rays through an elliptical object

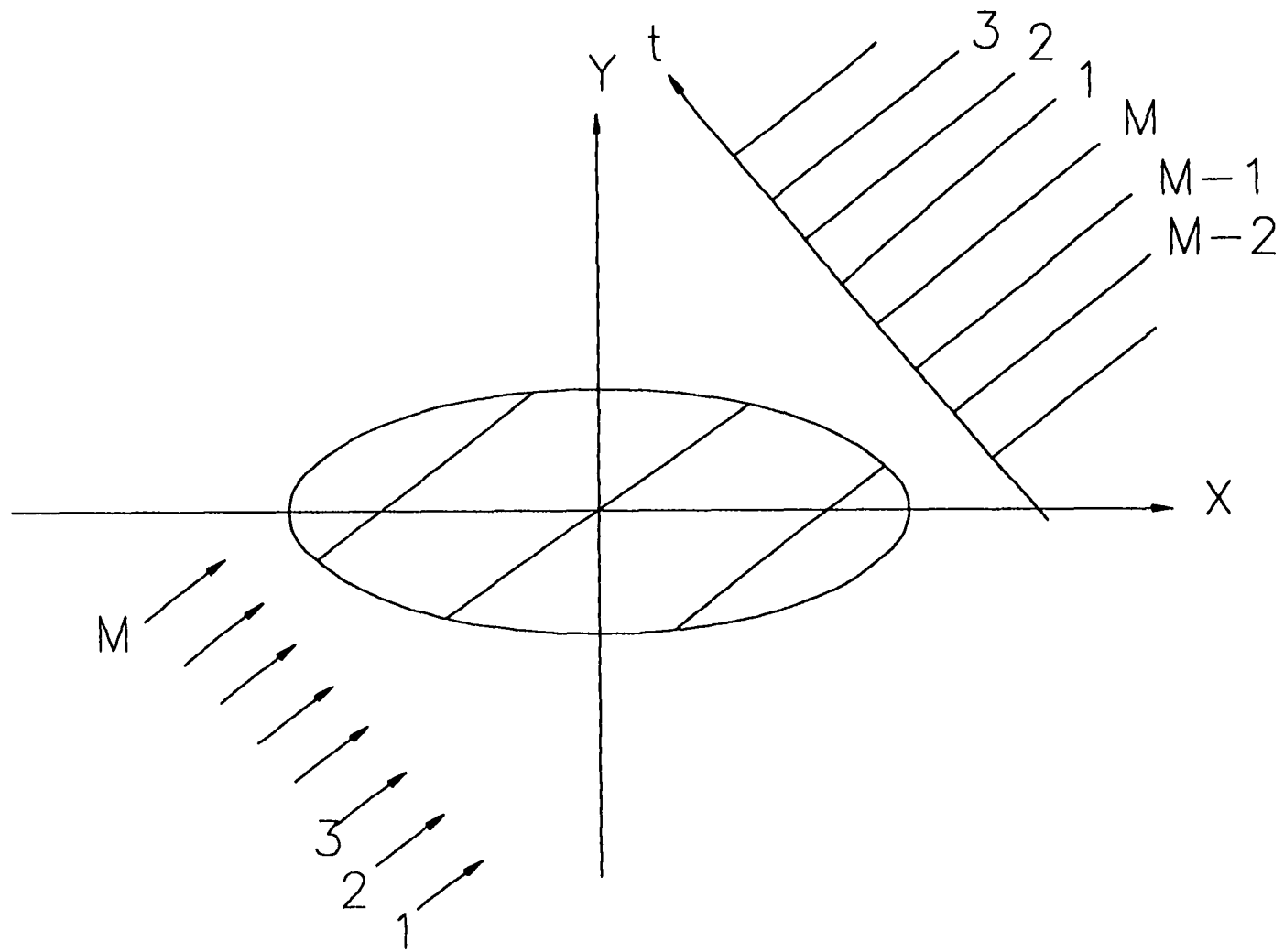


Figure 3.13 Projection data used in reconstruction algorithm

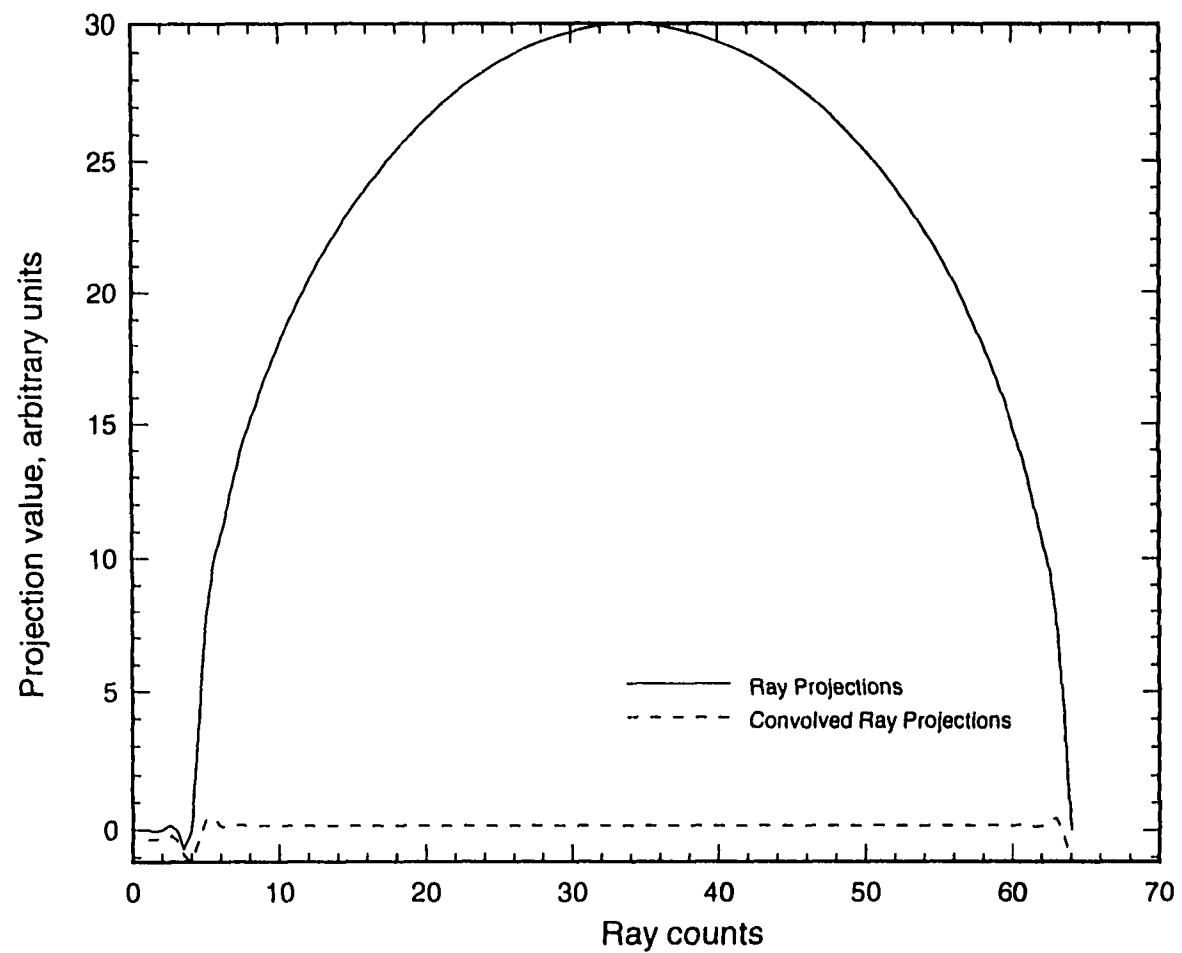


Figure 3.14a Steps in reconstruction of an elliptical object of uniform density showing the projection data and the convolved data.

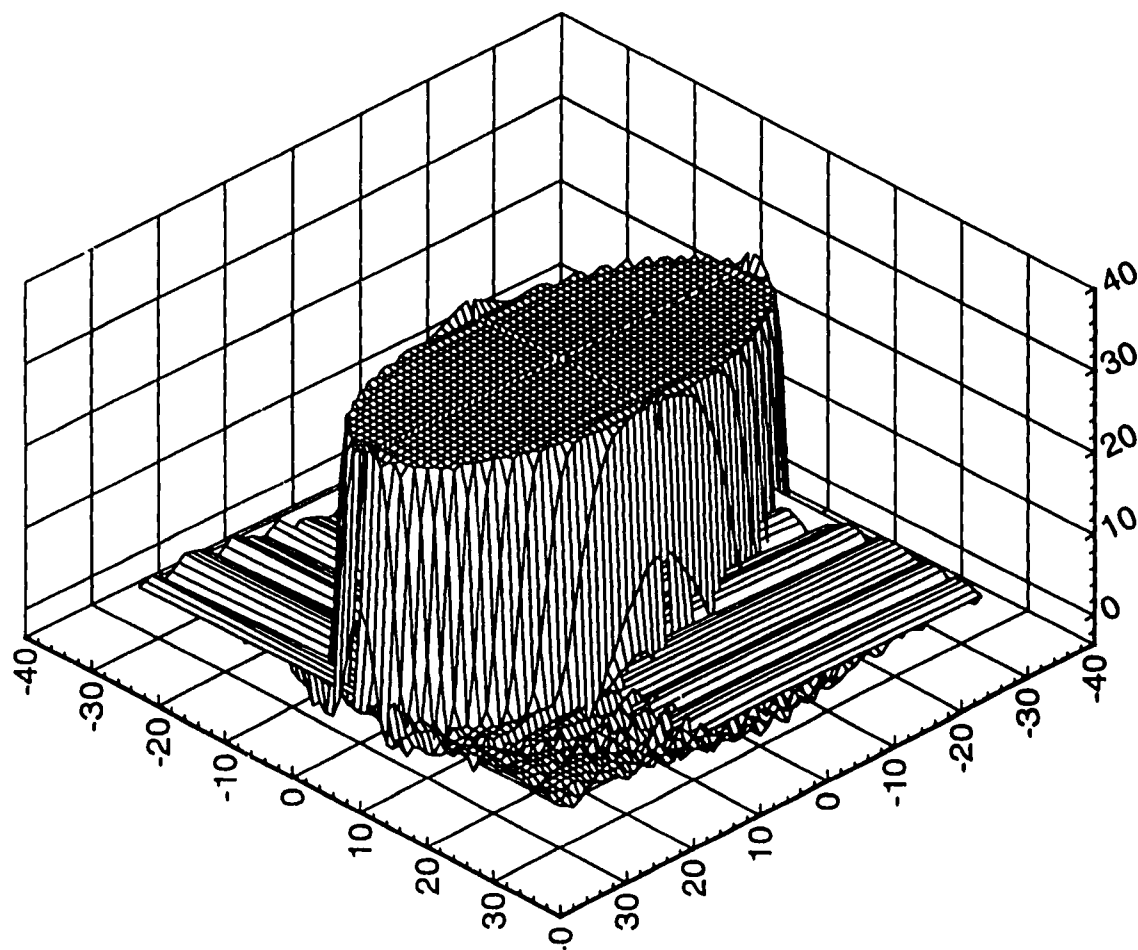


Figure 3.14b Results of reconstruction of an elliptical object of uniform density

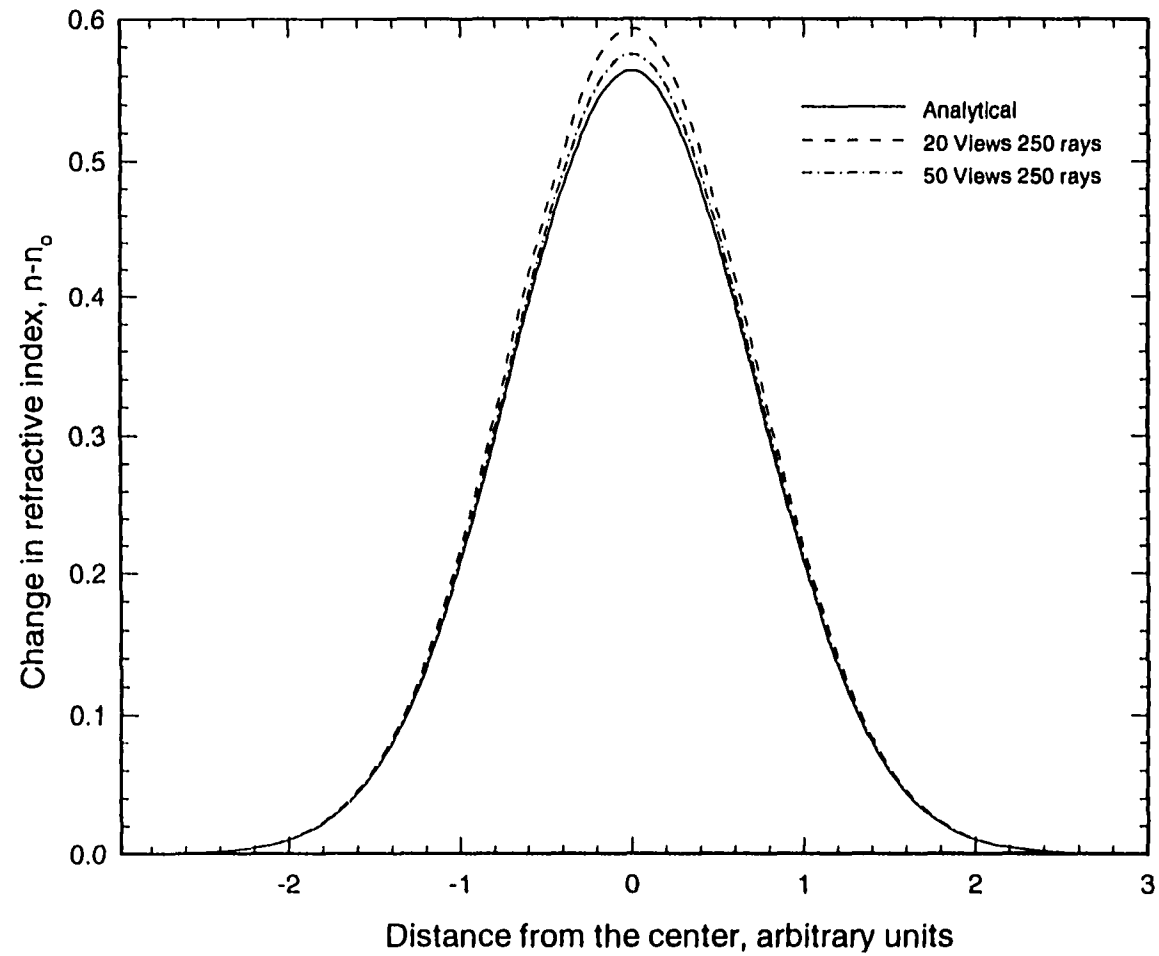


Figure 3.15 Reconstruction of refractive index field using beam deflection algorithm for 20 and 50 views, number of rays is 250

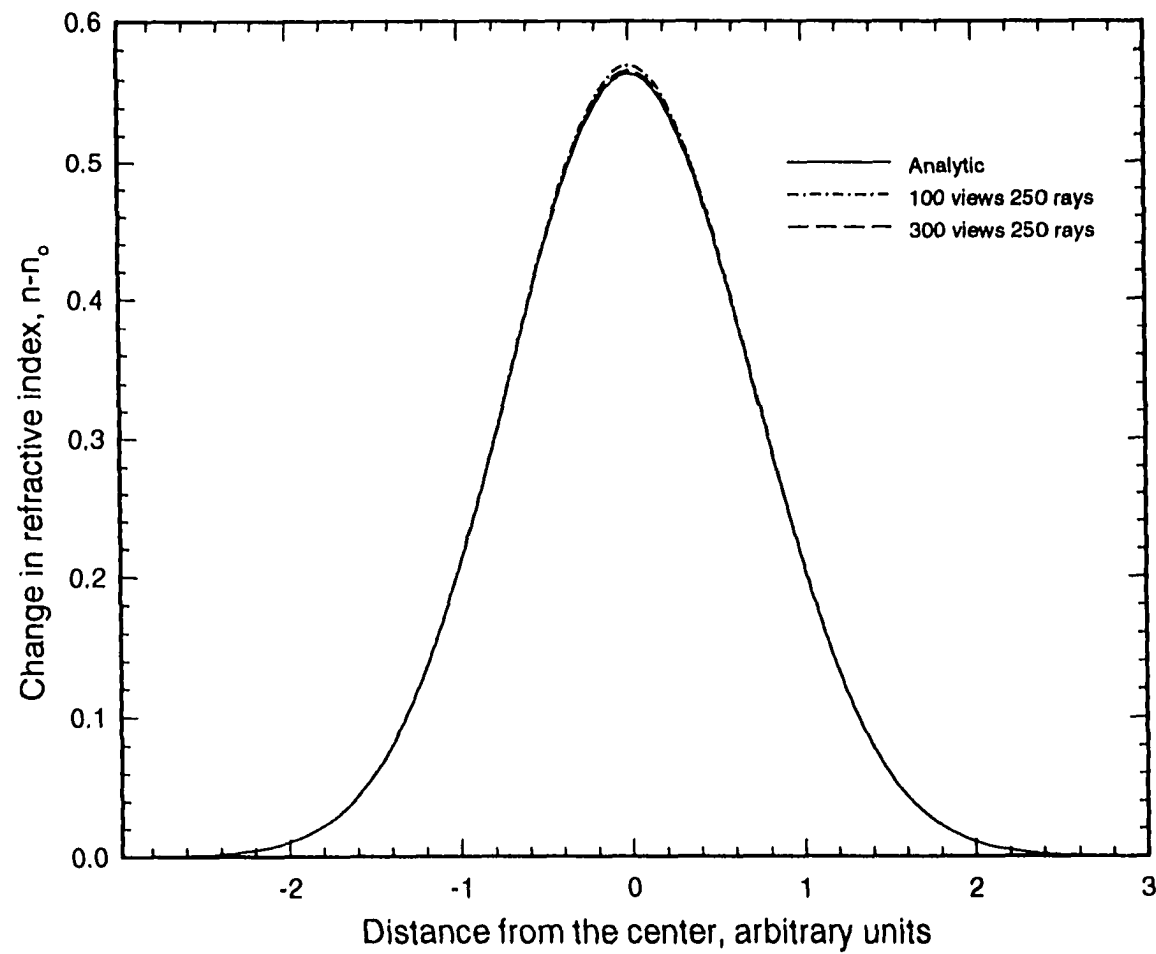


Figure 3.16 Reconstruction of refractive index field using beam deflection algorithm for 100 and 300 views and 250 rays

## **Chapter 4**

### **EXPERIMENTAL METHODS**

In this section we describe the experimental apparatus as well as the experimental procedures. Also discussed are the sources of errors in the measurements and a statistical analysis of random errors present in the measurements.

#### **4.1 Experimental Apparatus**

The overall experimental setup is shown in Figure 4.1. The basic setup consisted of the rainbow schlieren system, the heated air jet apparatus, and a data acquisition and control system. Three types of jets were investigated in this work: a vertical heated round jet, an inclined heated round jet and a vertical heated rectangular jet. The jet mounting apparatus allowed for the interchange of the jet tubes depending on the type of jet being investigated. For all jets, the experimental setup and experimental procedures remained the same. The experimental procedures consisted of calibrating the rainbow filter, measuring temperatures by a thermocouple probe, and acquiring the rainbow schlieren images.

The coordinate system used is also shown in Figure 4.1. The origin was at the intersection of the axis of rotation and the horizontal plane at the jet exit. The z-axis was oriented along the axis of rotation in the downstream direction. The x-axis was parallel to the direction of the light rays, and the y-axis was oriented normal to the direction of

the light rays. The inclined round jet was tilted with respect to the z-axis. For the rectangular jet, the major axis was along the y-axis and the minor axis was parallel to the x-axis.

The optical set up is also shown schematically in Figure 4.1. The light from a continuous xenon lamp was transmitted to the source slit by a 200 $\mu$ m fiber optic cable. The slit aperture was 50 microns in width and 2mm in height. The beam was collimated by an achromatic lens of diameter 63mm and focal length 490mm. The parallel beams then passed through the heated jet. A second lens similar to the collimating lens was used to focus the light rays. This lens produced the image of the slit source at its focal point. A rainbow filter was placed at the focal plane of the decollimating lens. A camera lens placed beyond the focal plane then produced the image of the test-section on a charge coupled device (CCD) sensor. The image was captured and digitized by a frame grabber installed in a 486 personal computer.

Figure 4.2a shows the round jet assembly. The jet apparatus consisted of an aluminum tube of inside diameter 7.1mm. The total length of the tube was 190mm. The lower half was 12mm outside diameter to fit into a pair of 90 degree screw gears mounted on a rotating table. The bottom end of the tube was a 1/8" NPT machined male thread for connecting with a 90 degree rotating swivel fitting, whose other end was connected to the exit of the air heater shown in Figure 4.2a.

The rotating mechanism consisted of a pair of 90 degree screw gears with the driver gear connected to a stepper motor via a shaft and a coupler. The assembly was supported by an open rectangular box made of 6.35 mm thick aluminum plates. A



rectangular particle board of 15.2 mm thickness was placed on the holder flush with the jet exit (and just below the incline for the inclined jet) so as to minimize convection currents from the jet tube walls and the rotating mechanism affecting the jet flow. The entire holder assembly was insulated with high temperature fiber glass insulation.

The inclined jet is shown in Figure 4.2b. The jet consisted of an aluminum tube of 12mm outside diameter and inside diameter of 6.35mm. The total length of the tube was 190mm. The top end of the tube was a machined 1/8" NPT male thread for connecting with a brass fitting inclined at 30 degrees to the vertical. The inside diameter of the inclined standard brass fitting was 5.4mm. This inclined fitting then formed the exit of the jet tube. The middle of the tube was fitted into the pair of 90 degree screw gears mounted the rotating table.

The rectangular jet apparatus is shown schematically in Figure 4.2c. The jet apparatus consisted of a brass rectangular tube of crosssection 8.7mm by 3.9mm inserted into a 12mm outside diameter tube with an inside diameter equal to the diagonal of the rectangular tube crosssection (Figure 4.2c). The total length of the tube assembly was 190mm. The lower half was 12mm diameter to fit into a pair of 90 degree screw gears mounted on the rotating table.

The air heater shown in Figure 4.3 consisted of an electrical heater, which could heat the air to a temperature of upto 1100 K depending on the supply voltage. This heater was essentially a heating element enclosed in a high temperature Pyrex glass tube of 10mm O.D. The glass tube was inserted into a stainless steel tube of 12.7mm. O.D. The heater was insulated along its length using high temperature fiber glass insulating blanket.

The heater was 133mm long and it was rated at 25 to 400 S.C.F.H air flow (0.71 to 11.31 m<sup>3</sup>/hr.) with a power rating of 465 watts @ 120 volts. The voltage could be varied by a power control module (variac) connected to a standard 120 V electrical outlet. Compressed air passing through a mass flow meter and a needle valve was fed to one end of the heater. With an appropriate compression fitting, the other end of the heater was connected to the rotating swivel at the bottom of the jet tube in the tube holder.

A three-dimensional translating mechanism as shown in Figure 4.3 was used to obtain thermocouple measurements across the heated air jet. The thermocouple was constructed of thin 0.013mm diameter wire of type-K. The bead diameter was about 0.3mm. Thermocouple measurements were taken at three heights above the jet exit at  $z=5\text{mm}$ ,  $10\text{mm}$  and  $15\text{mm}$  planes. The  $z$ -axis of the translating stage was not automated. At each height, temperatures were taken along the  $x$ -axis (parallel to the light rays) and along the  $y$ -axis (normal to the light rays) at equal intervals of about 1 mm using the stepper motors connected to the translating stage. The stepper motors were computer controlled and the thermocouple measurements were recorded by the same computer using a data acquisition card. The data were acquired at a rate of 10 samples per second for a period of 10 seconds, thereby providing 100 measurements at each point. Details of the data acquisition card and software are described elsewhere [Butuk and Gollahalli (1996)]. The temperature was measured at approximately 100 points along each axis.

## 4.2 Experimental Procedures

Figure 4.4 shows a schematic of the apparatus used to calibrate the filter before using it to study a particular test field. The calibration was done without disturbances in test field. The calibration procedure consisted of mounting the filter on a micrometer translating stage operated manually. The procedure involved translating the filter across the focal point over the width of the rainbow filter. The translation was done in steps of 0.01 mm and at each step an image of the test section with no disturbances was captured. This was done after carefully aligning the optical components. In all, about 120 steps were taken for a total of 120 images. These images were then processed and the average hue over a rectangular portion of the image was computed for each image. The standard deviation of the mean hue was also obtained for each image. A standard deviation of less than 0.06 radians was desired for a good quality filter. This indicated a correct sizing of the slit in relation to the filter width. The hue of each image plotted against translation across the filter produced the calibration curve shown in Figure 3.2. This filter is the 1st generation filter following the terminology introduced by Greenberg et al.(1995).

The 1st generation filter resulted from an optimization procedure that was performed to manufacture the filter. The filter was manufactured by computer generating the desired rainbow spectrum over the desired width. This width depended on the sensitivity required of the schlieren system. The hue variation from 0 to 360 degrees was linearly distributed over the width of the filter. The computer output was printed by a 35mm slide recorder. The 35mm slide was then sent for development and printing in a photographic shop. Once developed, the hue distribution on the printed 35mm slide

(known as zeroth generation filter) will not be linear as desired. This is because of the nonlinearities introduced by the recorder, the film developing process and the schlieren system. To linearize the hue distribution, a correction procedure was undertaken. In this procedure, the relationship between hue and filter location of this zeroth generation filter was used to produce a 1st generative filter that corrected for non-linearities present in the zeroth generation filter. Essentially the difference between the computer generated linear curve and the measured curve of the developed filter was determined. This difference was then used to add or subtract to the hue distribution used by computer to produce the 1st generation filter. This nonlinear hue distribution was sent to the slide recorder and the printed film subsequently developed. This procedure could be repeated to create the next generation filter until the desired degree of linearity was achieved. In this work it was only necessary to produce a 1st generation filter whose calibration curve is shown in Figure 3.2.

The experimental procedure involved setting the flow rate at a fixed value of  $0.004 \text{ m}^3/\text{min.}$  for the round jet (  $0.00206 \text{ m}^3/\text{min.}$  for the inclined jet and  $0.004 \text{ m}^3/\text{min.}$  for the rectangular jet) to provide Reynolds numbers of 570, 380 and 500 respectively at the jet exit. These were based on diameter for the round and inclined jet and based on width for the rectangular jet. The experimental conditions are shown in Table 4.1. The experiment was started by turning on the heater and fixing the voltage at a predetermined value to give a jet exit temperature of about 450K. The jet attained steady state conditions after about 1.5 hr. Even after this time the fluctuations in the line voltage caused temperature variations of up to 10K in the jet exit temperature.

After attaining steady state, the experiment was begun by turning off the air flow rate and by capturing the image of the undisturbed test section. This image was used as a reference zero deflection image or the background image. The average hue for this image was used as the reference hue. After this image was captured, the flow was turned back on and thermocouple point measurements were taken at the  $z = 5\text{mm}$  axial plane. After probe measurements along the  $x$  and  $y$  axes at  $z = 5\text{mm}$  and along the  $y$  axis at the  $z = 10\text{mm}$  plane, the experiment was half completed. At this time the schlieren images were acquired and stored.

For the round jet, because of axisymmetry, images were acquired only at one view angle. This was done by visually capturing the most symmetric image displayed on the computer screen. For the inclined jet and the rectangular jet, 50 views of the heated jet were acquired by rotating the jet using a stepper motor in equal angular increments over a 360 degree angle. A Windows-based image processing program was used to acquire and store the images. The program had the basic processing functions for capturing, saving and loading the images. Each schlieren image was recorded and stored in digital form for later analysis.

After acquiring the schlieren images, point thermocouple measurements were completed for the  $x$  axis at the  $z = 10\text{mm}$  plane and for  $x$  and  $y$  axis at the  $z = 15\text{mm}$  plane. The experiment was then shut down and the images analyzed using the convolution backprojection algorithm. The details of this algorithm have been described in chapter 3. For accurate reconstructions in the near region of the rectangular jet, it was necessary to

increase the number of views. Linear interpolation was used to increase the views from 50 to 99 over 360 degree angle of rotation.

#### **4.3 Sources of Errors and Error Analysis**

There are four main sources of error in the present measurements with the schlieren technique

- (i) Random errors due to flow disturbances
- (ii) Errors due to optical imperfections, misalignment of the optical setup and non-uniformities in the background hue.
- (iii) Experimental errors due to vibrations, imperfect jet rotation and orientation
- (iv) Errors introduced by the reconstruction algorithm.

The random errors because of room air disturbances were found to be the major source of error. Some causes of these disturbances include natural room air currents caused by the movement of occupants and variations in room temperature, natural convection currents caused by the mounting system surfaces, temperature fluctuations because of line voltage variations and room air disturbances from unknown sources. These disturbances caused the jet to sway about the axis of rotation. Therefore care was exercised in capturing the images by visualizing the most steady jet on the computer screen. A statistical analysis was performed to quantify this random error. The procedure of analysis is explained below.

The errors due to optical imperfections such as chromatic aberration of lenses and non-linearities in the manufacture of lenses affected the data. These errors affect the accuracy of the instrument and are fixed for a particular schlieren optical setup.

Another source of errors is because of the misalignments. Since the jet tubes used were not manufactured to high precision there was misalignment in their vertical orientation. The rotating system was also not of high precision and caused some rotation misalignment. These errors created difficulty in exactly matching the location of the thermocouple measurements with the schlieren reconstructed temperatures in some cases. Even though care was exercised in measurements, the errors due to misalignments caused spatial resolutions to be off by  $\pm 5$  pixels in some cases, which is equivalent to about  $\pm 0.5\text{mm}$ .

The reconstruction algorithm could also introduce errors. Using convolution backprojection (CFB), Hughey and Santavicca (1982) identified four possible causes of these errors:

- (i) The presence of noise in the data or the magnitude of the signal to noise ratio (SNR)
- (ii) aliasing errors caused by undersampling both in angle and space.
- (iii) Gibb's phenomena, which occur when there is a discontinuity in the refractive index field to be reconstructed.
- (iv) improper choice of the convolution or filtering function

The presence of noise in the projection data can have a profound influence on the reconstruction accuracy. Hughey and Santavicca (1982) have demonstrated that even a 2% random error in the data can cause reconstruction inaccuracies of as much as 10% in

the center region. By performing a frequency spectrum of the projection data they suggested a method of identifying noise data and separating it from the signal data. When this is done, the inaccuracies in the center region of the reconstruction tend to be smoothened.

Aliasing errors are caused by undersampling the projection data per view. When this occurs, high frequency components appear at low frequencies; this causes under prediction of the jet peak. Dash (1992) has pointed out that, if the spacing of the projections is decreased (by oversampling), the real difference between adjacent projections becomes smaller. When this difference becomes comparable to the noise in the data, the CBP algorithm becomes inaccurate. It is hence recommended that noisy data be smoothened. Steightz (1974) gives the formula required for adequate sampling of  $M$  points in a given projection it is:

$$M = R\omega_{max}/\pi$$

where  $R$  is the outer radius of the flow boundary and  $\omega_{max}$  is the maximum frequency of the experimental projection data. According to the sampling theorem, a function can be uniquely recovered from its samples if it is sampled at a rate greater than twice the highest frequency component of the function. This Nyquist frequency is given by  $1/2a$ , where  $a$  is the sampling spacing in the projection. If the sampling criteria are not met, the reconstruction function will contain contributions from the under-sampled high frequency components which appear as low frequency contributions in the transform domain.



The filter that is used in the reconstruction should filter out high frequency information in the experimental data. Kwoh (1977) has indicated that the ideal filter has a bandwidth which includes all the essential information for reconstruction, but filters out high frequency noise.

The other source of error is the Gibbs phenomenon which occurs when there is a discontinuity in the refractive index of the flow field. When this happens, an oscillating overshoot occurs at the discontinuity. This is the cause of error in the convolution backprojection algorithm. This phenomenon is likely to occur at jet boundaries of the reconstruction region.

#### Experimental errors and statistical analysis

Holman (1994) discusses two types of experimental errors, (i) systematic or fixed errors. These are the errors that are of similar magnitude in all repeated measurements, and (ii) random errors, which are caused by human operators, environmental conditions, fluctuations in the voltage and other random sources of errors.

The random errors were greater than the fixed errors in this study. Therefore, we shall discuss the relevant analysis procedure for these errors. Uncertainty in these errors are best reported in terms of statistics based on the 95% confidence level, and the assumption that the measurements follow the Gaussian type distributions clustered about the median with a common median and standard deviation independent of sample size. Statistically, a value of three times the standard deviation on both sides of the mean value (i.e.,  $\pm 3\sigma$ ) covers most of the area under the Gaussian normal distribution curve. The 95% confidence interval is covered by  $\pm 2\sigma$  of the mean value. This  $\pm 2\sigma$  confidence

level is taken as the basis of student's t-test. The use of the normal distribution curve requires many samples from a large population. Experimentally the number of samples that can be acquired is limited. Therefore, the student's t-test modifies the spread about the mean by a factor depending on the number of samples and the required confidence level. With this modification fewer samples of varying data can be acquired and analyzed. When an unbiased data of n samples is acquired, the standard deviation is calculated as

$$\sigma = \left[ \frac{\sum_{i=1}^n (x_i - x_m)^2}{n - 1} \right]^{\frac{1}{2}}$$

where  $x_i$  is the data and  $x_m$  is the mean. For an uncertainty level of c, the Students 't' distribution gives:

$$c = \pm \frac{t\sigma}{\sqrt{n}}$$

t is found from students t-tables for different degrees of freedom and levels of confidence. For example for ten samples, at 95% confidence level, the Students t= 2.228 [Holman (1994)]. Sample calculations of error using this procedure are given in Appendix A.1.

**Table 4.1**

**Experimental Conditions:**

Jet	Round	Inclined	Rectangular
Flow rate (cold), m <sup>3</sup> /min	0.004	0.00206	0.004
Mass flow rate, kg/s	7.847X10 <sup>-5</sup>	4.041X10 <sup>-5</sup>	7.847X10 <sup>-5</sup>
Reynolds number	570	380	500
Exit temperature, K	450	450	450
Diameter or major dimensions, mm	7.1	5.4	8.7X3.9

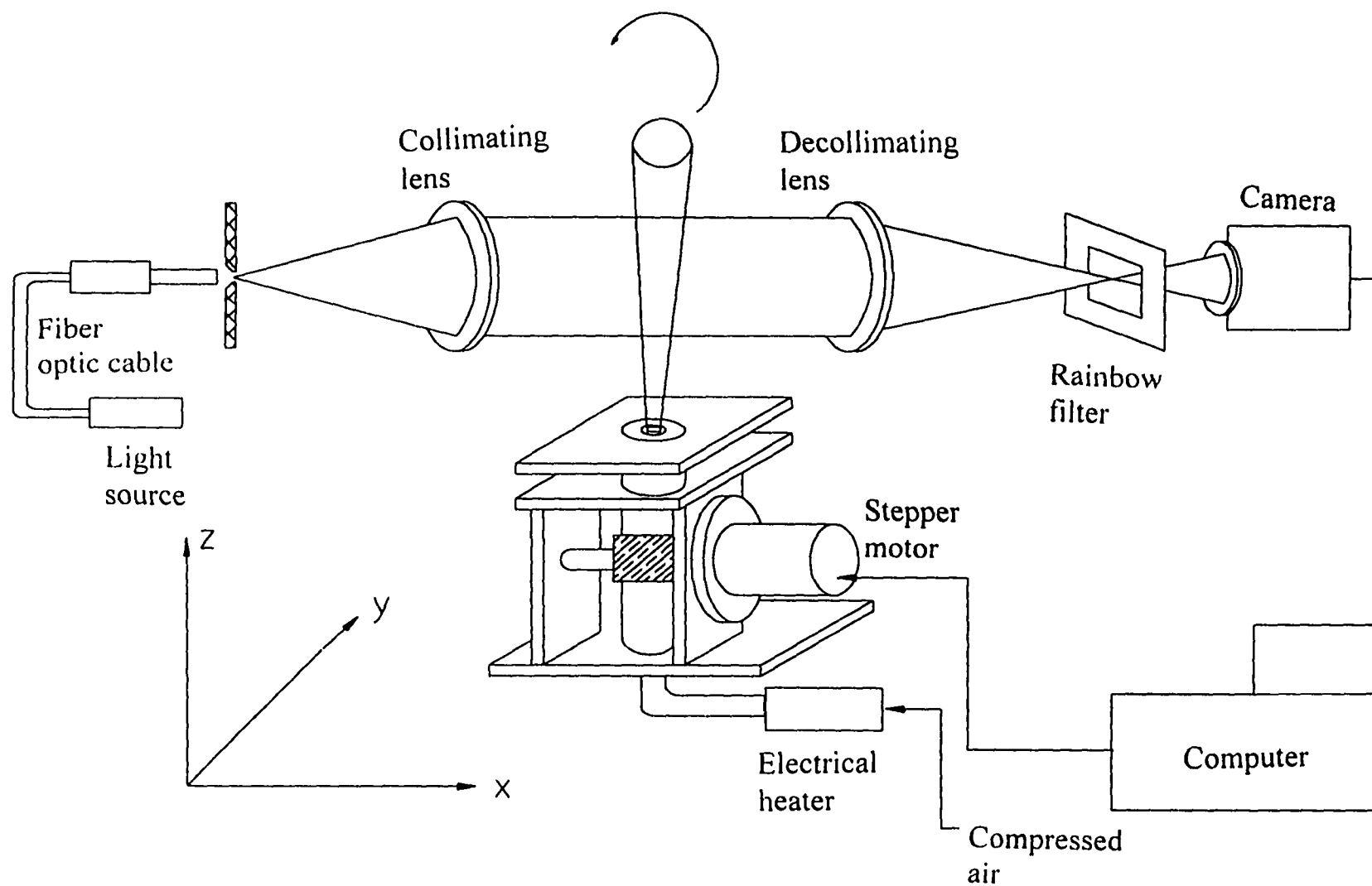


Figure 4.1 Overall experimental setup showing the schlieren optics and jet apparatus

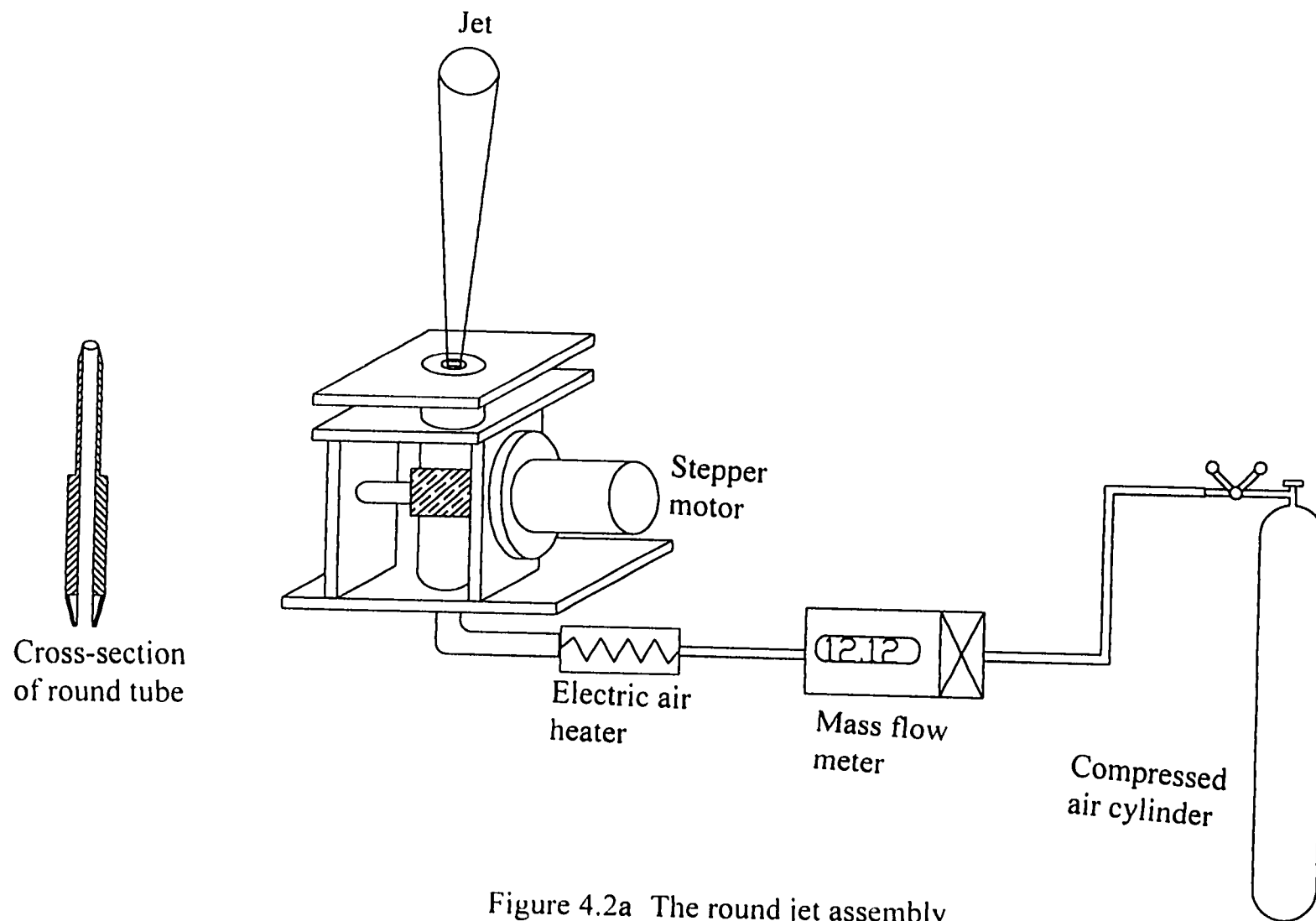


Figure 4.2a The round jet assembly

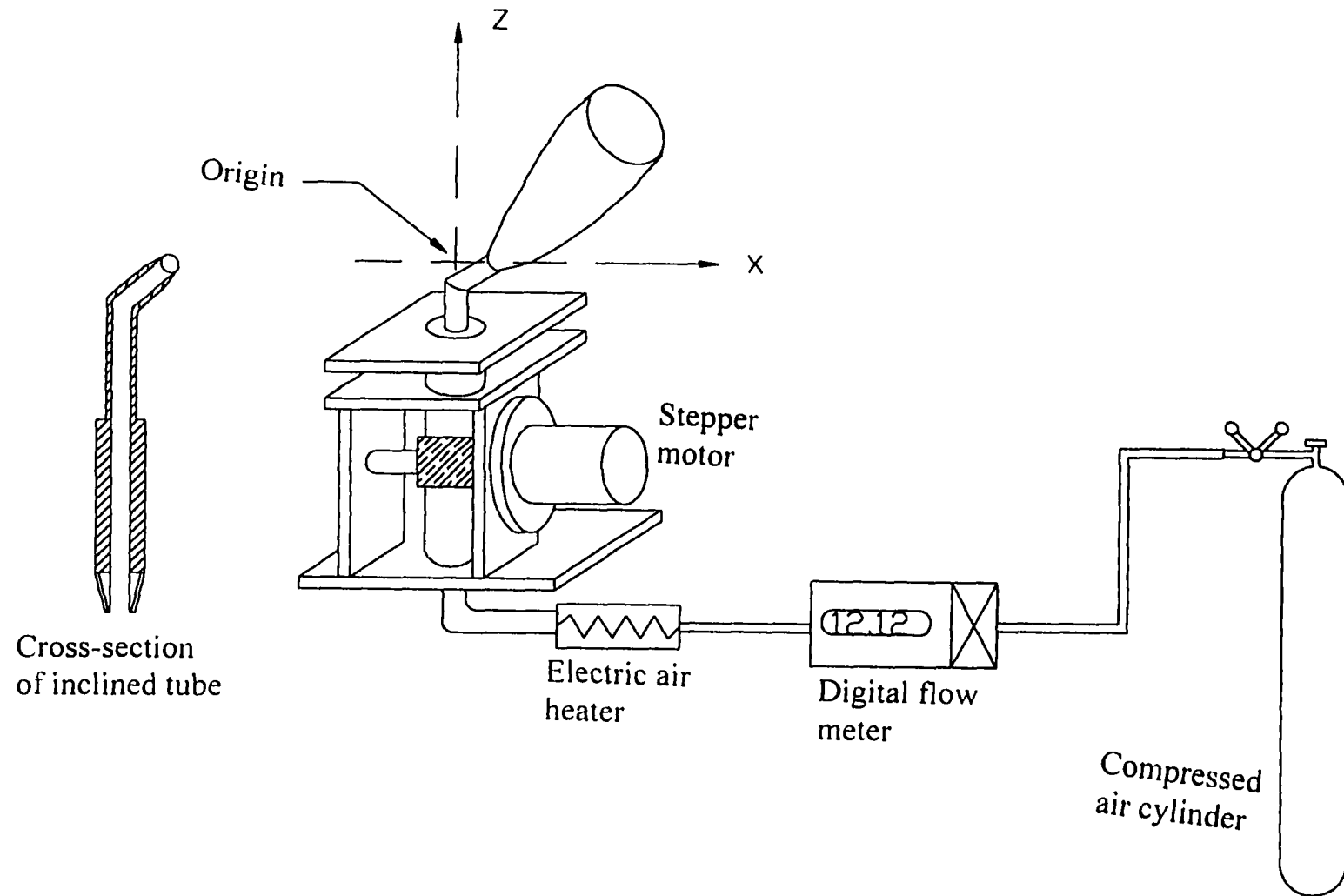


Figure 4.2b The inclined jet assembly

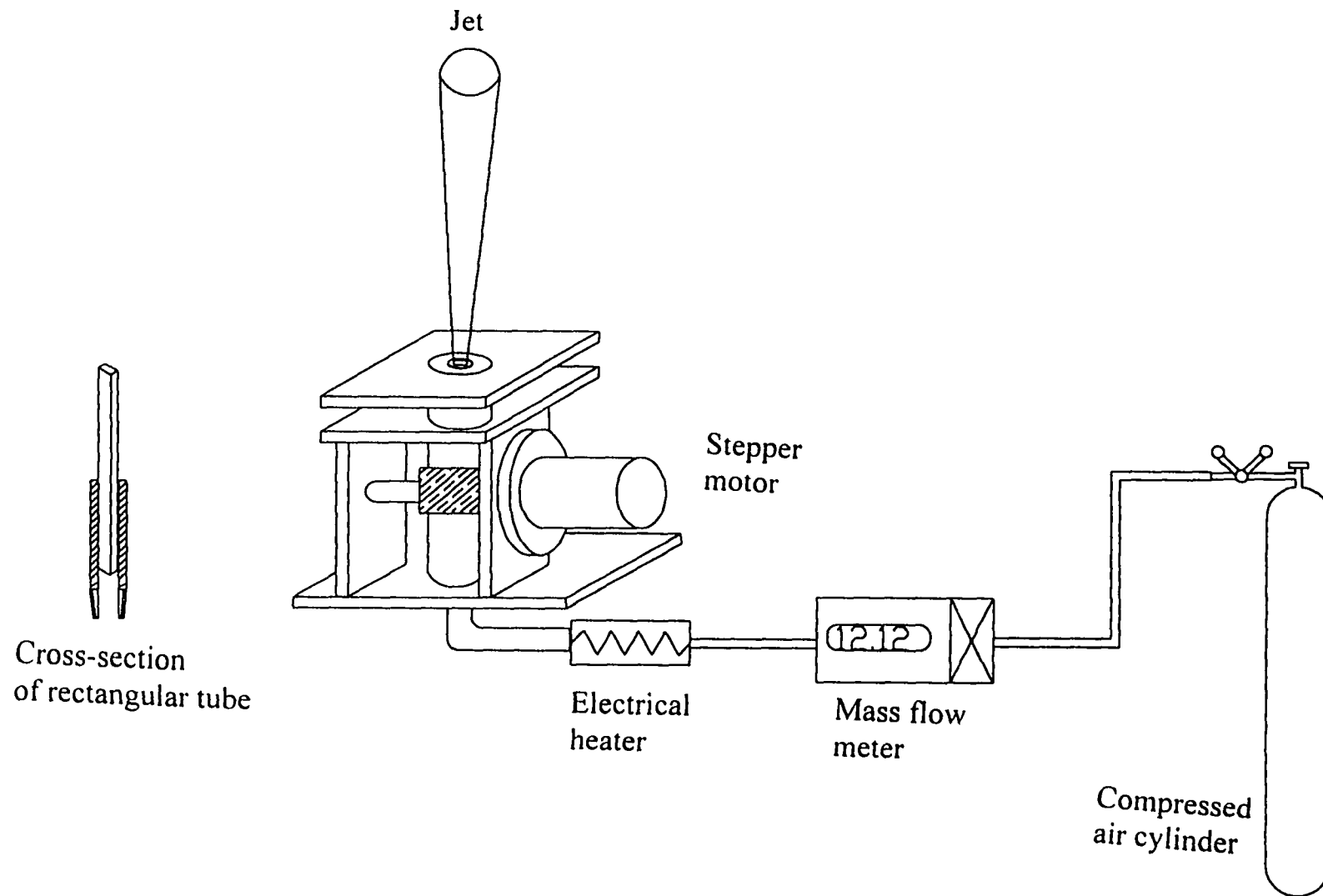


Figure 4.2c Rectangular jet assembly

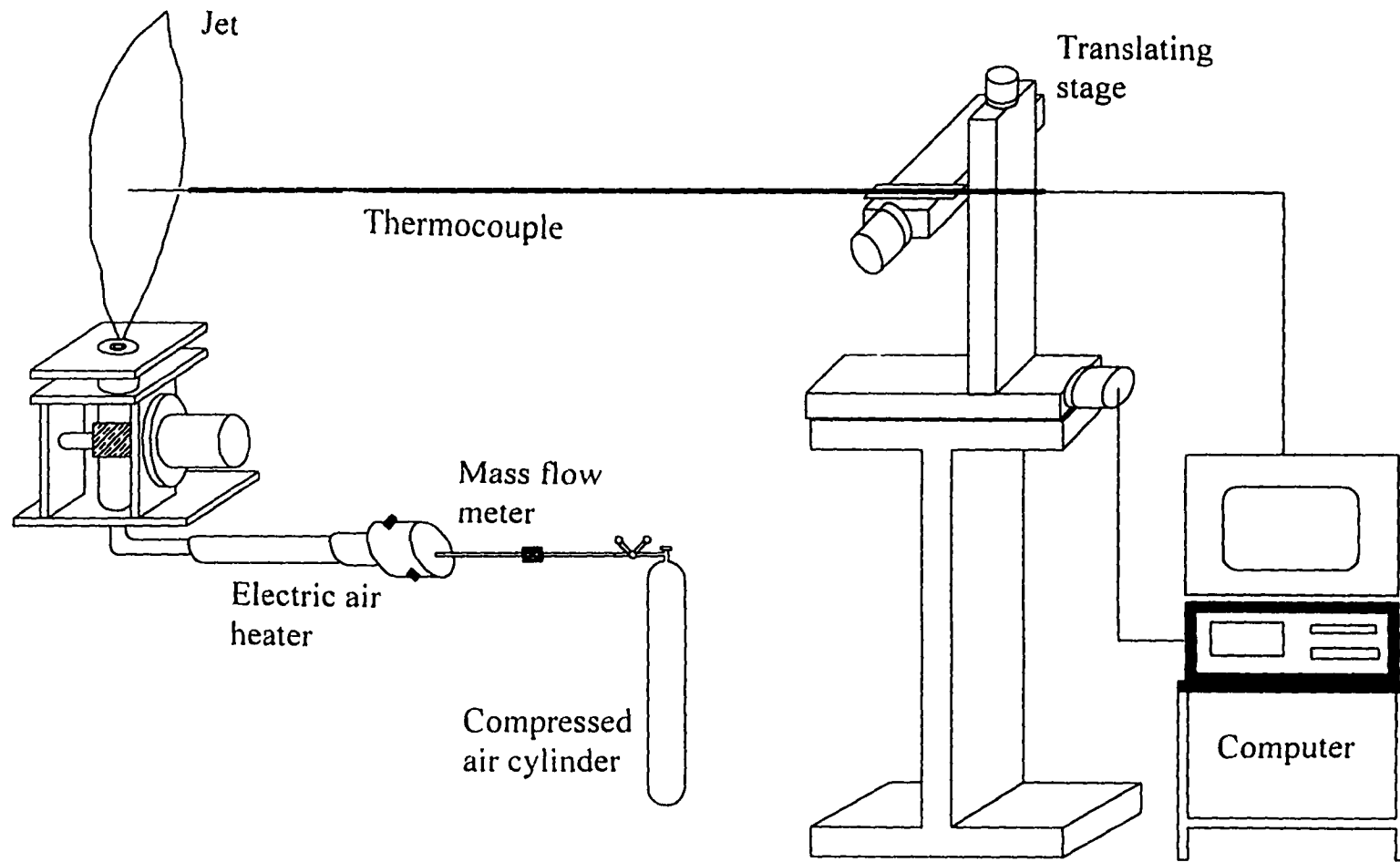


Figure 4.3 Three dimensional traversing system



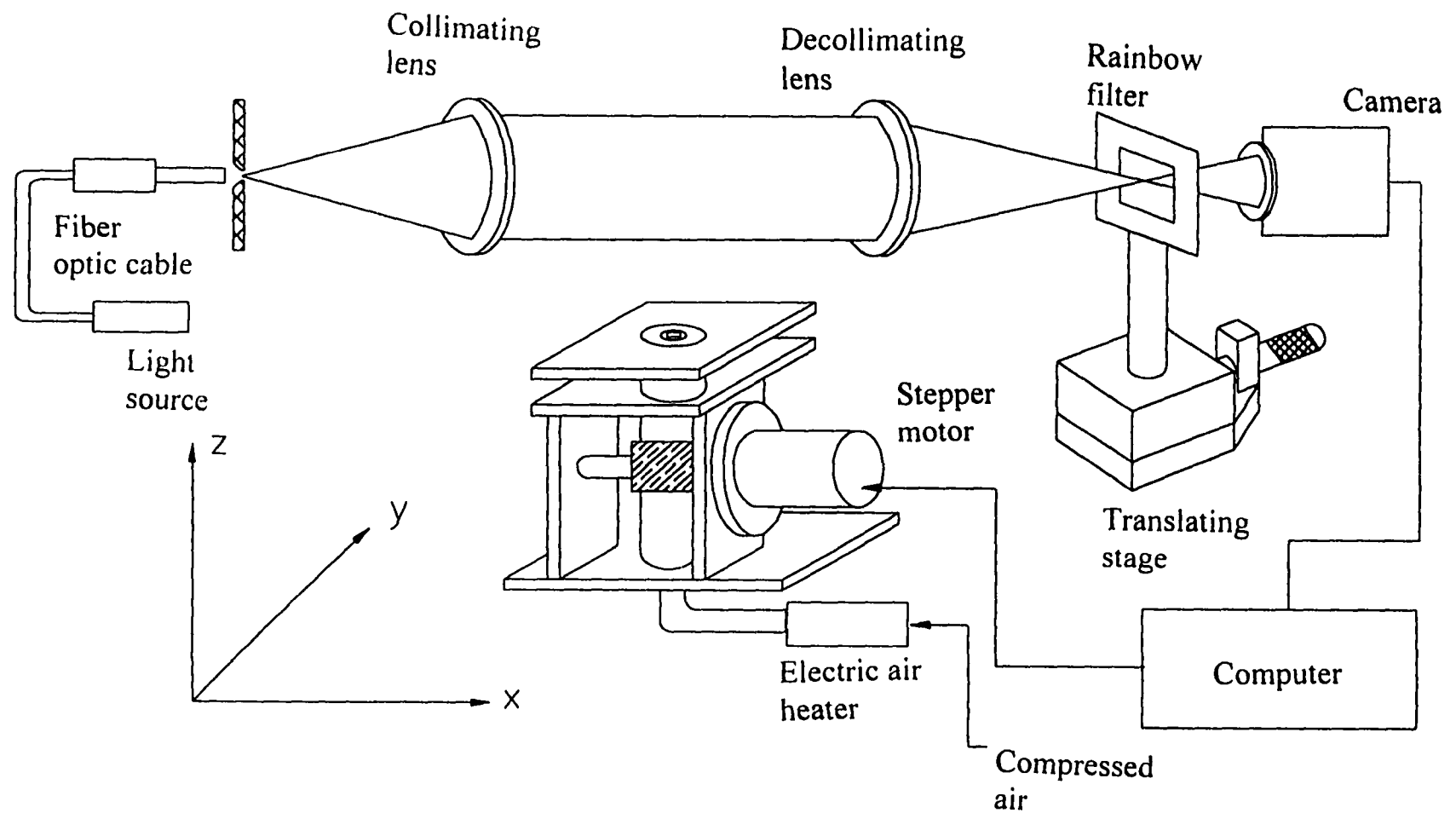


Figure 4.4 Setup showing filter calibration. No disturbance in test section

## Chapter 5

### RESULTS AND DISCUSSIONS

In this section, the discussion of measurements in the heated round jet, the inclined round jet, and the rectangular jet is presented. First, we shall present the discussion of the round jet which is followed by the discussion of the inclined jet and finally the discussion of the rectangular jet.

#### 5.1 The Round Heated Jet:

The results of the schlieren reconstruction of the axisymmetric heated air jet temperatures are discussed. All the results presented were reconstructed using the convolution backprojection (CBP) algorithm discussed in Chapter 3. This algorithm meant for asymmetric fields can be used to reconstruct an axisymmetric jet since in this case the projections are independent of the viewing angle, and as such the measured single projection in one direction is simply duplicated the desired number of times to obtain the required number of views. A schlieren photograph of one view of the round jet is shown in Appendix B.2

Figure 3.2 shows the calibration curve used in the reconstruction. The steps involved in the reconstruction are shown in Figure 5.1a,b,c and d. Sample calculations are shown in Appendix A.5. First of all, the hue of the captured image for a particular scan line is determined and is shown in Figure 5.1a. Using the calibration curve the deflections corresponding to the recorded hues are determined. These are shown in Figure 5.1b.

Using these deflections, the beam deflection tomographic algorithm is implemented in order to reconstruct the refractive index field which is shown in Figure 5.1c. Finally, using the Gladstone-Dale relation (see equation 3.26) the temperature field was determined as shown in Figure 5.1d. All these steps were incorporated into the reconstruction computer program. The asymmetry that is seen in Figures 5.1a and b was caused by the noise in the data. During reconstruction the backprojection algorithm (which is a summation process) acts as an averaging process [Faris and Byer (1988)], in essence reducing the noise in the data and restoring some symmetry and smoothened data as seen in Figure 5.1c.

To investigate the effects of unsteadiness of the jet on the results, 10 consecutive images were acquired and used to reconstruct the temperature field measured immediately after the acquisition of the images. Figure 5.2a shows the resulting hue plots of the images, and Figure 5.2b shows the mean hue with corresponding error bars (determined statistically as described in Chapter 4) at each point. This hue plot is the first step in using rainbow schlieren method to reconstruct the temperature field. Figure 5.2 clearly shows the effects of unsteadiness of the jet on the results.

Now with 10 consecutive images acquired, there are two ways to proceed in reconstructing the temperature field. One way is to take an average of the hue of all the 10 images and use this mean hue to reconstruct the temperature field. The other way is to use each image separately and reconstruct the temperature field corresponding to each image. The resulting temperature to be compared with thermocouple data, is then simply the average of all the temperatures from each individual image. Both of these approaches

were implemented using the basic 10 images and Figure 5.3 shows the results as compared with thermocouple data. From the figure, it is clear that both approaches are not the same, better comparison with experimental thermocouple data was obtained by averaging the hue of the 10 images than averaging the temperatures. The reason for this is because of the non-linearity of the process. The reconstruction errors accumulated when each individual image was used for reconstruction. Hue averaging results in less reconstruction errors since reconstruction is performed only once. Therefore, the rest of the results will be presented using this method.

The errors due to jet unsteadiness were calculated statistically as described in chapter 4 using 95% confidence level and student's t-distribution. Sample calculations are shown at the end of chapter 4. The results indicate a maximum error in the schlieren reconstruction of about 13 % caused by room air disturbances. The same procedure was used to evaluate the thermocouple errors which were found to be 2% of the mean temperature recorded. Other sources of errors are analyzed in the uncertainty analysis shown in Appendix A.6.

Figures 5.4a, b, and c show the comparison of reconstructed temperature using the mean hue of 10 images with thermocouple measurements at axial locations of 5mm, 10mm, and 15mm above the jet exit. The figures also indicate the error bars calculated statistically as described above. It is seen that for all locations, the reconstructions using the schlieren technique compare reasonably well with the thermocouple measurements. The reconstructions at axial locations of 10 mm and 5mm are better than that at 15mm, due to the unsteady nature of the jet further downstream. Figure 5.4d shows the error bars

on both thermocouple data and schlieren data for the 5mm location. As indicated above the thermocouple errors were estimated at 2%.

Figures 5.5a, b, and c are comparison between temperatures obtained from single schlieren images taken during thermocouple measurements. The images was captured by visual observation of the most steady symmetric image. The data are again for axial locations 5mm, 10mm, and 15mm. Again to within experimental error the data compare well. The same trend in data is also evident as discussed above. The instability at axial location  $z = 15\text{mm}$  is obvious. At station  $z = 10\text{ mm}$ , the oscillations at the center of the schlieren reconstruction, may be attributed to the noise that is present. Comparing this figure with the corresponding Figure 5.4b, it is noticed that Figure 5.4b has less noise than Figure 5.5b and therefore lacks the oscillations observed in the center point data of Figure 5.5b.

So far, the above discussion has focused on the reconstruction along the axis parallel to the light rays. When taking thermocouple measurements, it was noticed that, because of the inherently intrusive nature of the thermocouple, there were errors associated with thermocouple measurement. These errors were more pronounced in the data taken normal to the light rays. This was because when taking measurements in this direction, the thermocouple intruded more into the flow and disturbed the symmetry of the jet more in this direction, than in the direction parallel to the light rays. This is seen in the reconstructions for this axis shown in Figures 5.6a and b. Figure 5.6a is reconstruction for the 5mm axial position and Figure 5.6b is the reconstruction for axial

position of 10 mm. Despite the asymmetry of the thermocouple data, the reconstructions are good especially for the 10 mm axial position.

## 5.2 The Inclined Round Heated Jet

Next, we discuss the comparison between experimental thermocouple measurements and the schlieren technique results for the inclined jet. Thermocouple traverse measurements were performed at two locations downstream of the inclined jet. These were at the locations  $z = 5$  mm and 10 mm. At each location, measurements were performed along the axis parallel to the light rays and along the axis normal to the light rays. The measurements along the axis parallel to the light rays were performed along the x-axis ( $y = 0$ ) with the origin centered at the axis of rotation at the perpendicular plane coinciding with the jet exit. With this coordinates system (as discussed in chapter 4 and shown in Figure 4. ), the jet exit was inclined and shifted about 10 mm from the origin.

Figure 5.7 shows the contours of a vertical plane through the line  $y=3$ mm and parallel to the light rays. In this plane the development of the jet vertically can be visualized. Appendix B.3 shows two schlieren photographs of two views of the inclined jet. It is seen from figure 5.7 that in relation to the center of the test section the visible jet was confined to the extreme end of the test section. A part of the jet was outside the schlieren view area at heights above 5mm. This was also observed in the horizontal contour plots described below. The three-dimensionality of the jet was accurately

reconstructed by the schlieren technique. The highest temperature shown was about 380 °K and the jet profile can be observed upto a height of about 17mm.

Figure 5.8 shows the contour plots of the reconstructed temperatures at  $z=5\text{mm}$ . From the figure, it is clear that the jet exit was slightly shifted to the right of the z-axis, according to the coordinate system discussed above (chapter 4). The light rays were parallel to the x-axis, and therefore, the direction of inclination of the jet was away from the center of the test section. Figure 5.9 shows the contour plots of reconstructed temperatures at  $z=10\text{ m}$ . It is noticed that the jet is shifted further away from the x-axis and that it is right at the border of the reconstructed region with a part of the contours cut-off. Figure 5.10 shows the contour plots at  $z=15\text{ mm}$ , where it is now clear that the jet has developed to outside of the reconstruction region. These contour plots corroborate the vertical contour plots of Figure 5.7 discussed above.

Figure 5.11 shows the comparison of the thermocouple measurements with schlieren results for the axis perpendicular to the light rays at the line  $x=12\text{ mm}$ . The comparison is very good, except at the center and at the left boundary. The discrepancies can be explained as due to the errors inherent of the schlieren technique and discussed in details, in a previous chapter. Figure 5.12 shows the reconstructions along the  $y=0$  axis, i.e. parallel to the light rays. Again, the agreement with thermocouple measurements is good. The slight increase in temperature to the left of the origin between  $y=-5\text{mm}$  and  $y=-10\text{mm}$  is due to the convection currents rising from the bend region of the tube and from the mounting system of rotation.

Figure 5.13 shows the reconstruction of the location  $z = 10$  mm at the  $x = 15$  mm coordinate line. The  $x$ -coordinate of the measurement axis was not the same as for the location  $z=5$  mm. The thermocouple measurement location was changed in order to follow the jet as it shifted further away from the  $z$ -axis downstream of the jet axis. The agreement between the schlieren measurement and thermocouple measurements were good at this location. Figure 5.14 shows the reconstruction at  $z = 10$  mm for the  $y=0$  line. The comparisons between thermocouple and schlieren follow the same trend as above except that the thermocouple measurements are wider than the schlieren measurements. This discrepancy can be explained as due to the Gibbs phenomena present in the reconstruction algorithm and explained by Hughey and Santavicca (1982). This error in the reconstruction occurs when there is a discontinuity in the refractive index of the flow field. In the contour plot of Figure 5.9, the discontinuity is seen to occur at the upper boundary where the outer contour of the jet is seen cut-off. Because of this, there is a discontinuity in the refractive index at this location.

### **5.3 The Heated Rectangular Jet:**

In this section, we present results of the development of the heated rectangular jet. First of all results of the comparison of temperatures reconstructed using the schlieren technique and thermocouple measurements obtained at three  $x$ -locations along the axis of the jet in the downstream direction are presented. The results for the development of the jet are presented last.



Figures 5.15a, and b show the comparison of the thermocouple measurements with schlieren measurement at  $z = 5$  mm above the nozzle height. The comparison for the major axis are shown in 5.15a and those for the minor axis in 5.15b. The comparison of temperatures for the major axis is good except at the center. The thermocouple errors were determined statistically as described in chapter 4 to be  $\pm 2\%$ . It was found that the main cause of discrepancies is due to the jet unsteadiness caused by air currents in the room. In the section on the round jet, details of the errors was pointed out to be  $\pm 10\%$  and that this error can be minimized if the jet is stabilized by carrying out experiment in a completely quiescent surroundings. When this error is eliminated the errors that are left are small ( $< 3\%$ ) and are caused by other sources of errors discussed in Chapter 4. These errors including the fixed errors inherent in the schlieren technique itself have also been discussed and an uncertainty analysis is shown in Appendix A.6. The noise in the data was mainly due to convection currents rising from the heater and the rotating mechanism enclosure. Insulation could not completely eliminate the convection currents. Within the experimental error, therefore, the thermocouple measurements and schlieren measurements compare well.

Figures 5.16a and b show the comparisons of data at  $z = 10$  mm. The comparison here is closer than at  $z = 5$  mm. This simply indicates that the image used for the reconstruction was closer to the mean value sensed by the thermocouple. The thermocouple readings were obtained over a 10-15 minute period as described in the experimental chapter. Readings at each point of transverse were sampled for 10 s at the rate of 10 samples per second, from which a mean value was determined for each

traverse point. When capturing the schlieren image to be used for the reconstruction, care was taken in order to capture an image that represented a mean of the fluctuations due to the jet unsteadiness. These disturbances caused the jet to sway about the  $z$ -axis, the image that was vertical was therefore considered the mean image. The disturbances of the jet could of course have been eliminated by enclosing the jet in a chamber with glass windows. This was not done however because we wanted a simple system to prove the rainbow schlieren imaging technique without introducing complications caused by deflections through optical glass windows. In systems with glass windows it is possible to incorporate this fact in the computation having demonstrated the validity of the technique.

Figures 5.17a and b show reconstructions at  $z = 15$  mm. The thermocouple results shows while comparing the data of all the three  $x$  stations of the jet's major axis, the jet has spread outwards. The comparison on the minor axis, on the other hand, is not quite obvious. It will be shown below that the jet spreads out more in the plane of the major axis than in the plane of the minor axis.

Figures 5.18a, b and c show the temperature contours at  $z = 5, 10$ , and  $15$  mm respectively. From the plots it is evident that the jet spreads more on the major axis than on the minor in this near nozzle region of the jet. The contours closer to the nozzle at  $5$  mm are less smooth than the downstream contours. This was found to be a problem of the reconstruction technique caused by limited number of rotational views. To reconstruct the temperatures, the jet was rotated at  $50$  angular positions to obtain  $50$  images used in the reconstruction. Because closer to the nozzle the field is more three

dimensional, more views are required for accurate reconstructions. Improved reconstructions were obtained when the images were increased to 99 by linear interpolation. This fact suggests that the convolution backprojection algorithm is not suitable for limited view reconstructions. For situations where the number of views is limited, algebraic techniques of reconstruction are preferred [Dufang (1995)].

Figures 5.19 and b are plots of temperature contours in a vertical plane showing clearly the extent of the heated jet. Two schlieren photographs of the jet at two different view angles are shown in Appendix B.4. Figure 5.19a is the plot of the jet spread in the major axis and 5.19b is the plot for the jet spread in the minor axis. From the plots it is clear that the jet spreads more in the major axis than in the minor axis.

Figure 5.20a shows a plot of jet half width distance. The jet half-widths  $Y_{1/2}$ ,  $X_{1/2}$  defined as the distances from the centerline of the jet to the point where the axial mean temperature in each plane is equal to one half of its centerline value. The jet width in the major axis is denoted  $Y_{1/2}$  and the jet in the minor axis is denoted  $X_{1/2}$ . Figure 5.20b and 5.20c shows these plots non-dimensionalized by equivalent diameter  $D_e$ . Define a combined half-width as  $Y_c = (Y_{1/2} X_{1/2})^{1/2}$  [Hussain and Hussain (1989)]. The jet in the major axis spreads faster than in the minor axis and the combined half width spread lies in between the spreads for the major and minor axes-see Figure 5.21. The combined half-width can be used to characterize the overall behavior of the heated rectangular jet. Krothapalli (1981) reported a linear growth rate of the minor axis and a nonlinear growth rate of the major axis in their study of momentum jets. Chin-ming Ho and Gutmark (1987) also observed the same trend.

Figure 5.22a shows a plot of the decay of centerline temperature. Previous investigators have identified three regions of flow issuing out of a heated rectangular jet; an initial region close to the nozzle where the center line temperature is fairly constant, followed by a second region where the decay of centerline temperature is proportional to  $x^{-1}$ , and then a region extending to infinity where the centerline temperature decay is similar to that of a jet issuing from a circular crosssection. These three regions are termed, the potential core, the two-dimensional region and the axisymmetric region respectively. From Figure 5.22a the trend suggest the two dimensional region. Figure 5.22b shows the plot of the two dimensional region fitted with a linear curve. In this two dimensional region the temperature decay profile follows the equation [Sfeir(1976)]:

$$\left[ \frac{T_c - T_a}{T_e - T_a} \right]^2 = k(\bar{z} - c)^{-1}$$

where  $T_c$  is centerline temperature,  $T_a$  is ambient temperature,  $T_e$  is jet exit temperature,  $k$  and  $c$  are constants and  $z$  is the dimensionless downstream distance (in this study the length dimensions were nondimensionalized with equivalent diameter  $D_e$  as defined by Hussain and Hussain (1989) and equal to the diameter of a round jet with same momentum flux area as the rectangular jet). Figure 5.22c shows the fit of the two dimensional region temperature decay data to the above equation. In this figure  $\eta = (z - c)^{-1}$ . The fitting to the equation is good. A value of  $k = 3.1$  was obtained. Zijnen(1954) obtained a  $k$  value of 4 for his heated turbulent rectangular jet.

Figures 5.23a and b show the temperature profiles at four z locations (z = 7mm, 14.3mm, 23.4 mm and 32.5 mm) across the major axis of the rectangle. In Figure 5.23a the spread of the jet is evident. Figure 5.23b are the same profiles in nondimensional similarity parameters as used by Zijnen(1958). The major axis temperature deficit  $\Delta T$  was nondimensionalized by centerline temperature deficit  $\Delta T_c$ , and y was nondimensionalized by  $\eta$ , where  $\eta=y/x-x_0$  in which  $x_0$  is the virtual origin. The equation he curve fitted to the data was:

$$\frac{\Delta T}{\Delta T_c} = \left[ 1 + 30\eta^2 + 2200\eta^4 - 30000\eta^6 \right] e^{-75\eta^2}$$

As found out by Zijnen(1958) the profiles seem to collapse into a single profile. This indicates that a similarity exists between the temperature profiles in this region. Zijnen's (1958) curve fitted equation to the profiles is also shown in Figure 5.23b. The curve fits the data fairly well except that it is a bit wider than the data. This may be due to the fact that Zijnen's data were for turbulent large aspect ratio rectangular jet as opposed to our laminar data. Figure 5.24a and b shows the same profiles across the minor axis corresponding to the same downstream z positions. In this plots the temperature jet spread is very small and Zijnen's curve fitted equation do not fit the profiles.

In order to be able to get a rough idea of how a heated rectangular jet develops, a comparison is made between the well known developments of the heated round and plane jet in Figure 5.25. The round jet with an aspect ratio of one and a plane jet with an infinite aspect ratio, are often quoted in literature as the limiting cases of three dimensional geometries. Because the round and the plane jets are two dimensional,

theoretical solutions are easy to obtain. In Figure 5.25, the plane and round jet solution were obtained using the simple method described by Kanury(1975). More detail analysis of the equations and solution procedure can be found in Brand and Lahey (1967) and in Gebhart (1986 ). The centerline temperature of a plane jet decay as  $x^{-1/3}$  and for a round jet the decay is as  $x^{-1}$ . Plotted in Figure 5.25 are the theoretical solutions of jet half widths for the round and plane jet and the schlieren experimental results of the rectangular jet . The half-jet width was calculated as discussed above. The development of the jet is shown in Figure 5.25 as starting off as a plane jet and growing towards the round jet shape.

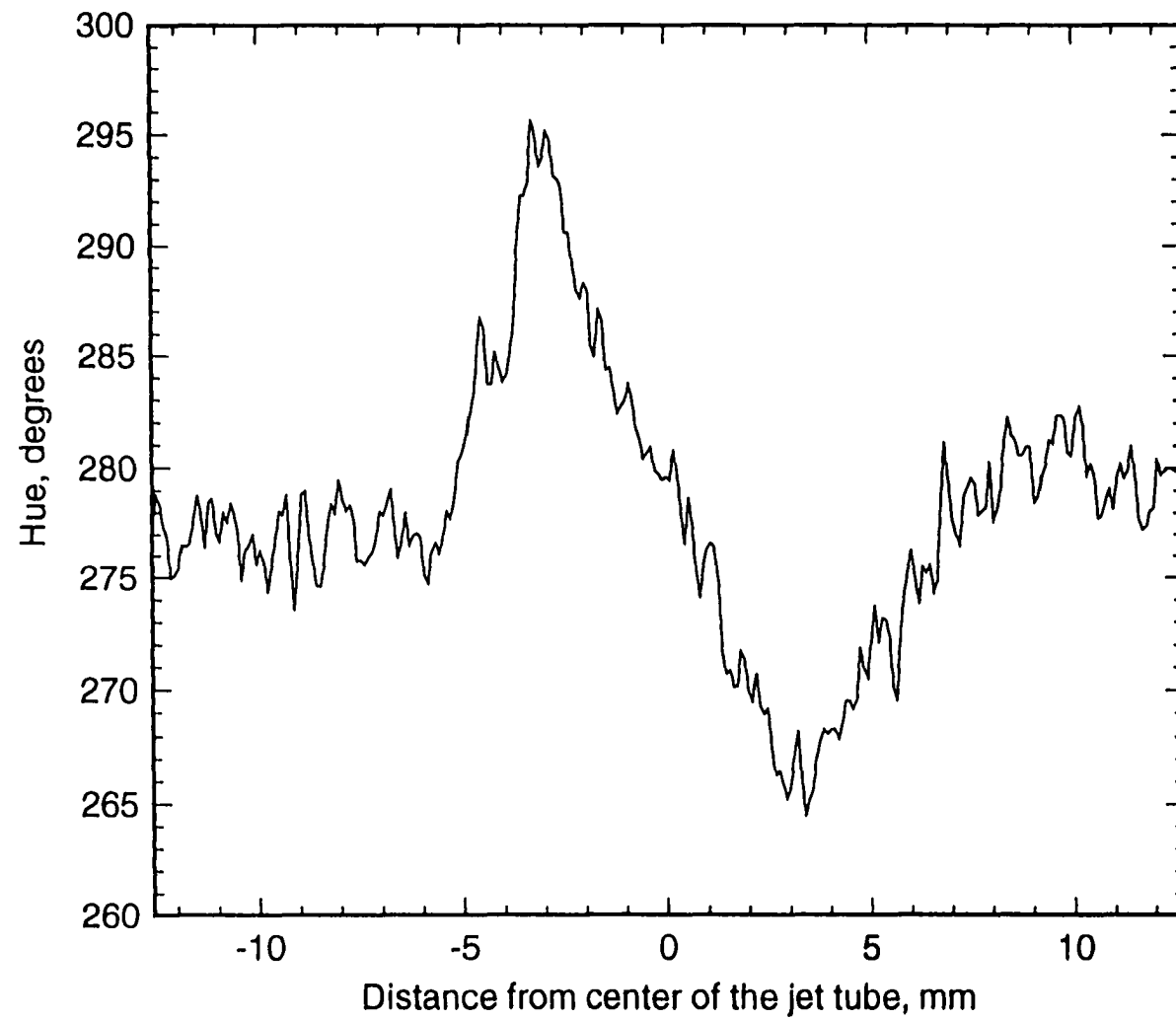


Figure 5.1a Plot of hue across a scanline

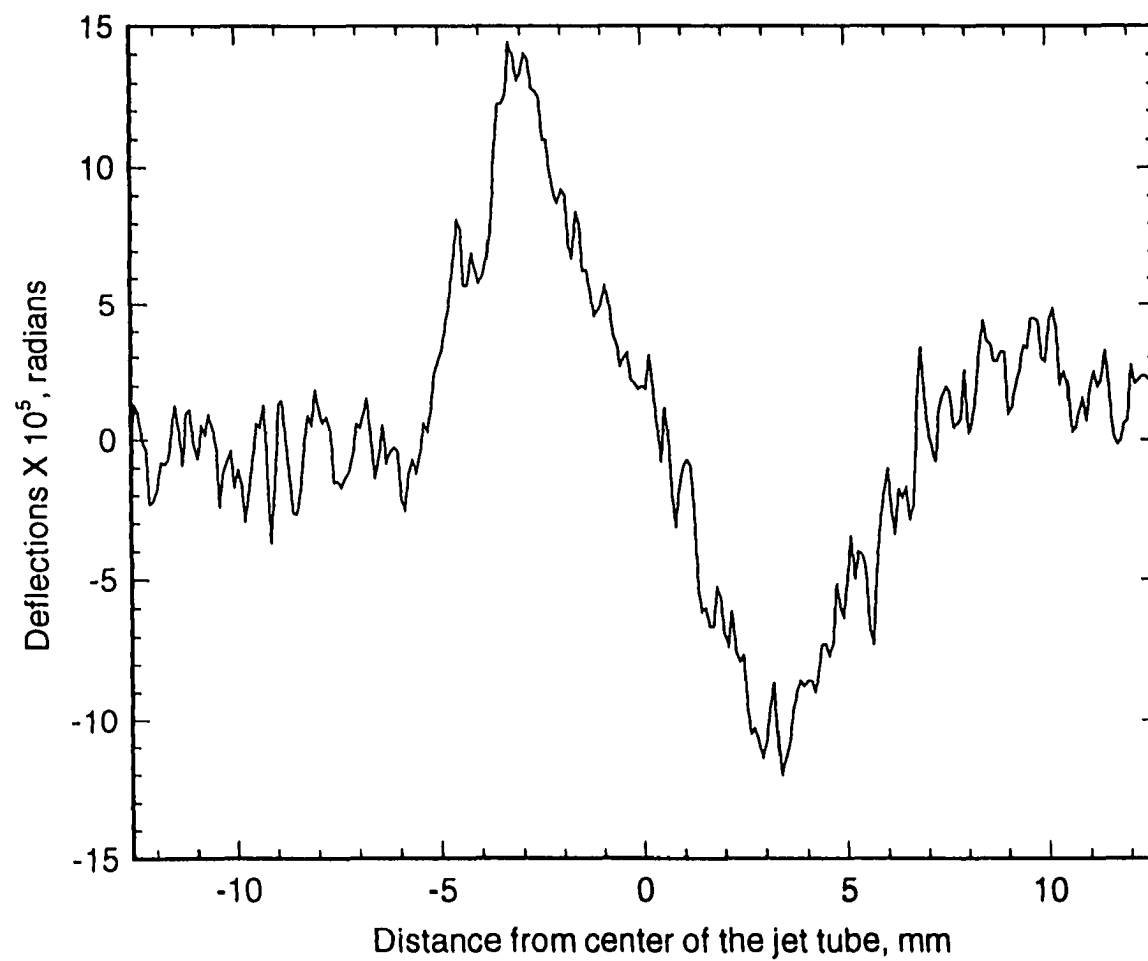


Figure 5.1b Plot of deflection across a scanline



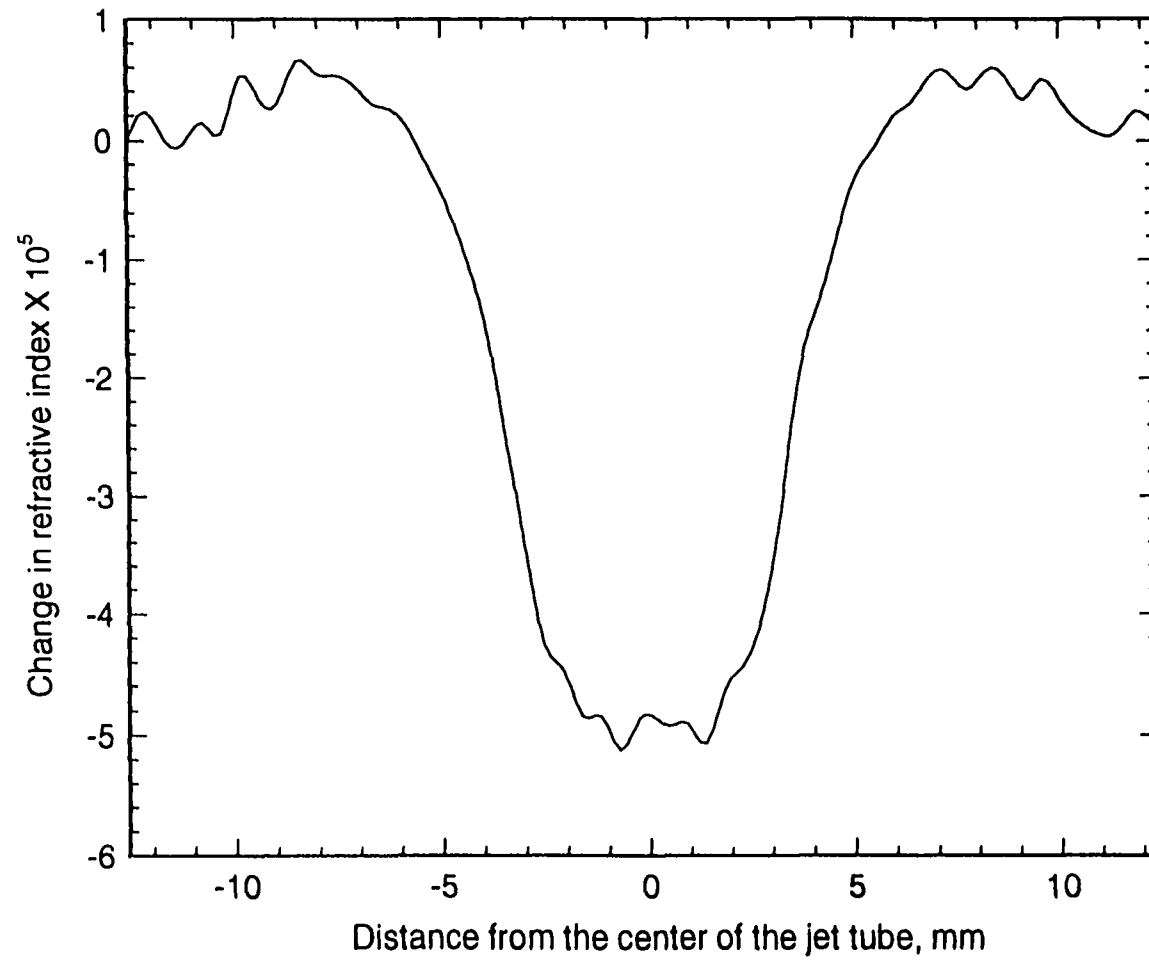


Figure 5.1c Plot of change in refractive index across a scanline

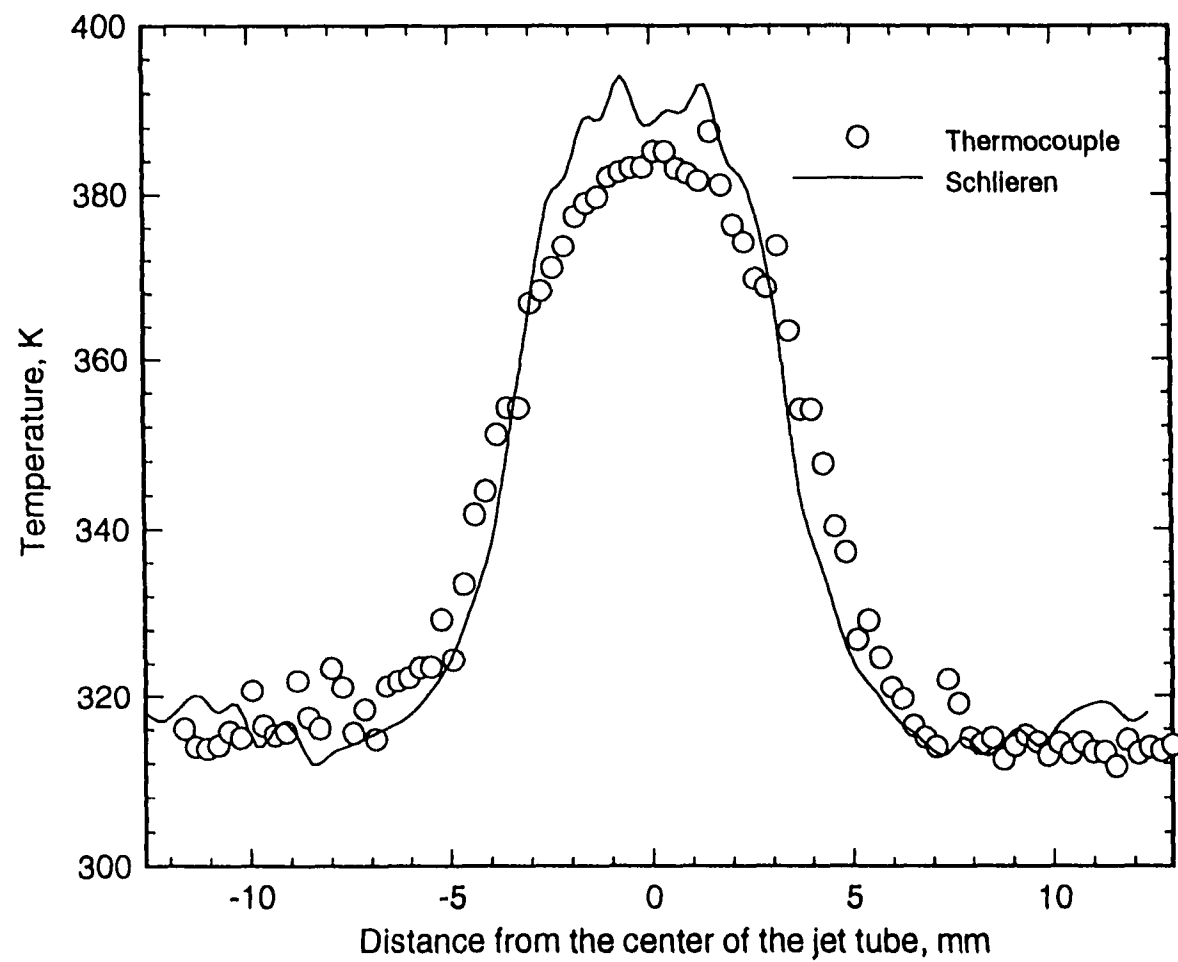


Figure 5.1d Plot of reconstructed temperatures across a scanline

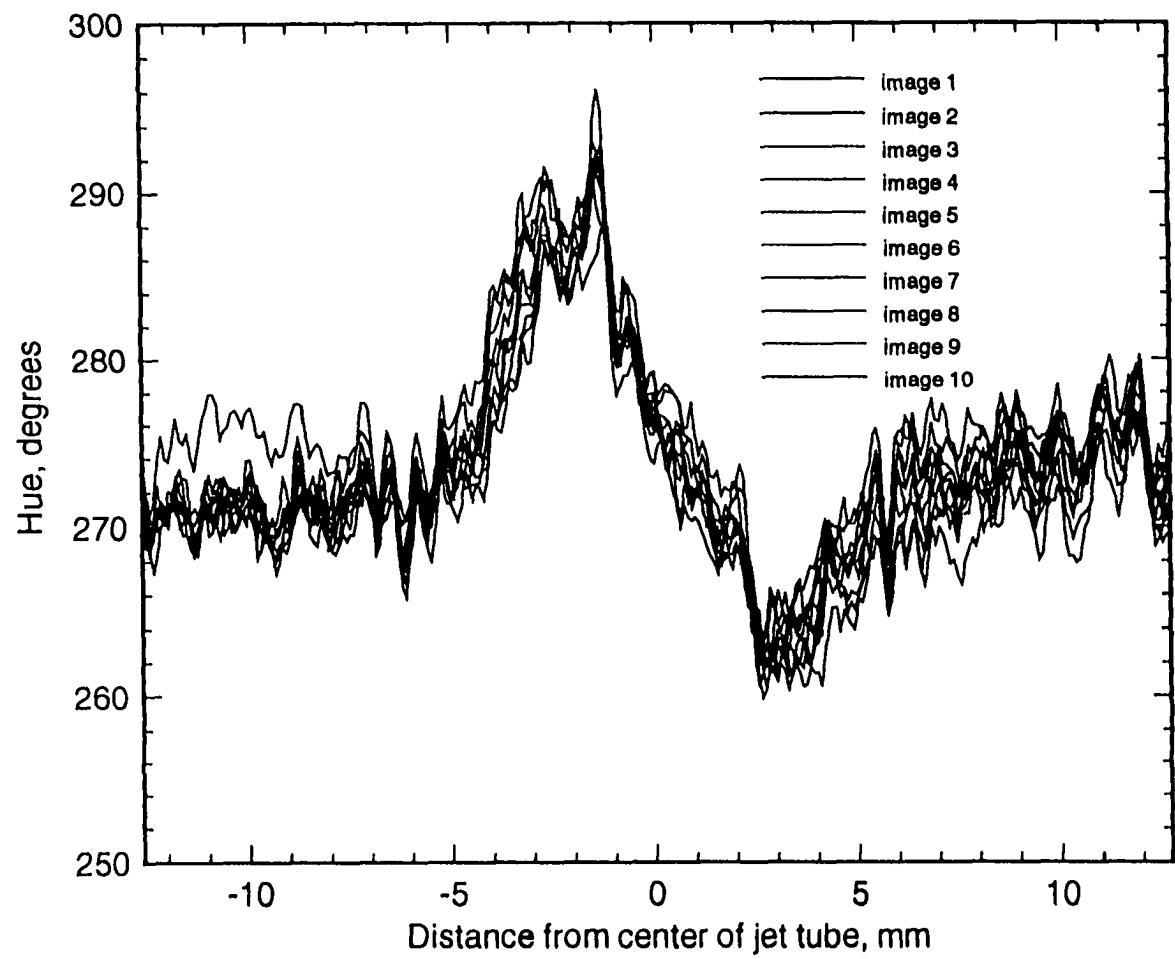


Figure 5.2a Plot of hue of 10 images

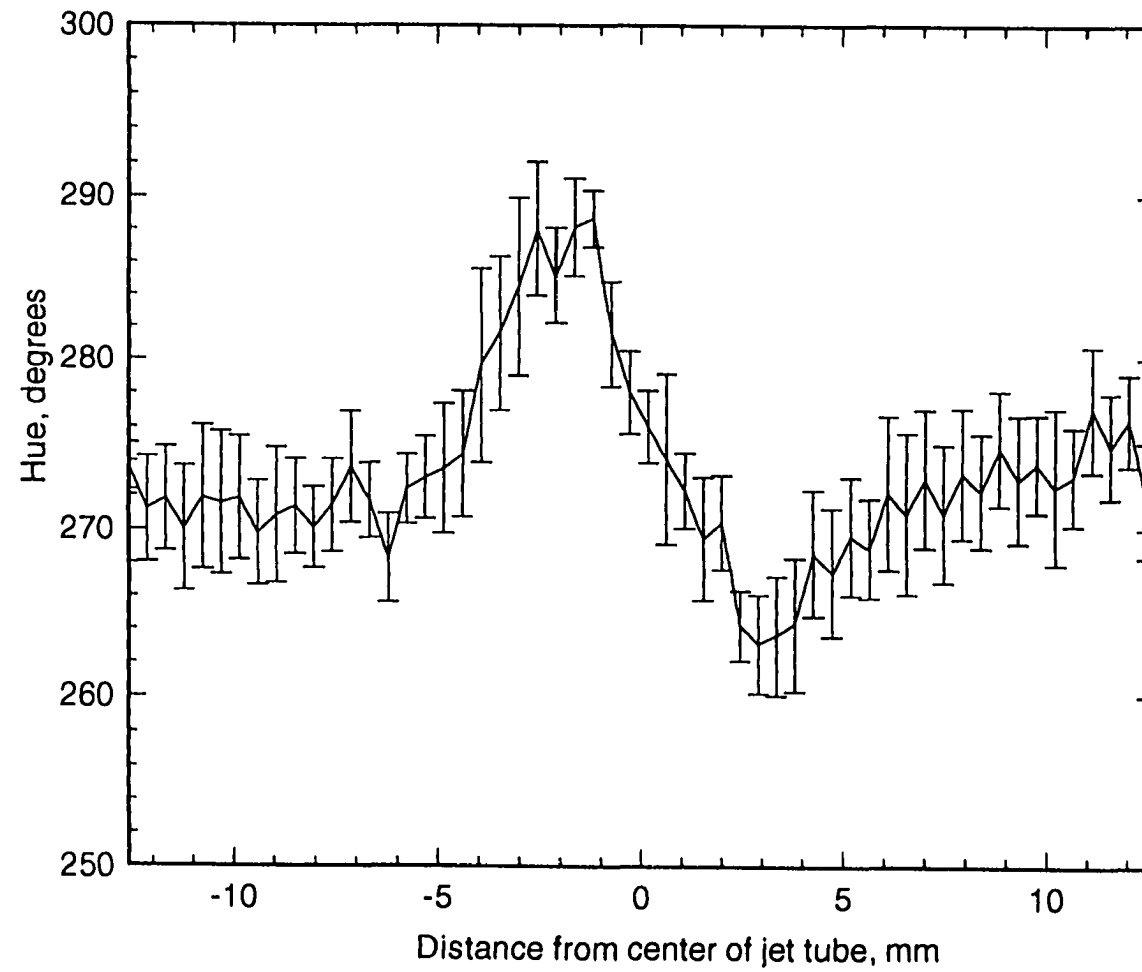


Figure 5.2b Plot of mean hue of 10 images with error bars

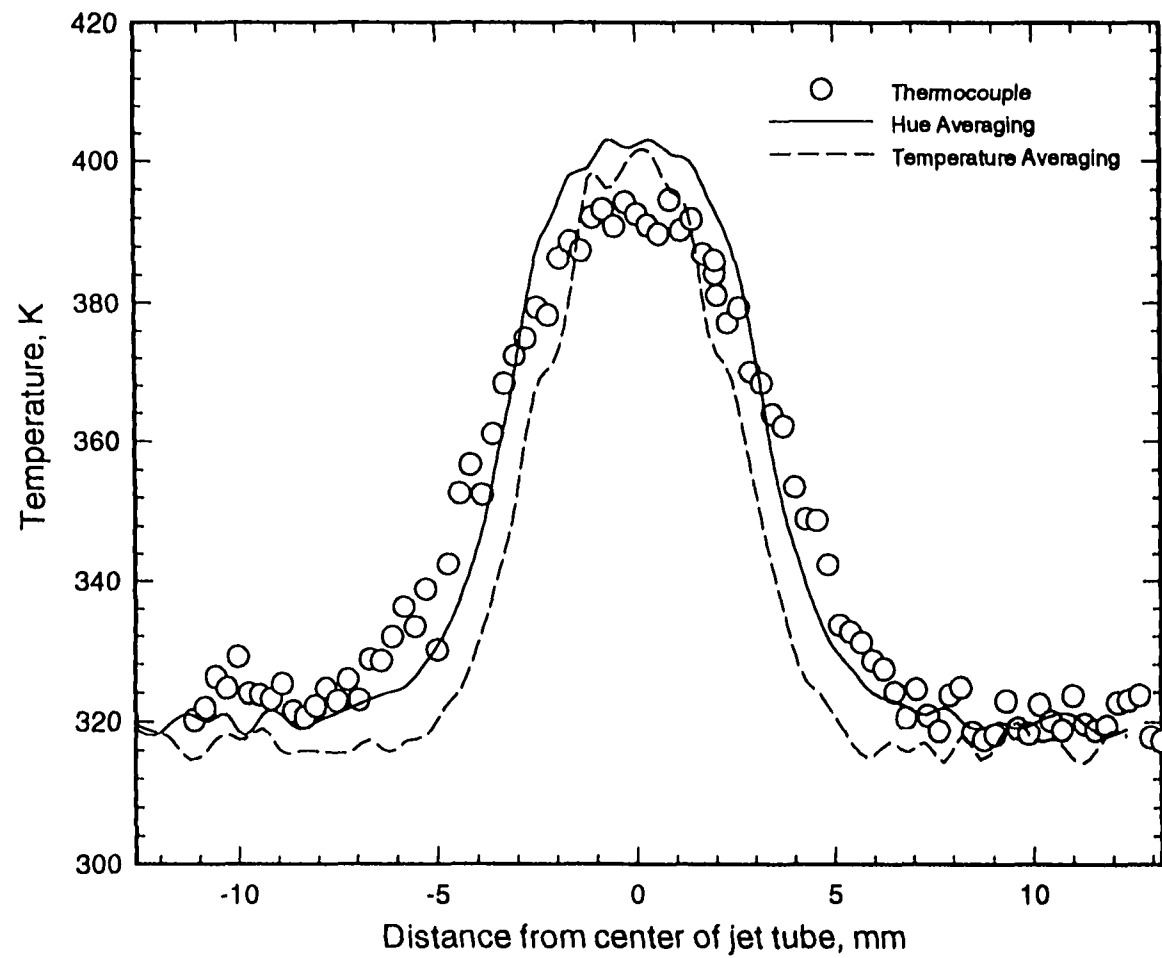


Figure 5.3 Effect of hue averaging and temperature averaging on the results

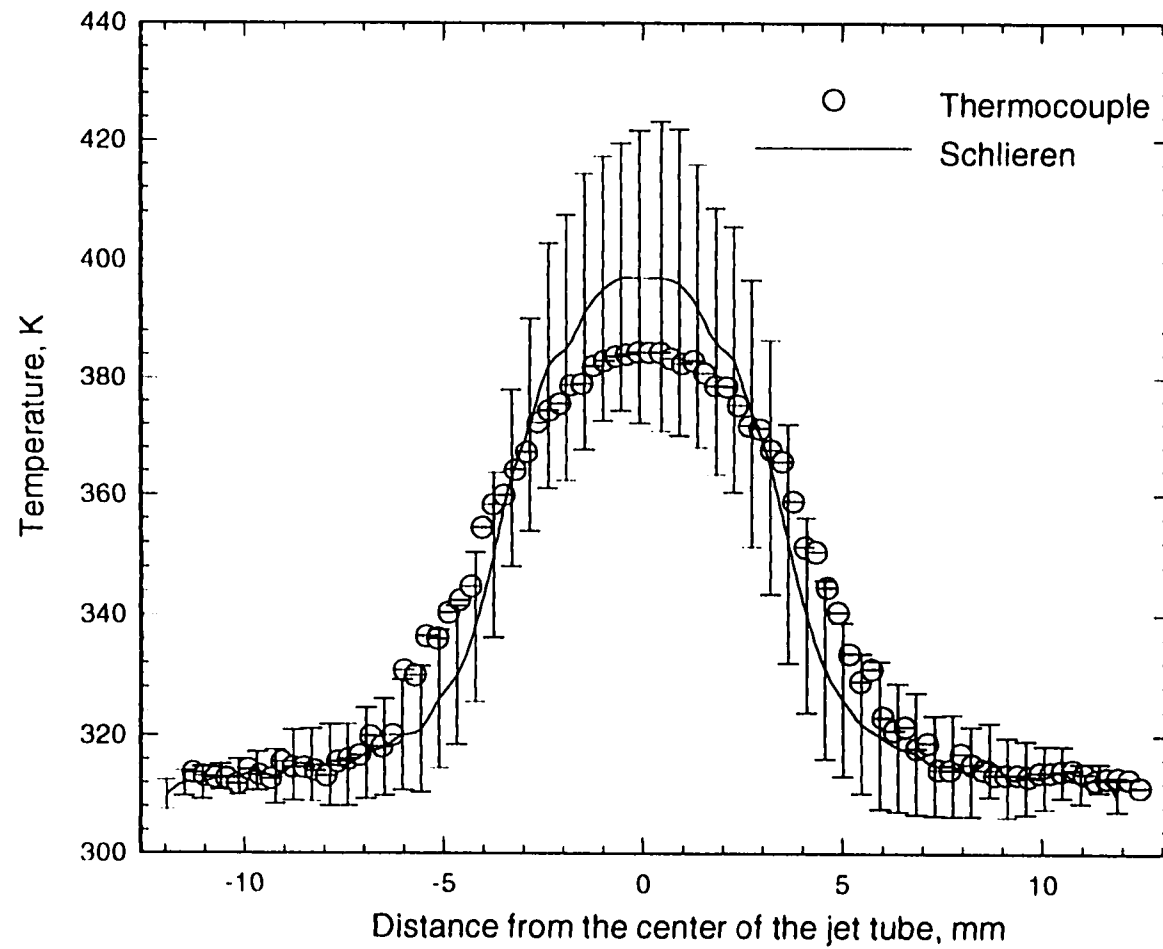


Figure 5.4a Comparison of reconstruction and thermocouple measurement at  $z = 5$  mm. Reconstruction using average hue of ten images across x-axis.

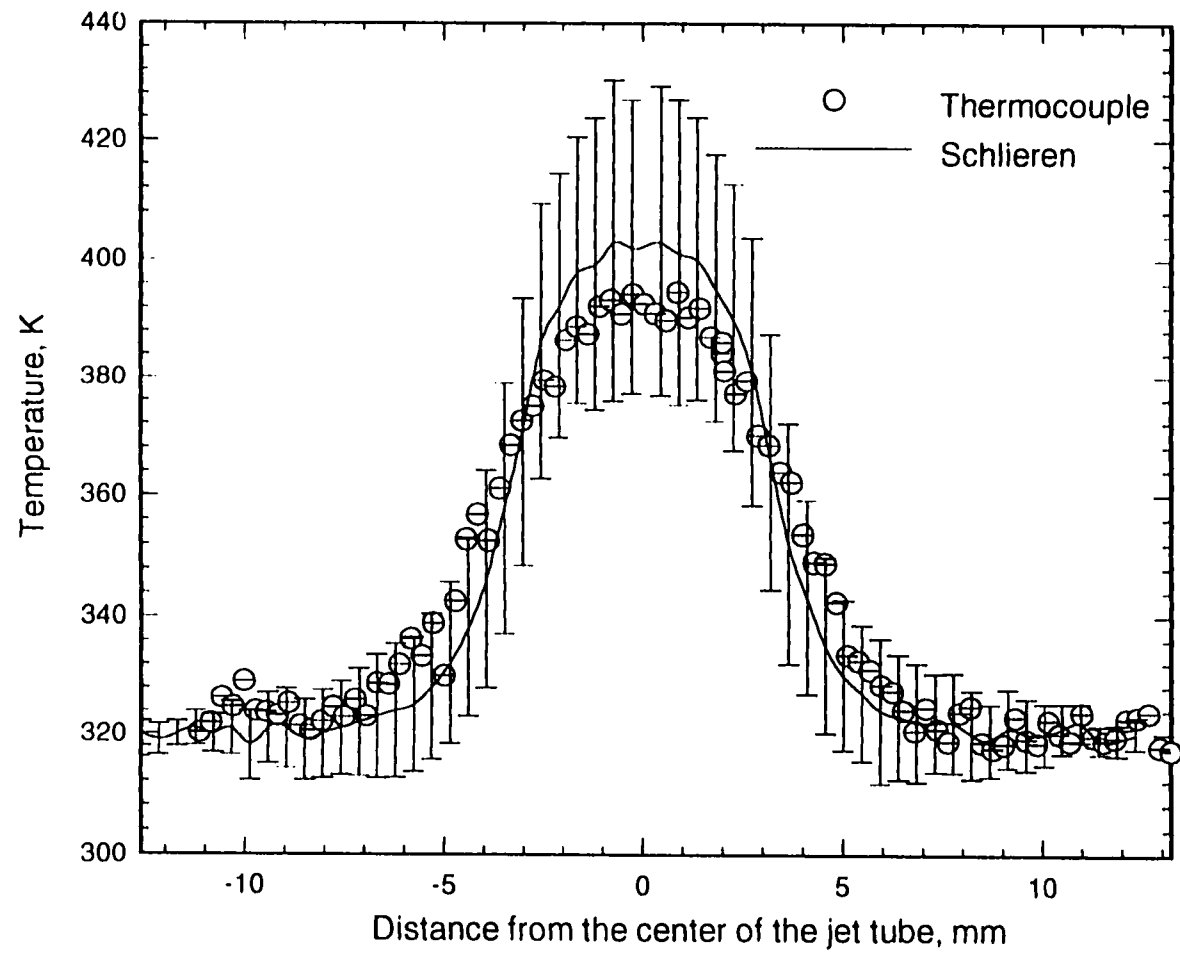


Figure 5.4b Comparison of reconstructions and thermocouple measurements at  $z = 10$  mm across x-axis.

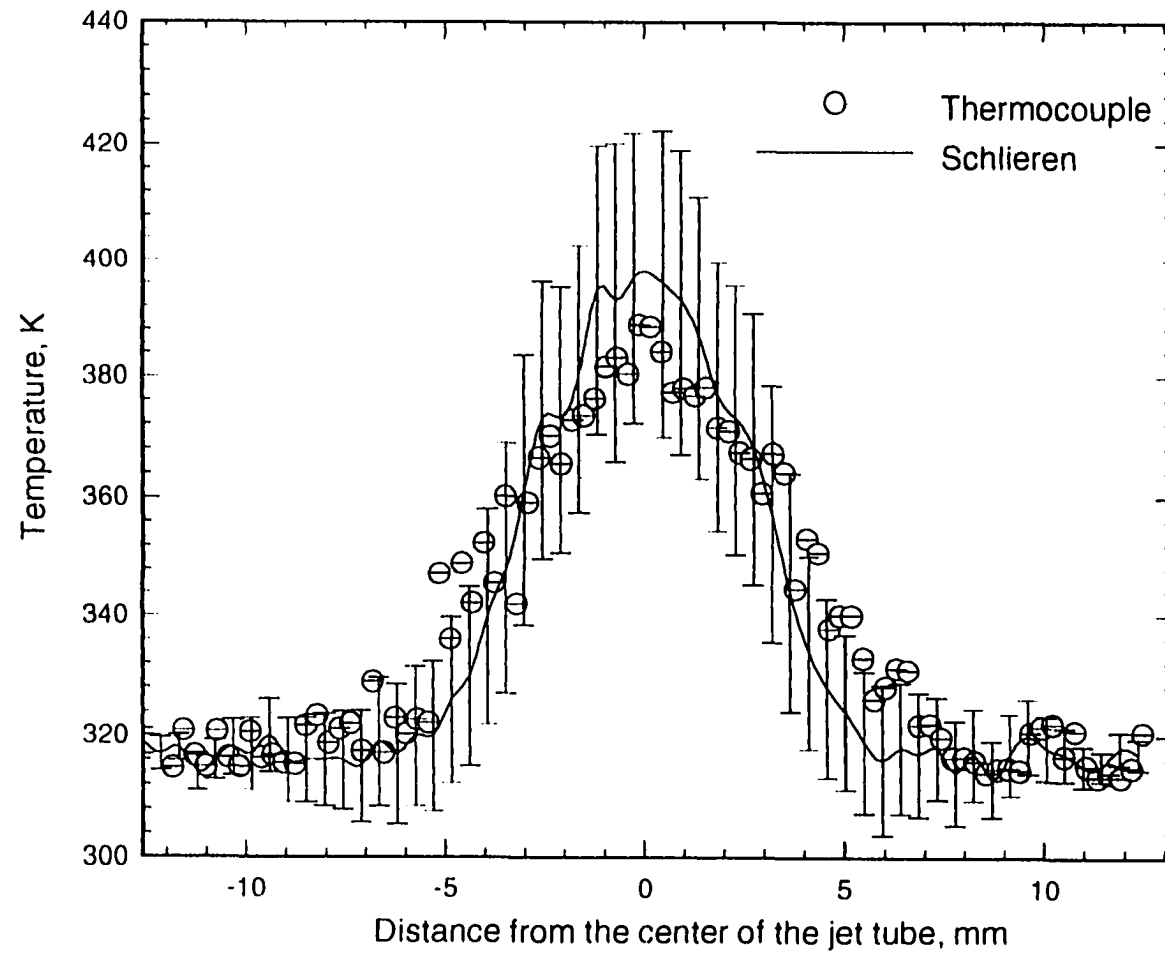


Figure 5.4c Comparisons of reconstructions and thermocouple measurements at  $z=15$  mm across x-axis.



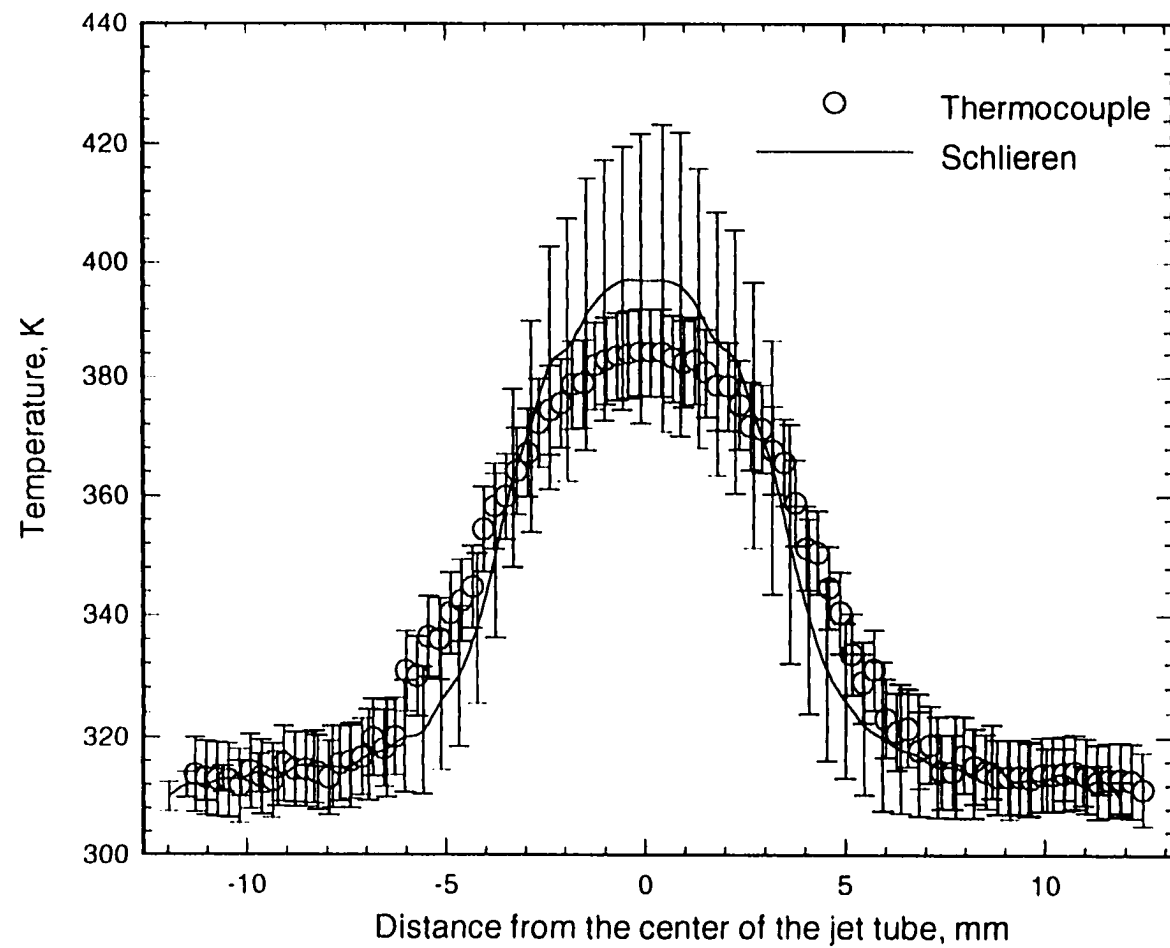


Figure 5.4d Comparisons of reconstructions and thermocouple error bars for measurements at  $z=5$  mm across x-axis.

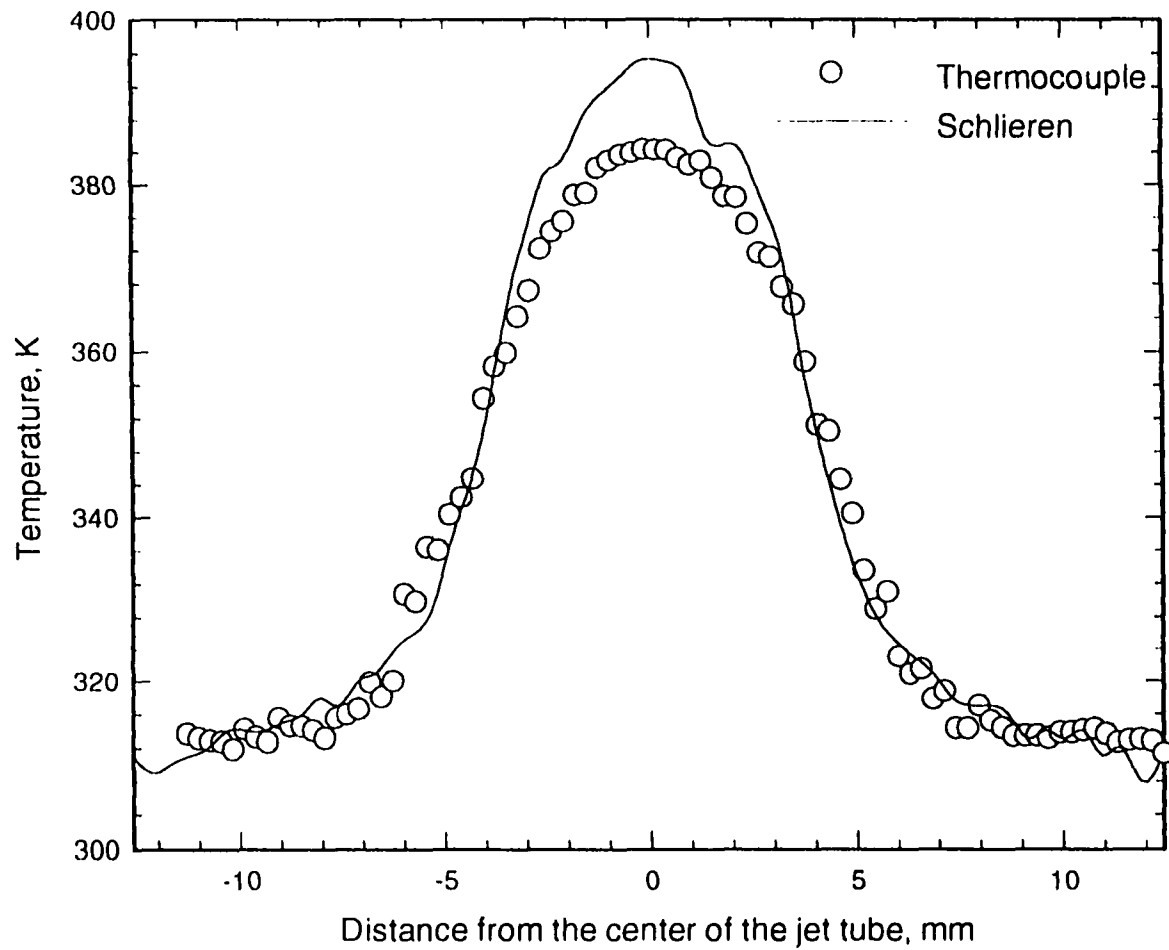


Figure 5.5a Comparison of reconstructions from single schlieren image and thermocouple measurements at  $z = 5$  mm across the x-axis.

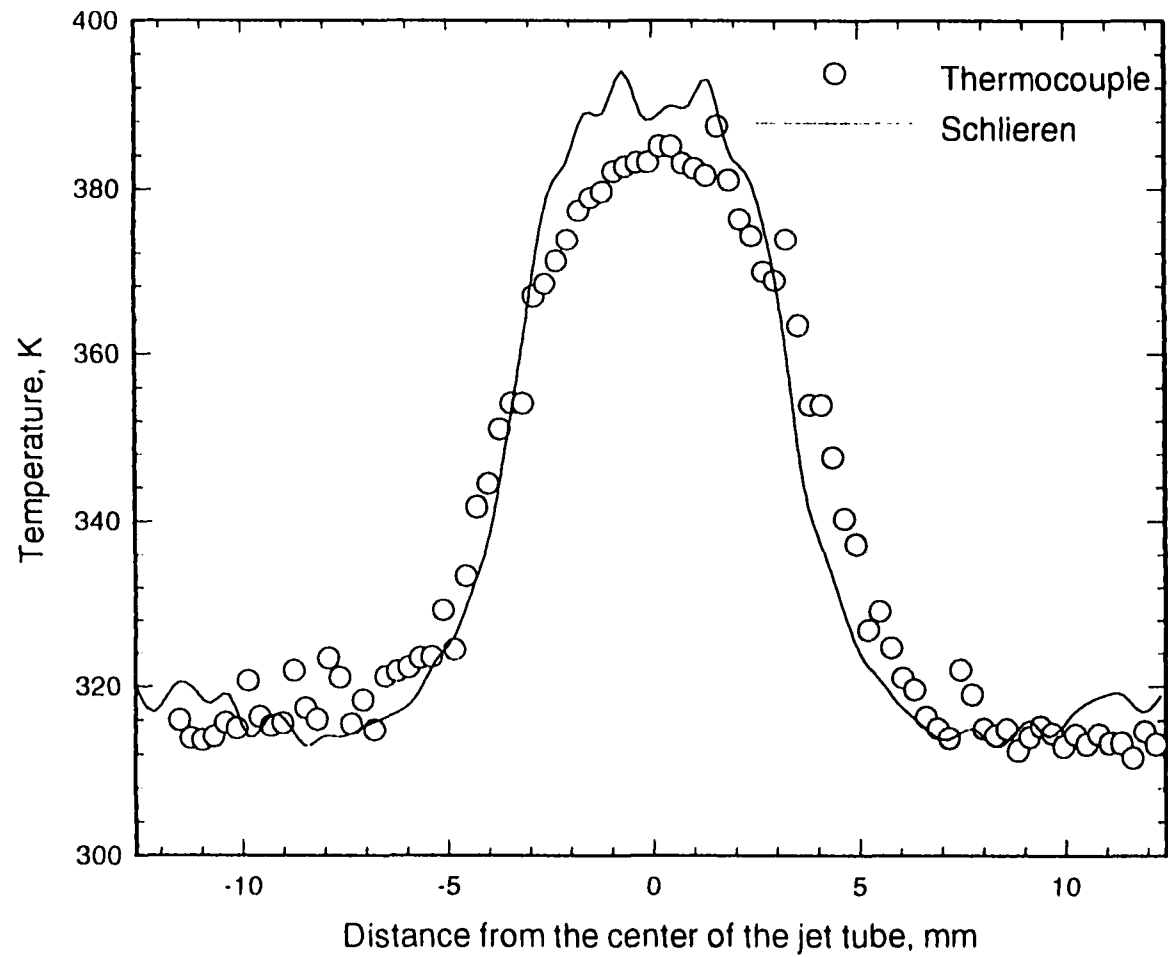


Figure 5.5b Comparison of reconstruction from single schlieren image and thermocouple measurements at  $z = 10$  mm across  $x$ -axis

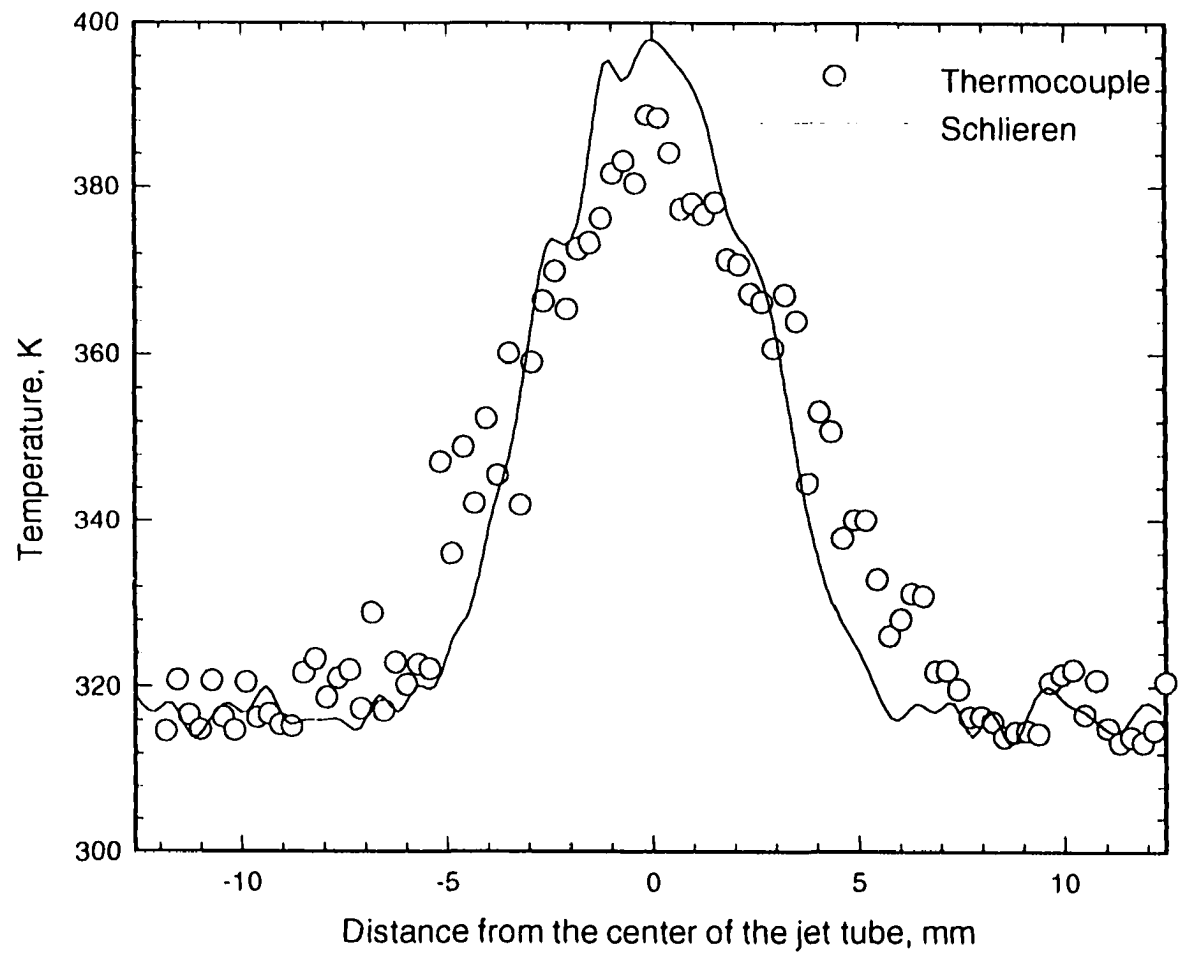


Figure 5.5 c Comparison of reconstruction from single schlieren image and thermocouple measurements at  $z = 15$  mm across x-axis

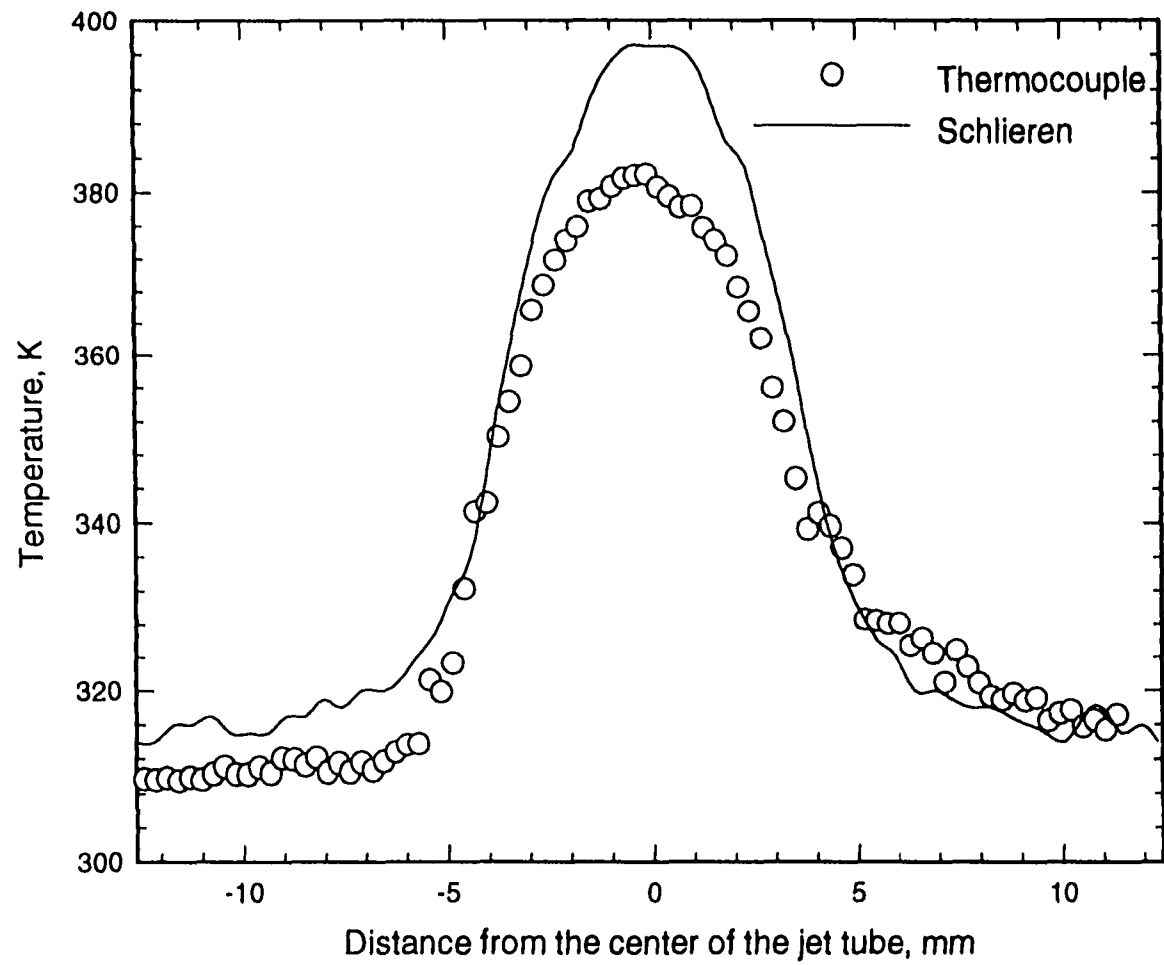


Figure 5.6a Reconstruction along the axis normal to light rays at  $z = 5\text{ mm}$ .

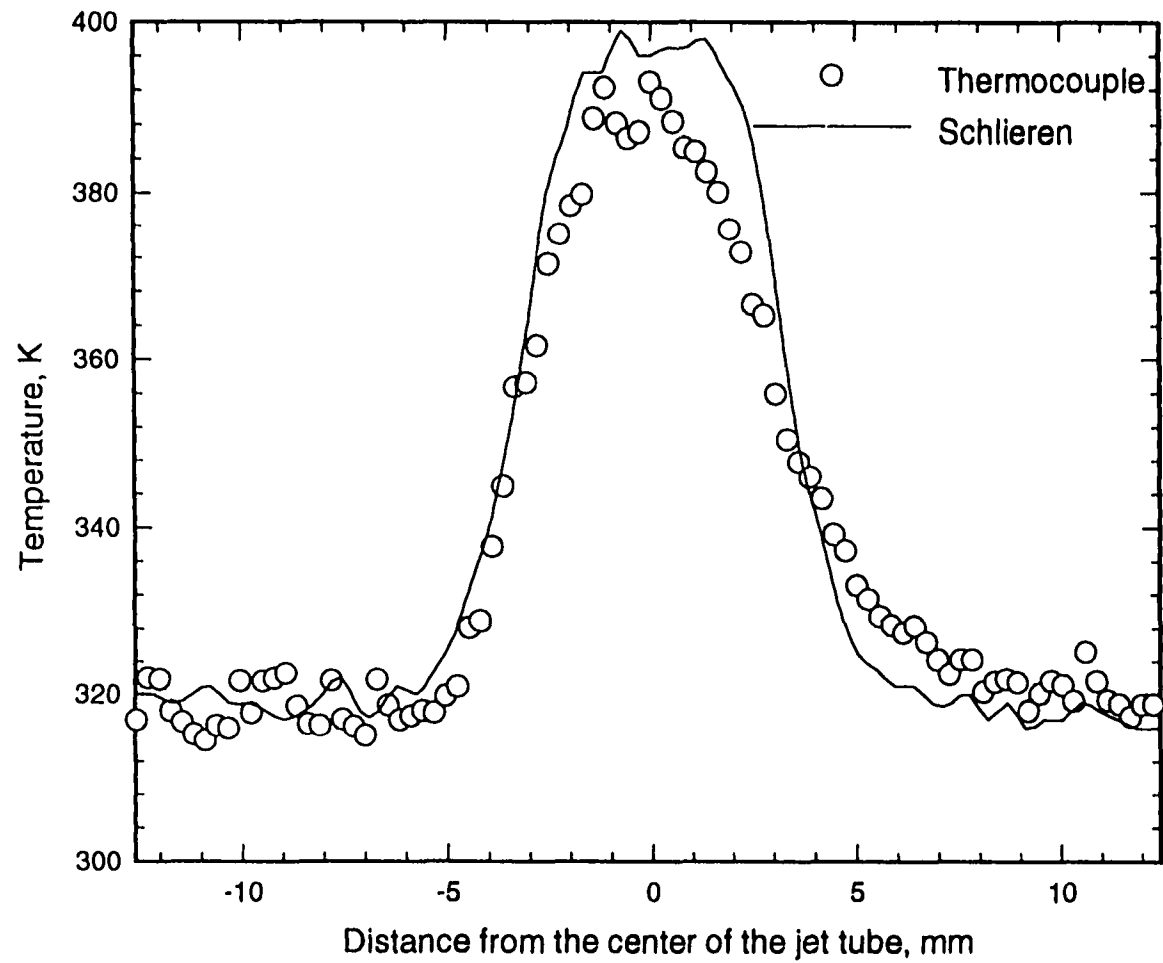


Figure 5.6b Reconstruction along the axis normal to light rays at  $z = 10$  mm

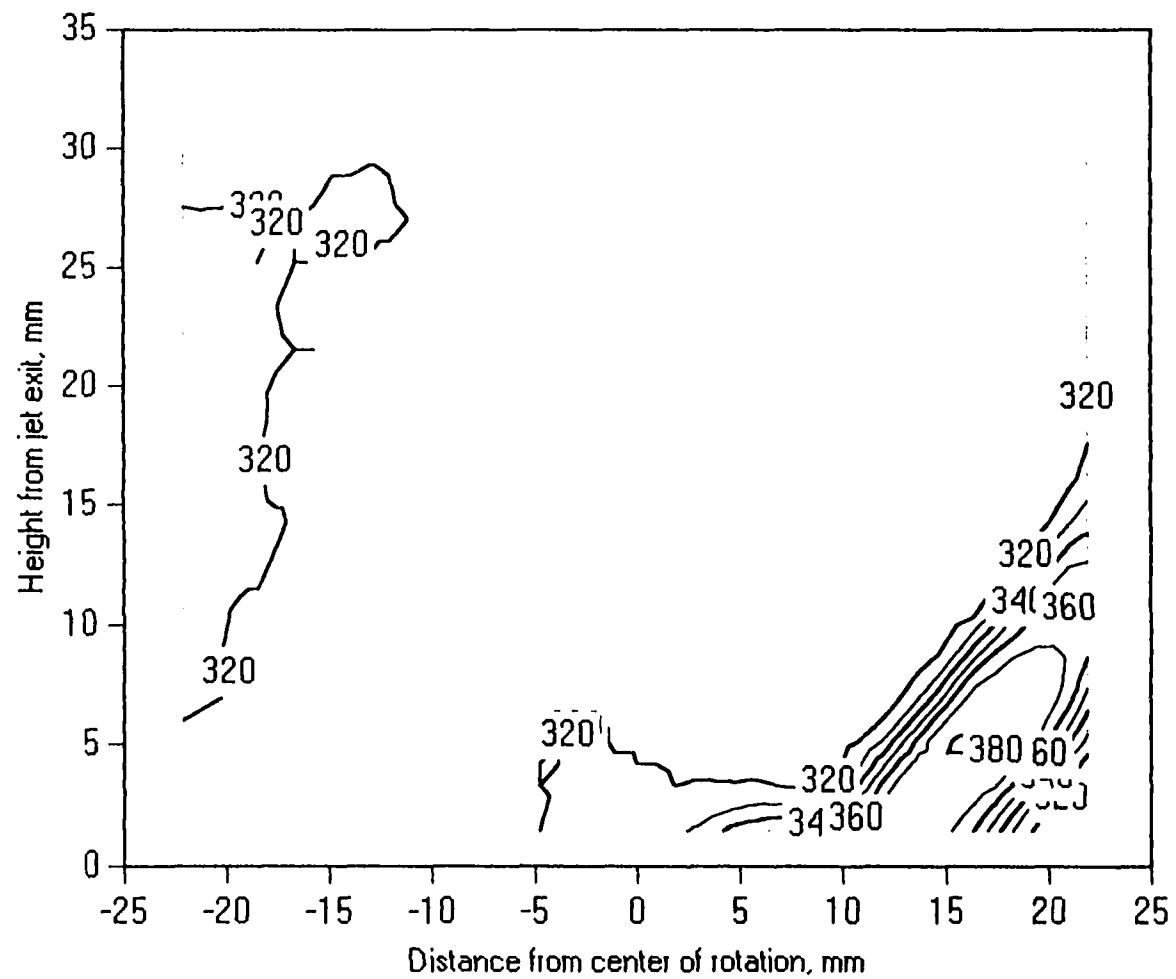


Figure 5.7 Contour plots within a vertical plane, parallel to the light rays at  $y = 3\text{mm}$ .

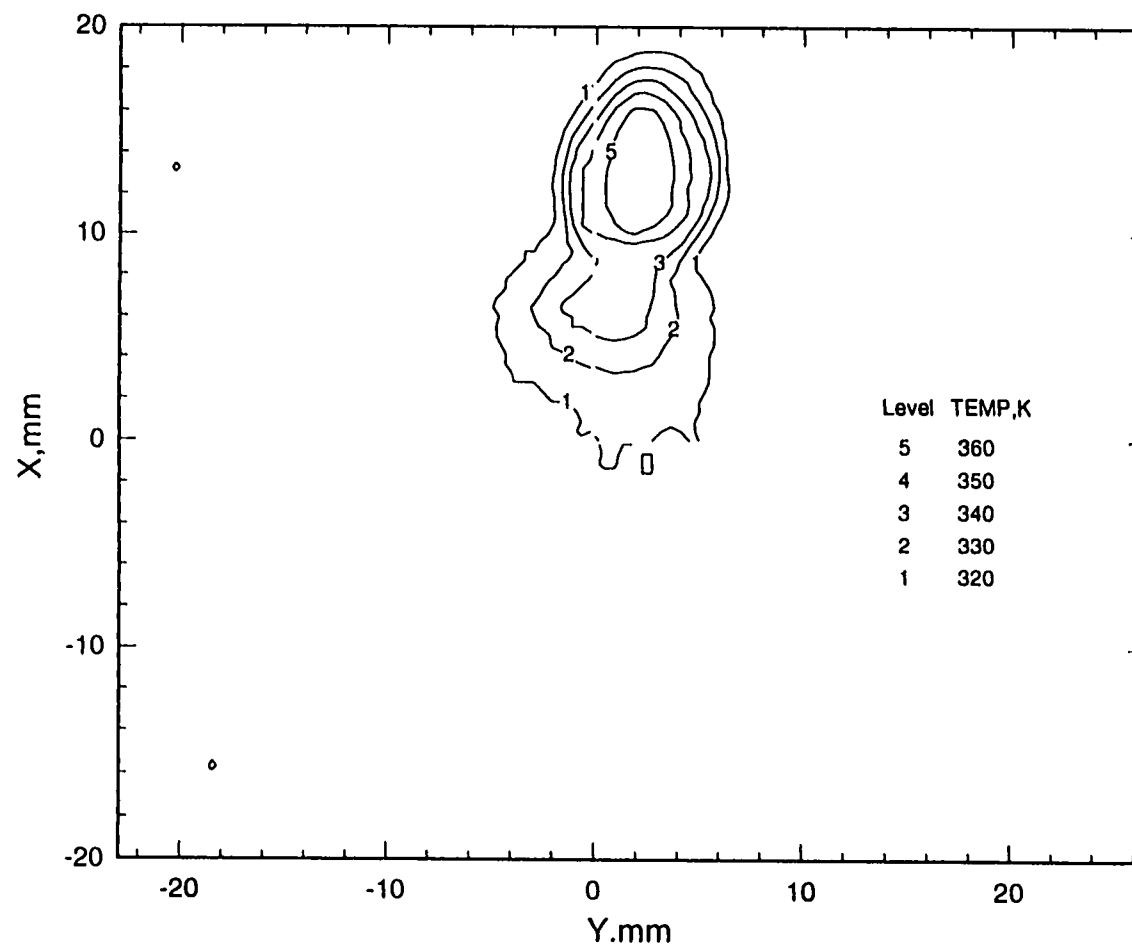


Figure 5.8 Contour plots at the horizontal axial plane through  $z = 5\text{mm}$



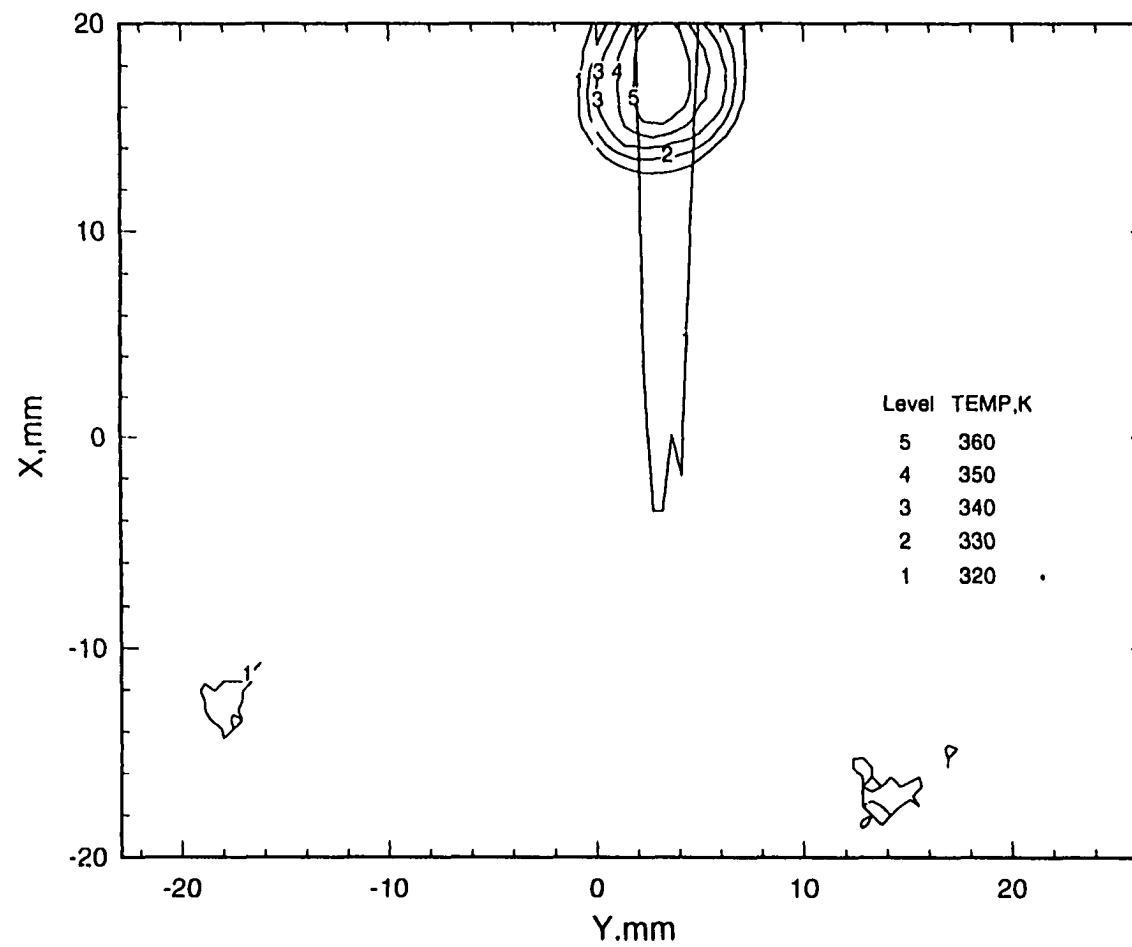


Figure 5.9 Contour plots at the horizontal axial plane through  $z = 10\text{mm}$

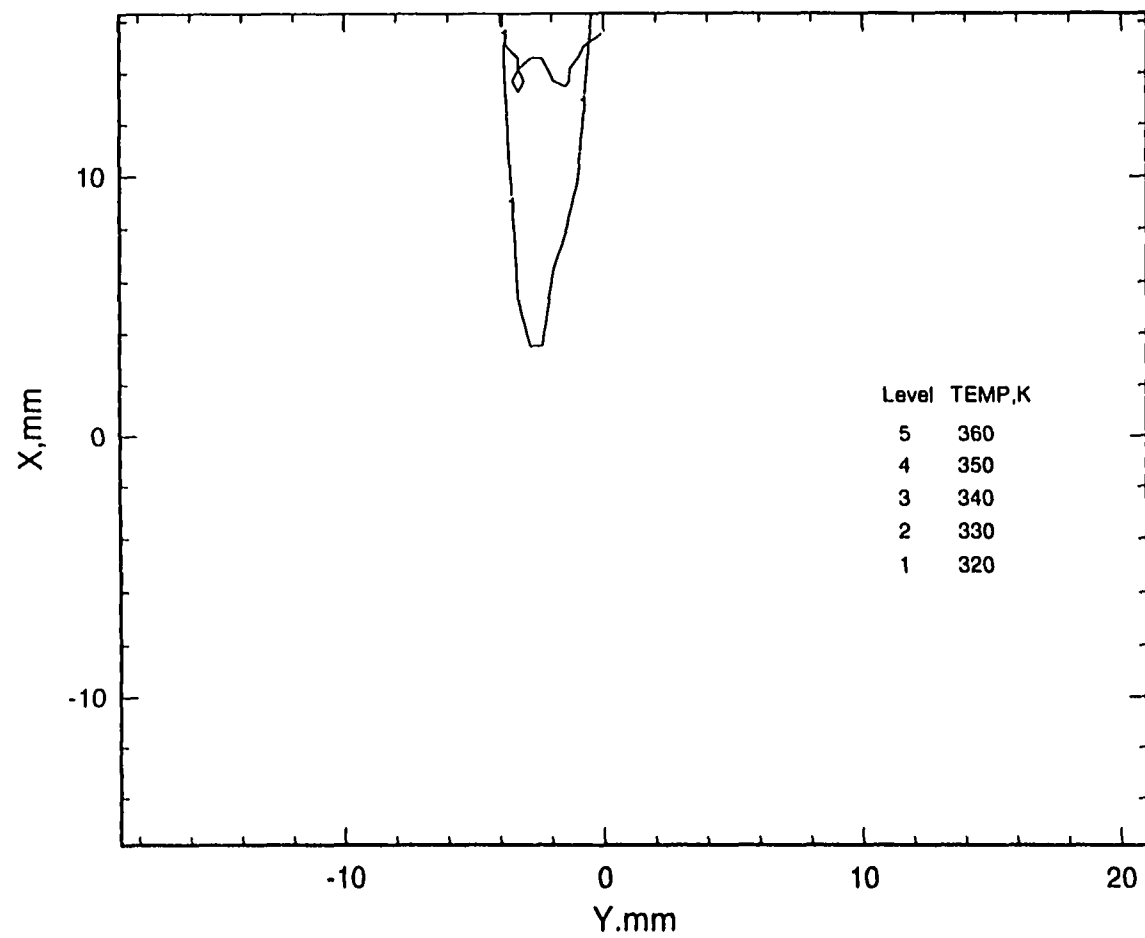


Figure 5.10 Contour plots at the horizontal axial plane through  $z = 15$  mm

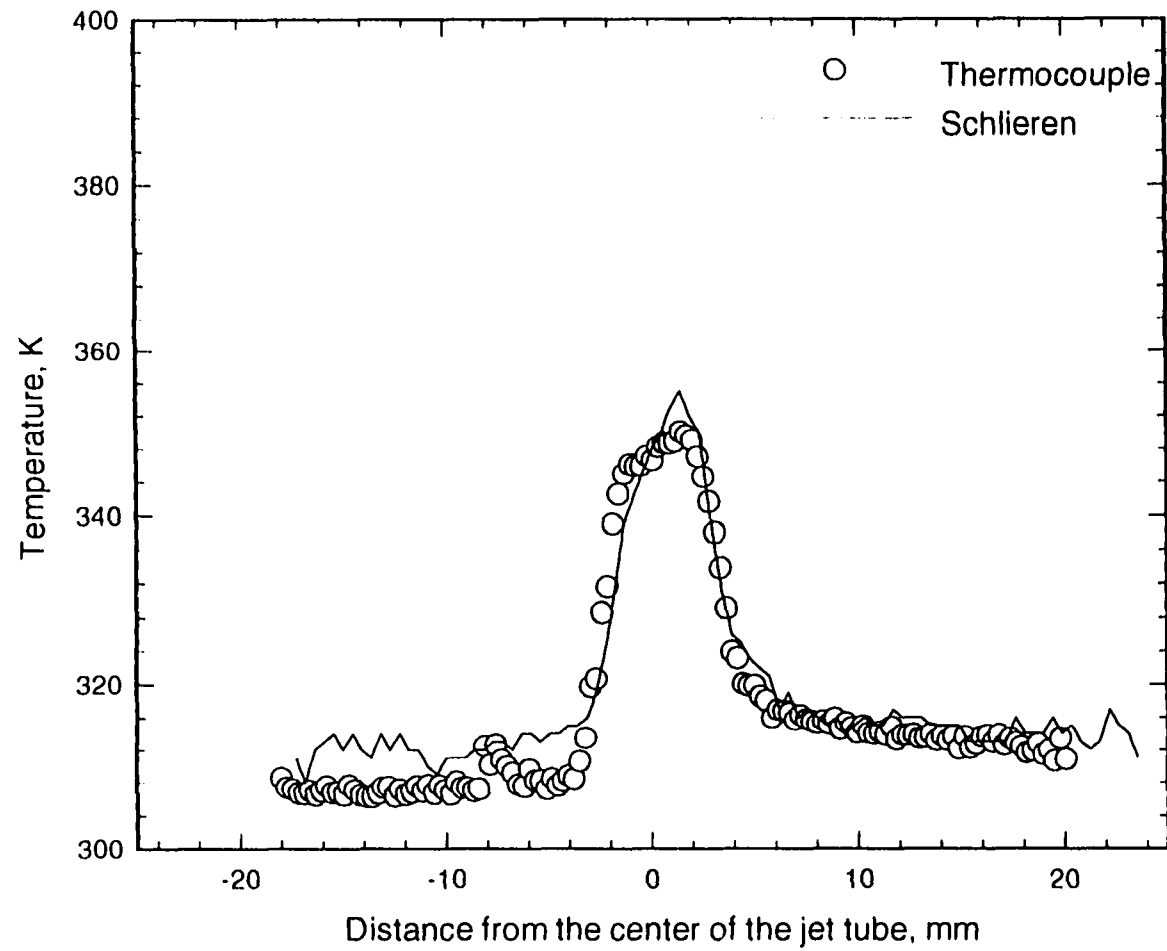


Figure 5.11 Comparisons of thermocouple measurements with schlieren reconstructions from the axial location  $z = 5\text{ mm}$  and line  $x = 12\text{ mm}$

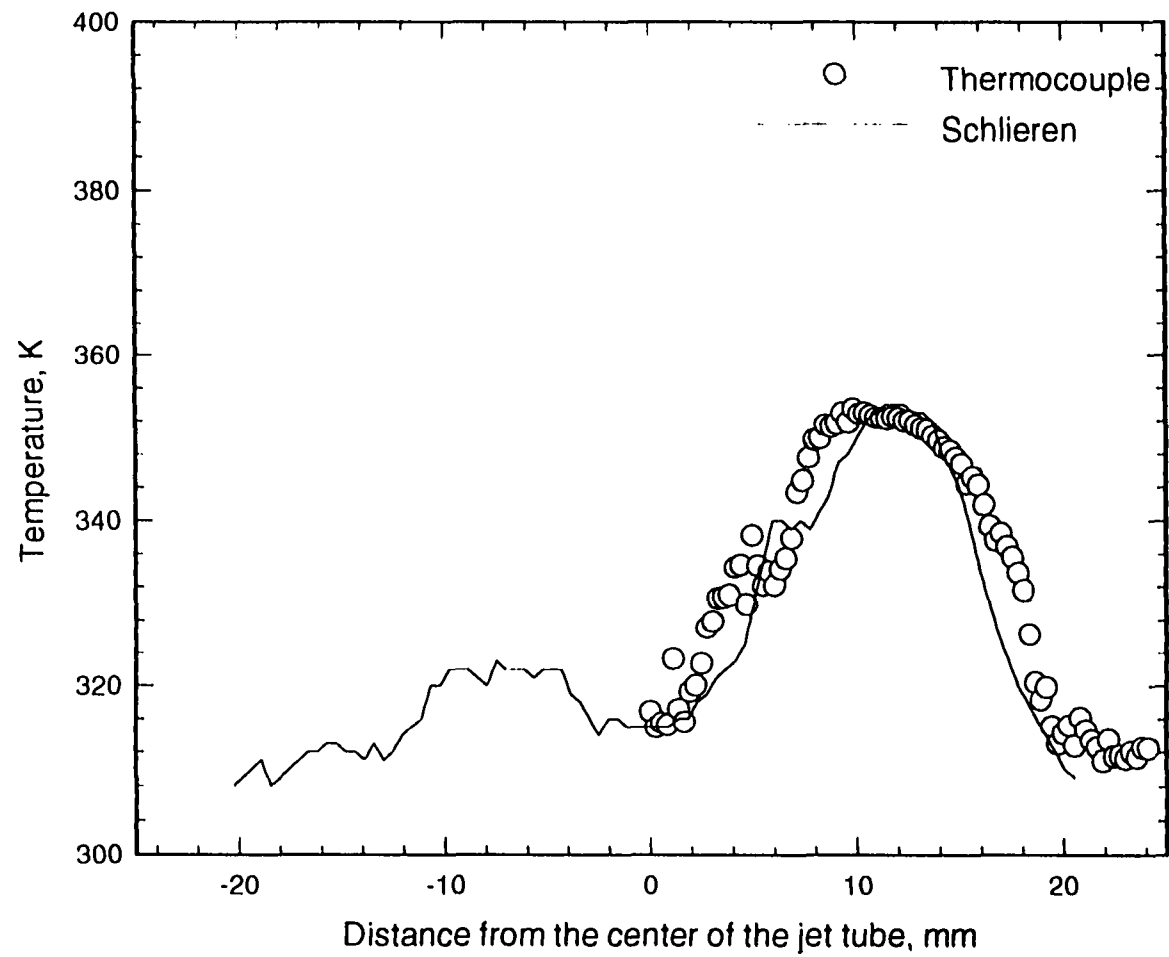


Figure 5.12 Comparisons of thermocouple measurements with schlieren reconstructions from the axial location  $z = 5\text{mm}$  and line  $y = 0$

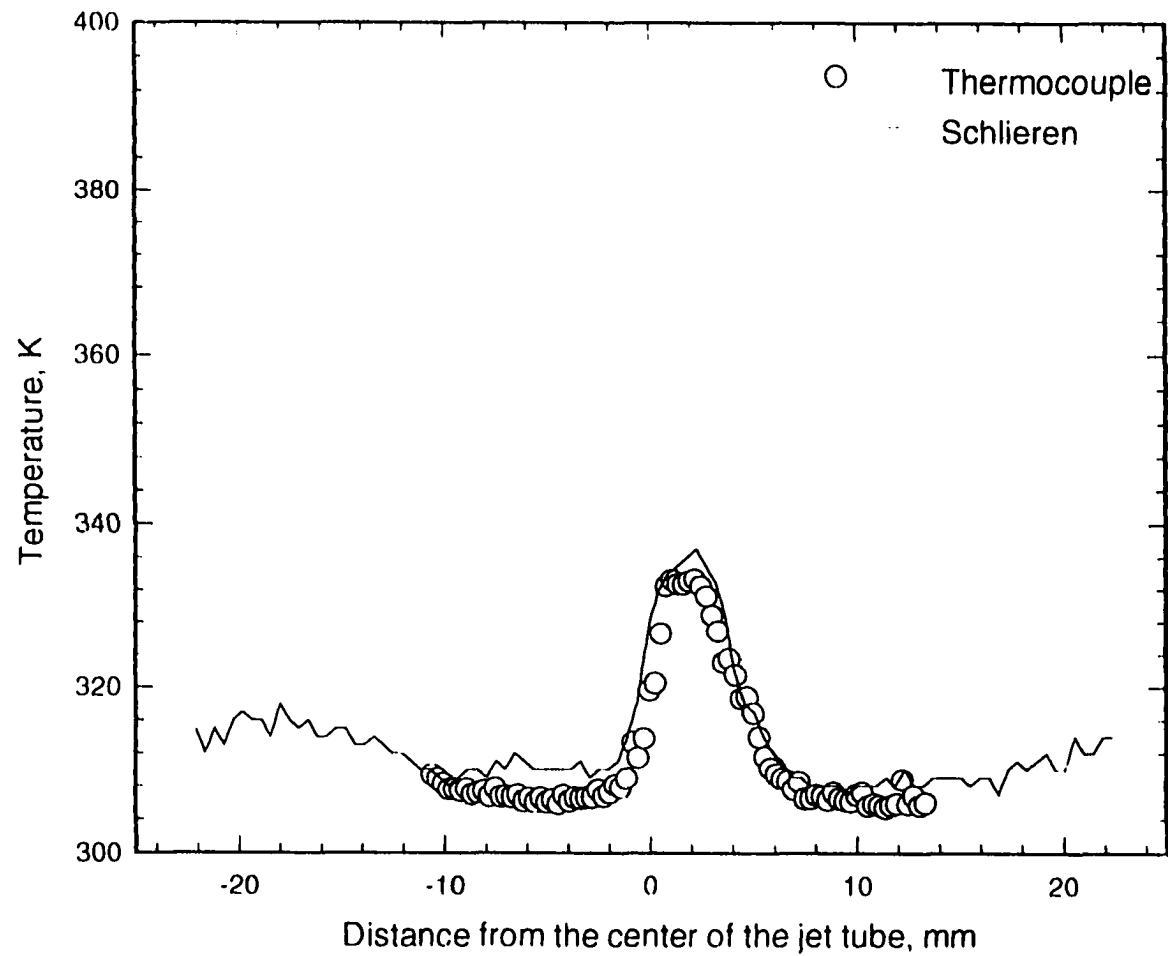


Figure 5.13 Comparison of thermocouple measurements with schlieren reconstructions from the axial location  $z = 10$  and line  $x = 15$

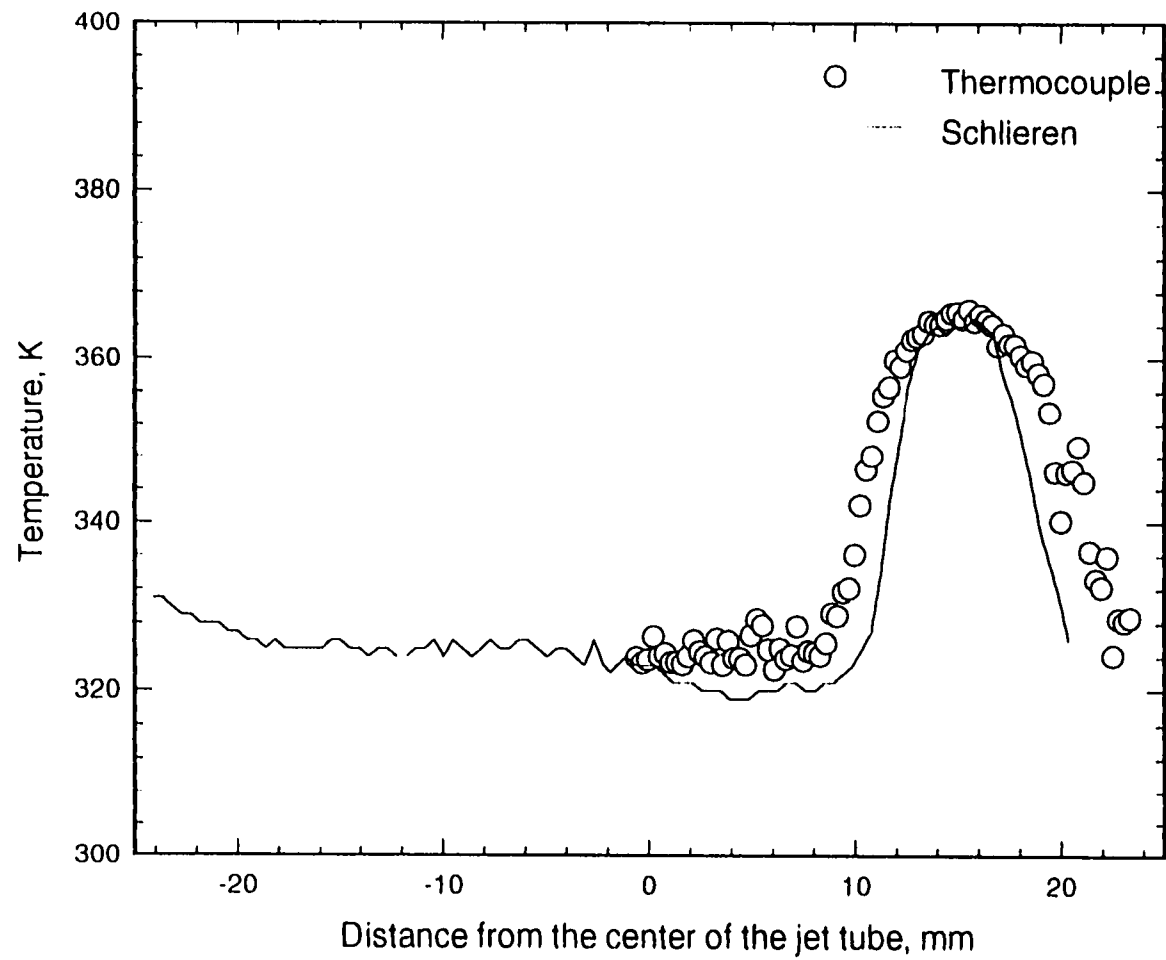


Figure 5.14 Comparison of thermocouple measurements with schlieren reconstructions from the axial location  $z = 10\text{mm}$ , and line  $y = 0$

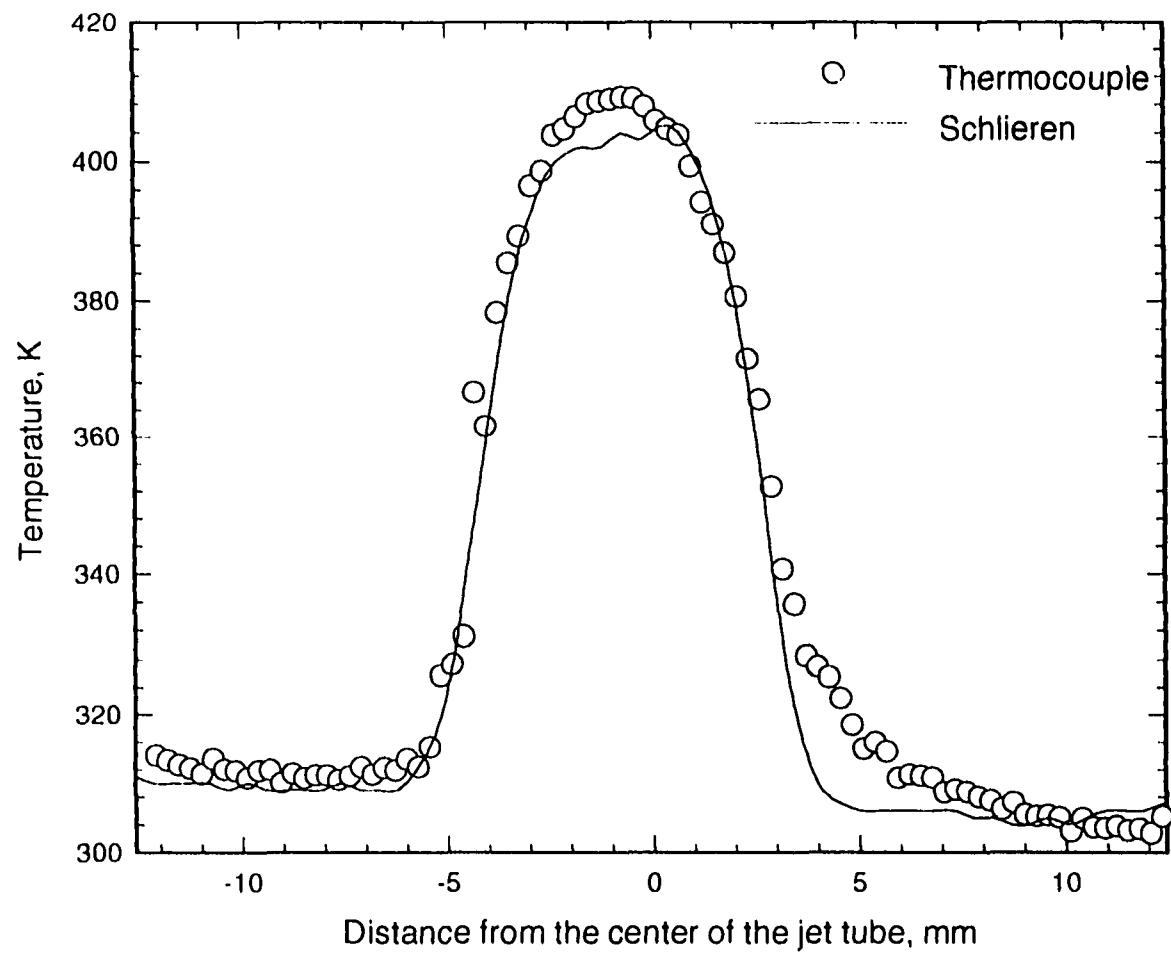


Figure 5.15a Comparison of thermocouple measurements with schlieren reconstructions for axial location  $z = 5$  mm, major axis reconstruction.

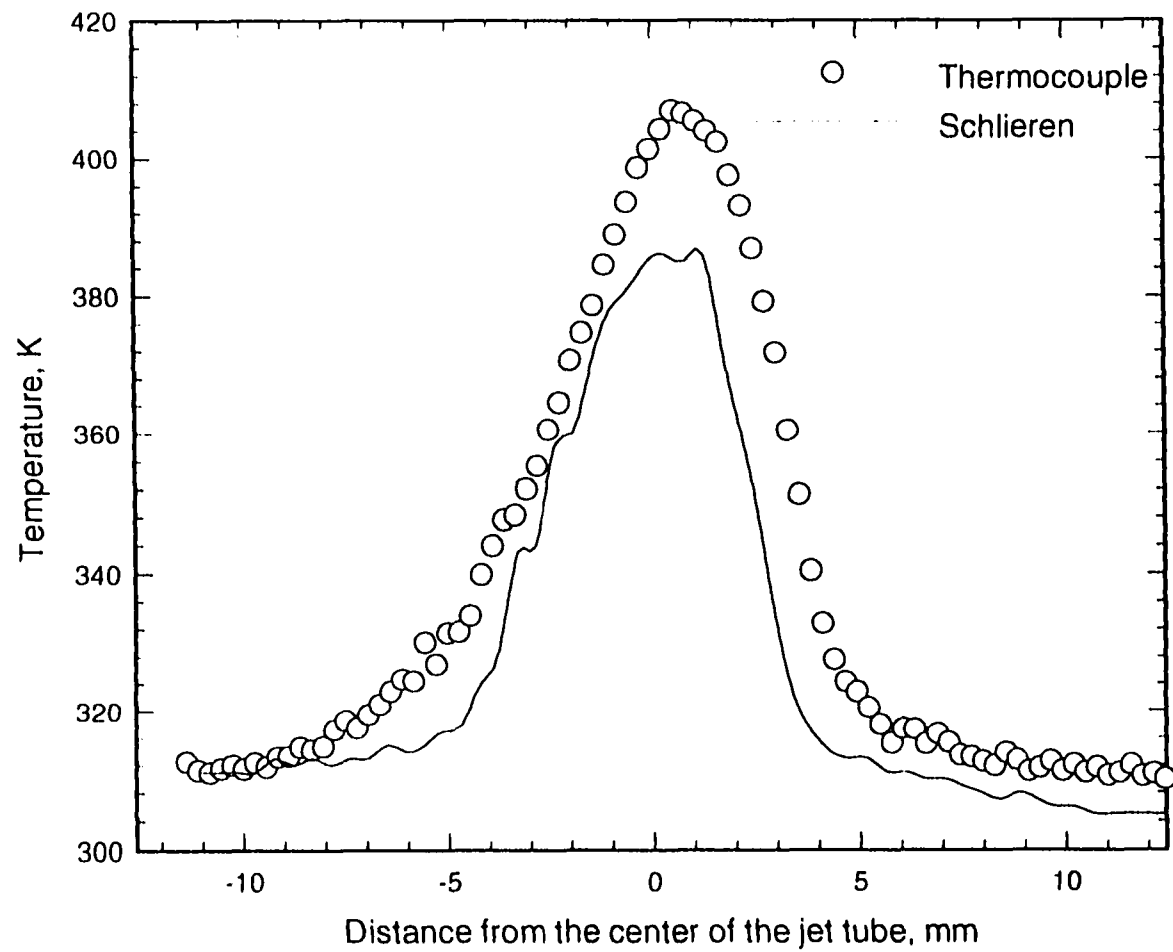


Figure 5.15b Comparison of thermocouple measurements with schlieren reconstructions for axial location  $z = 5\text{ mm}$ , minor axis



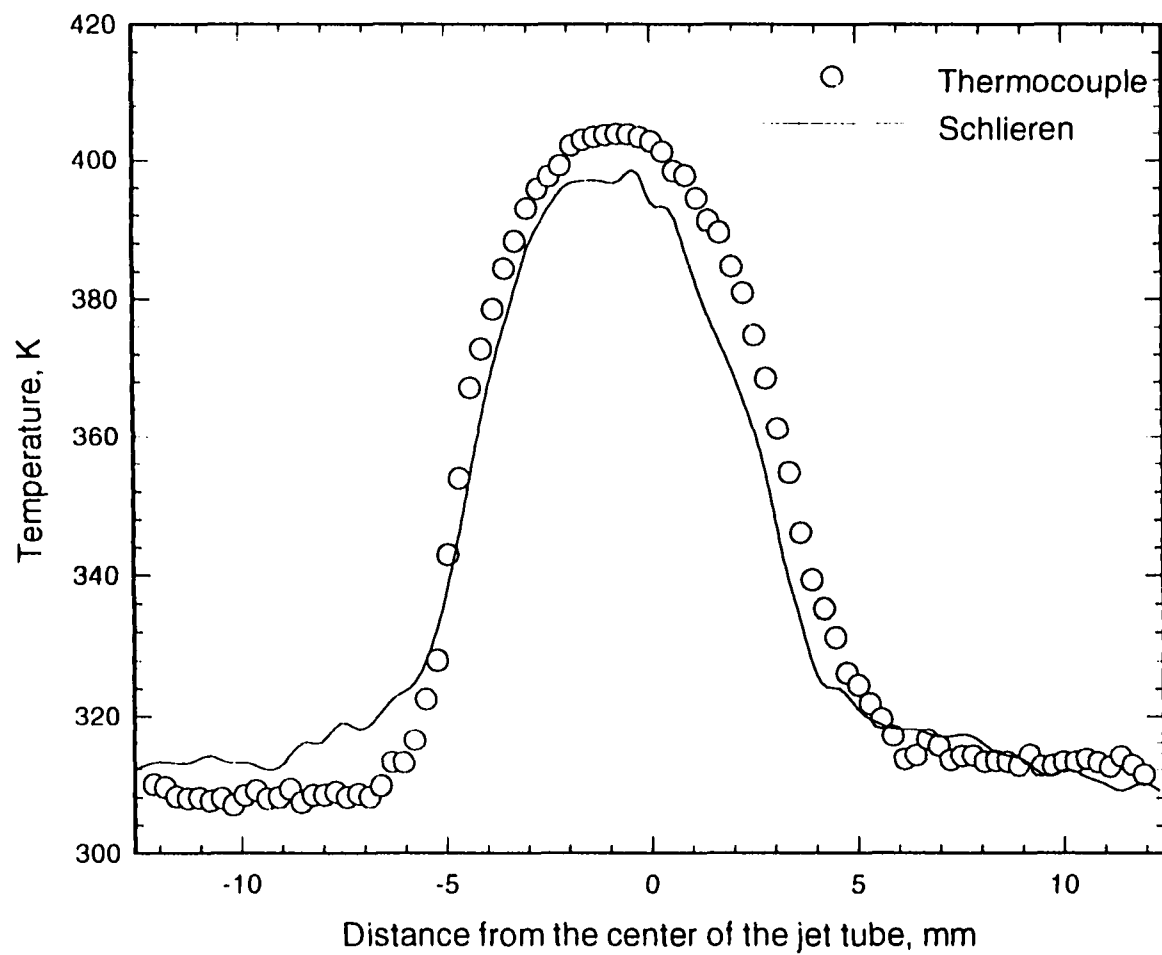


Figure 5.16a Comparisons of thermocouple measurements with schlieren reconstructions for axial location  $z = 10$  mm, major axis

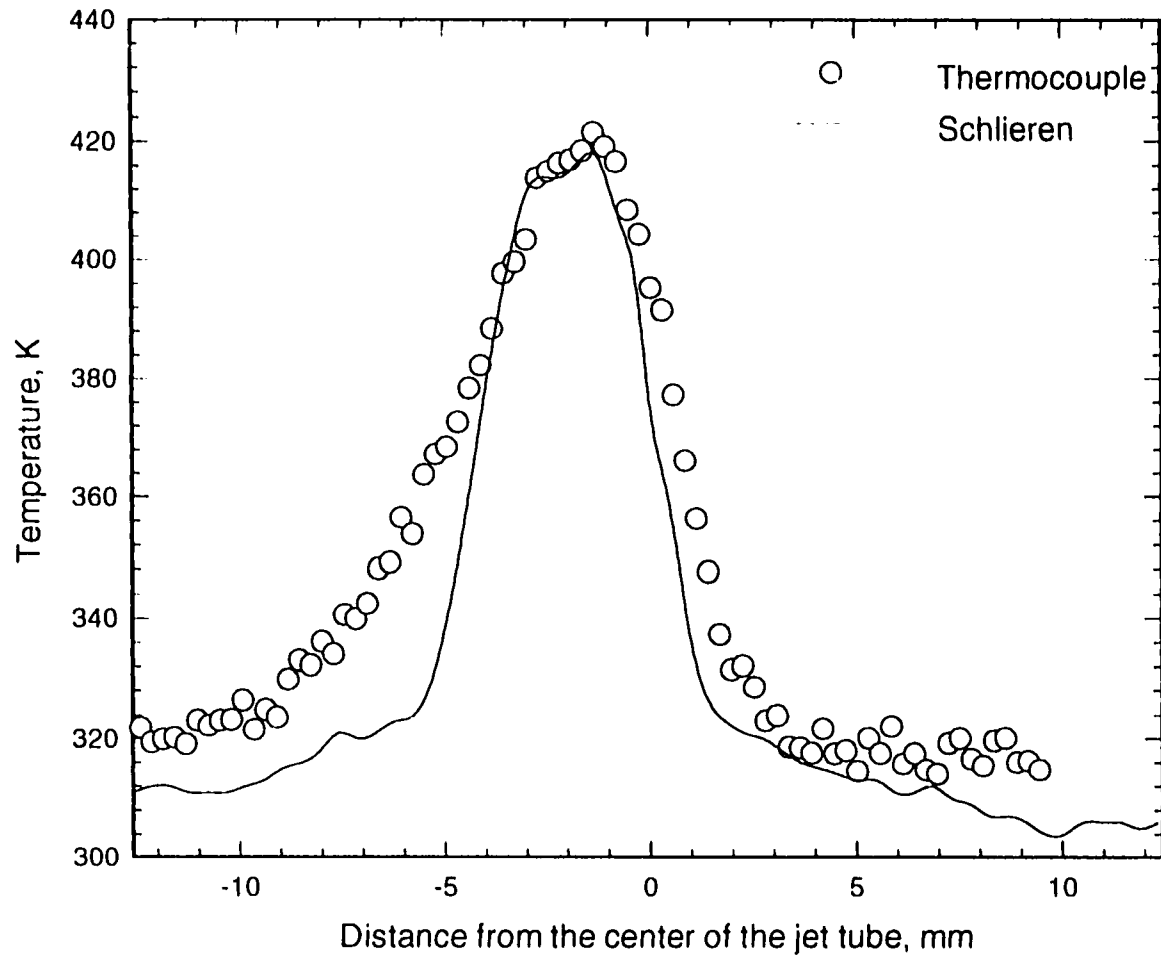


Figure 5.16b Comparison of thermocouple measurements with schlieren reconstructions for axial location  $z = 10$  mm, minor axis

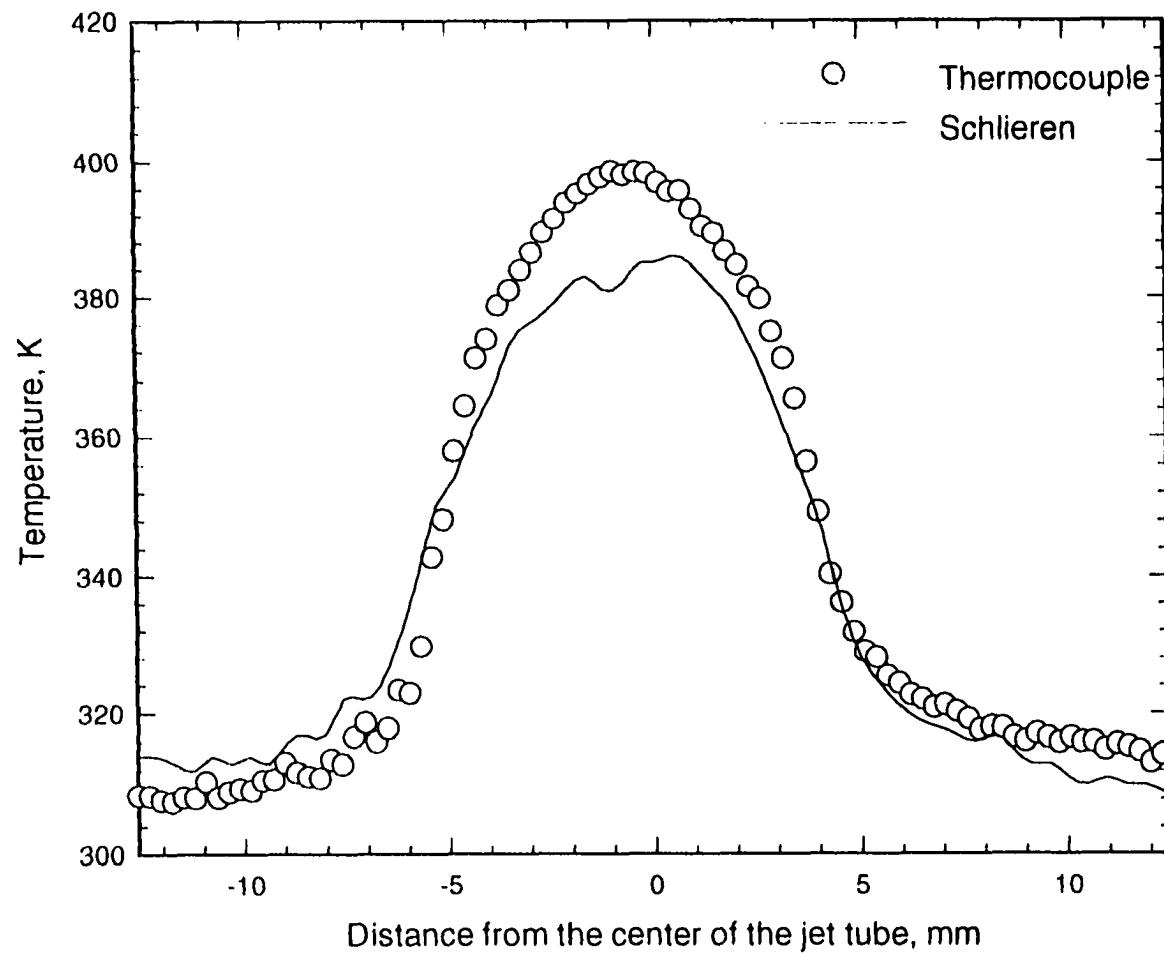


Figure 5.17a Comparison of thermocouple measurements with schlieren reconstructions for axial location  $z = 15\text{ mm}$ , major axis

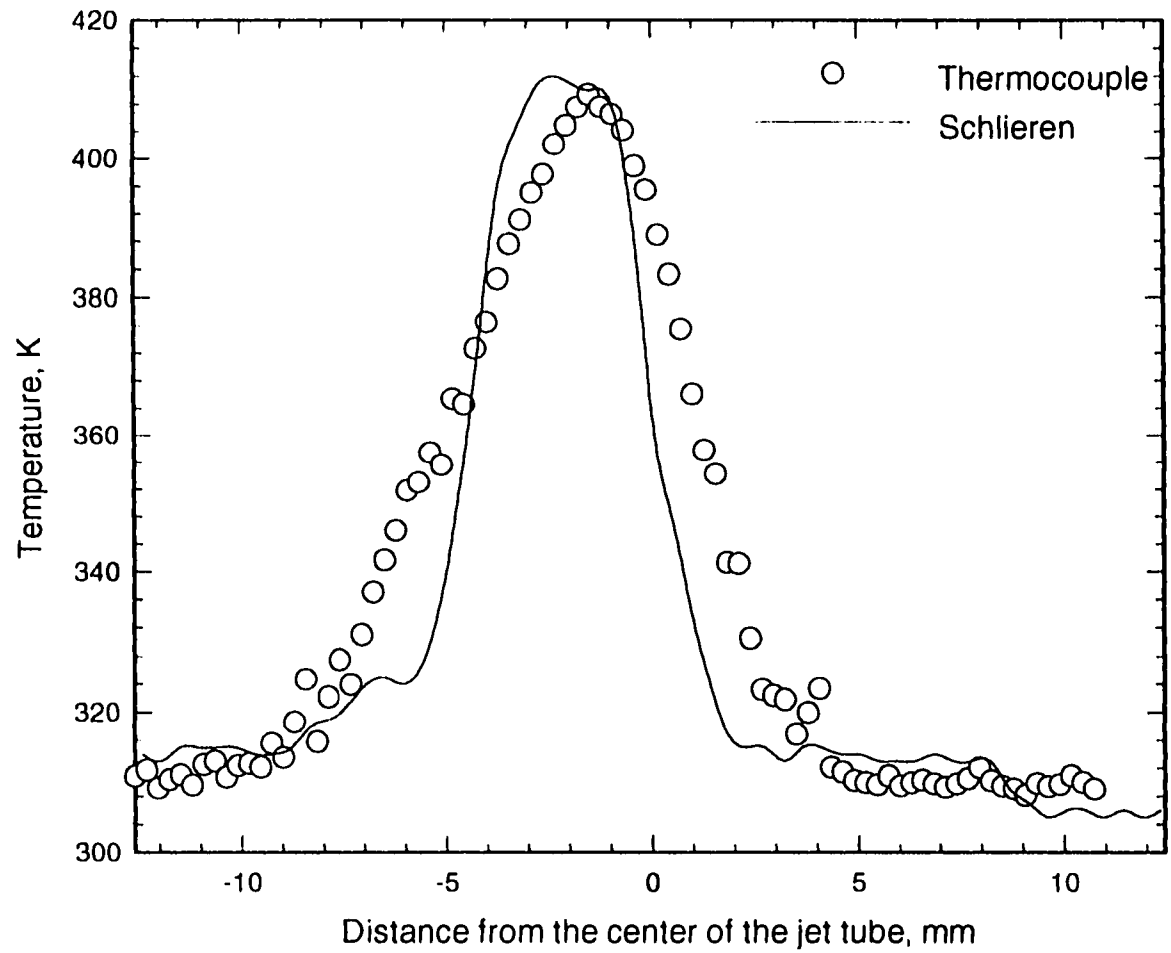


Figure 5.17b Comparison of thermocouple measurements with schlieren reconstructions for axial location  $z = 15$  mm minor axis.

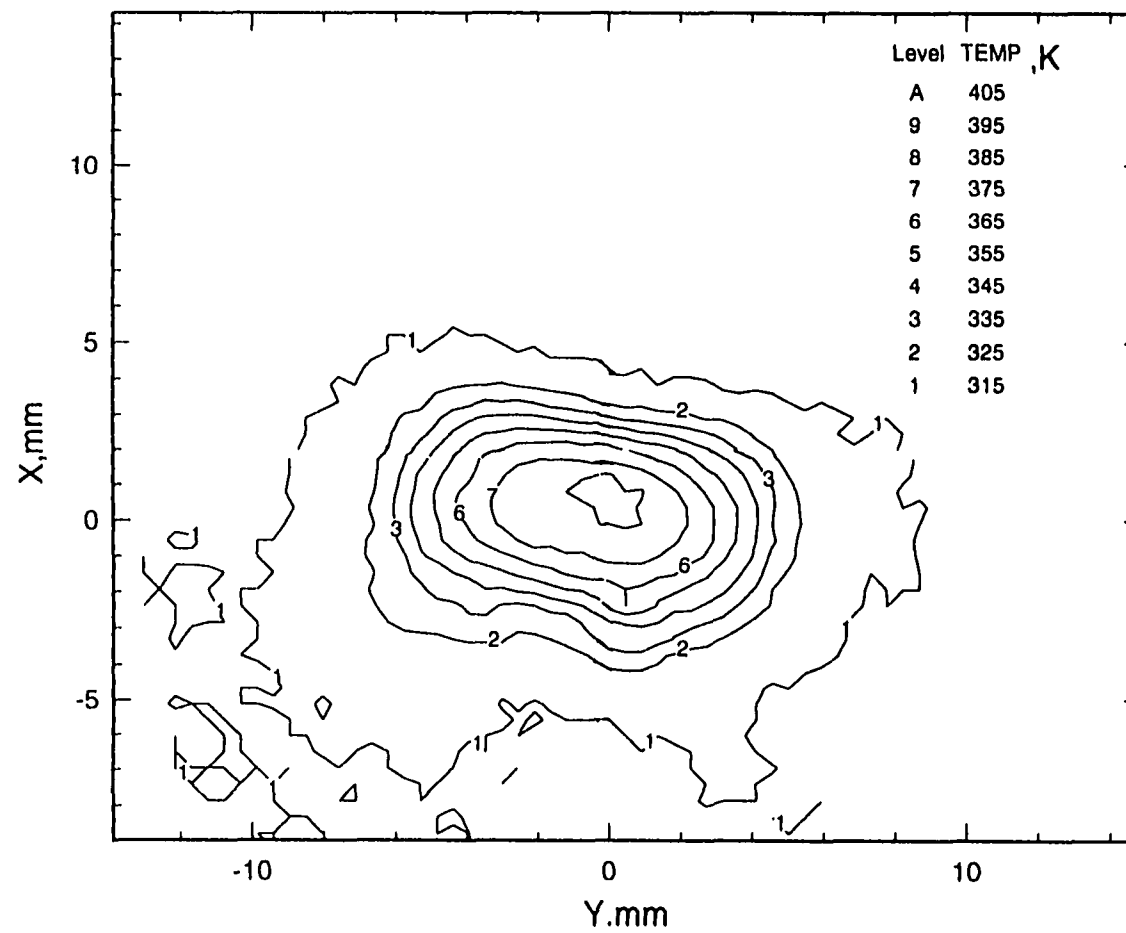


Figure5.18a Contour plots at axial plane through  $z = 5$  mm

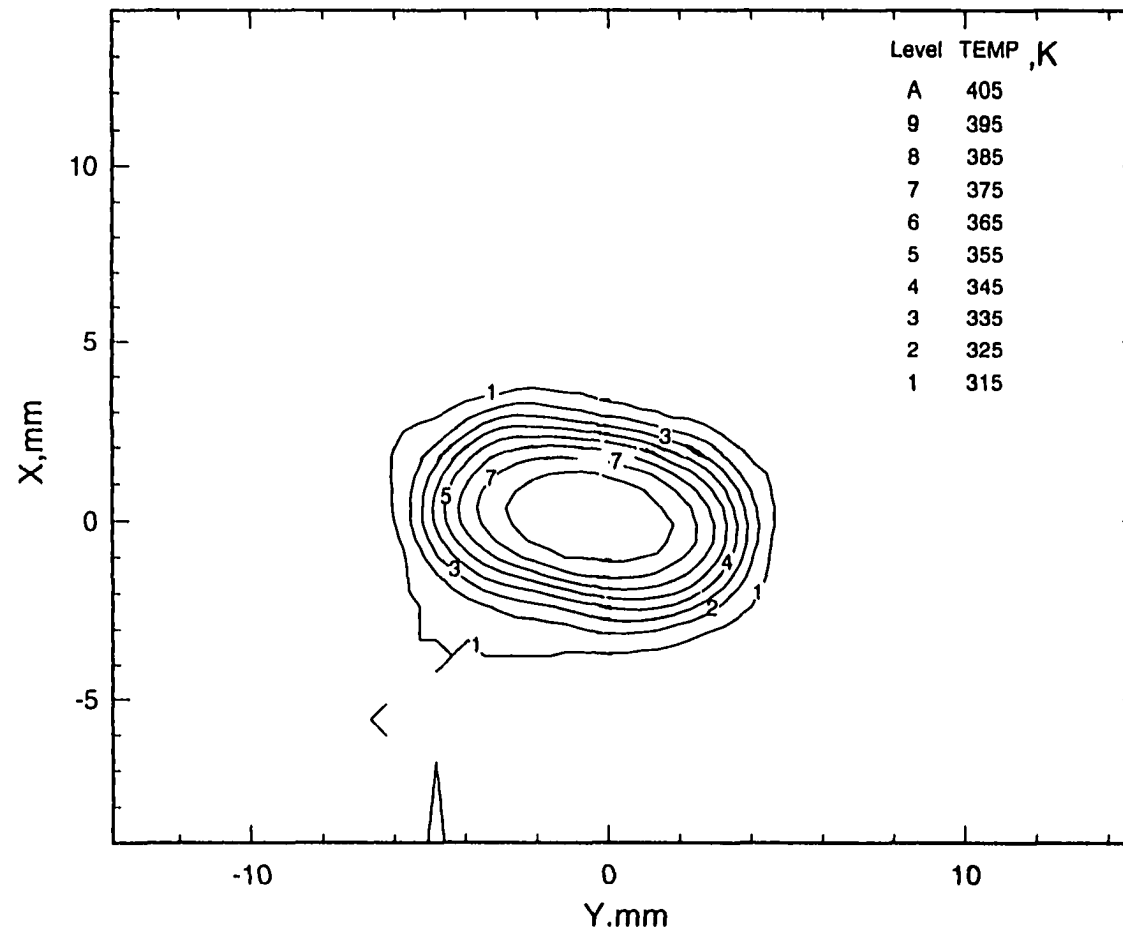


Figure5.18b Contour plots at axial plane through  $z = 10\text{mm}$

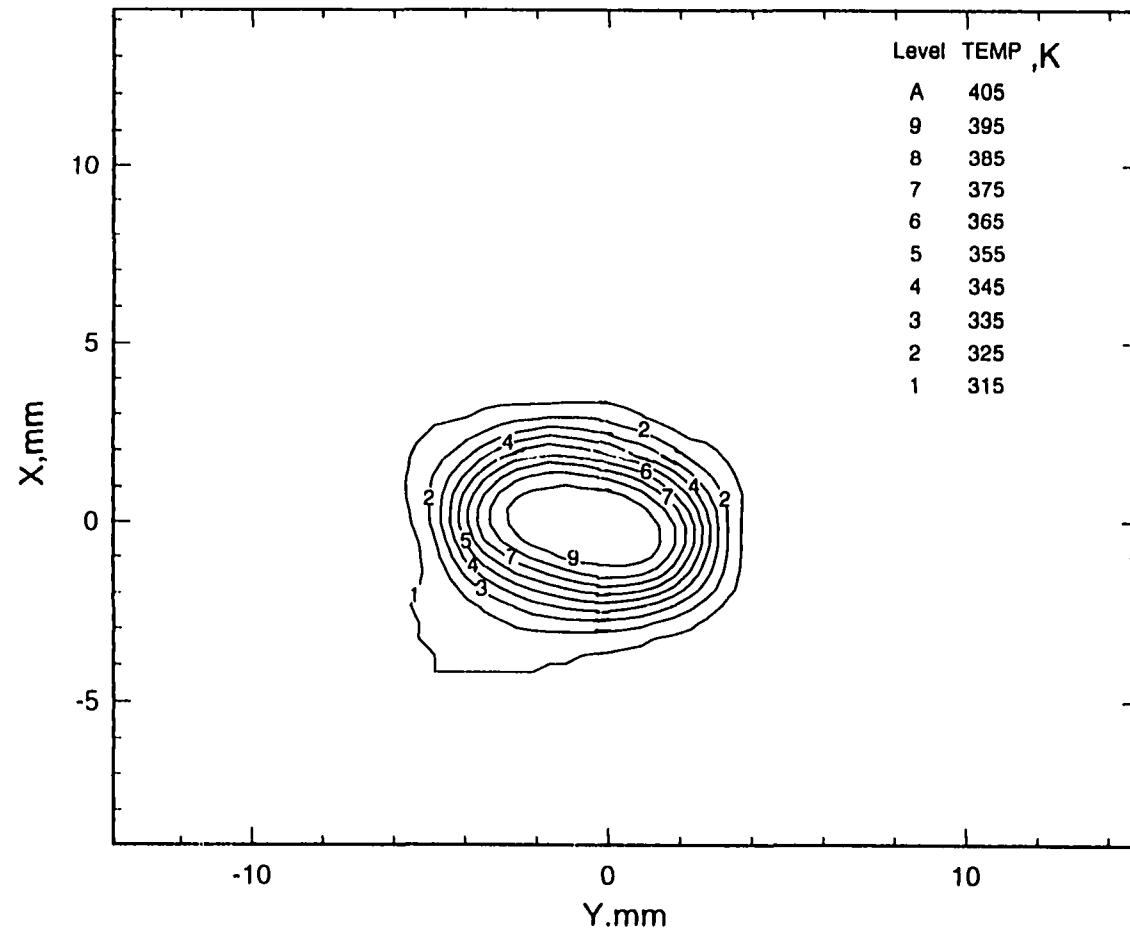


Figure5.18c Contour plots at axial plane  $z=15\text{mm}$

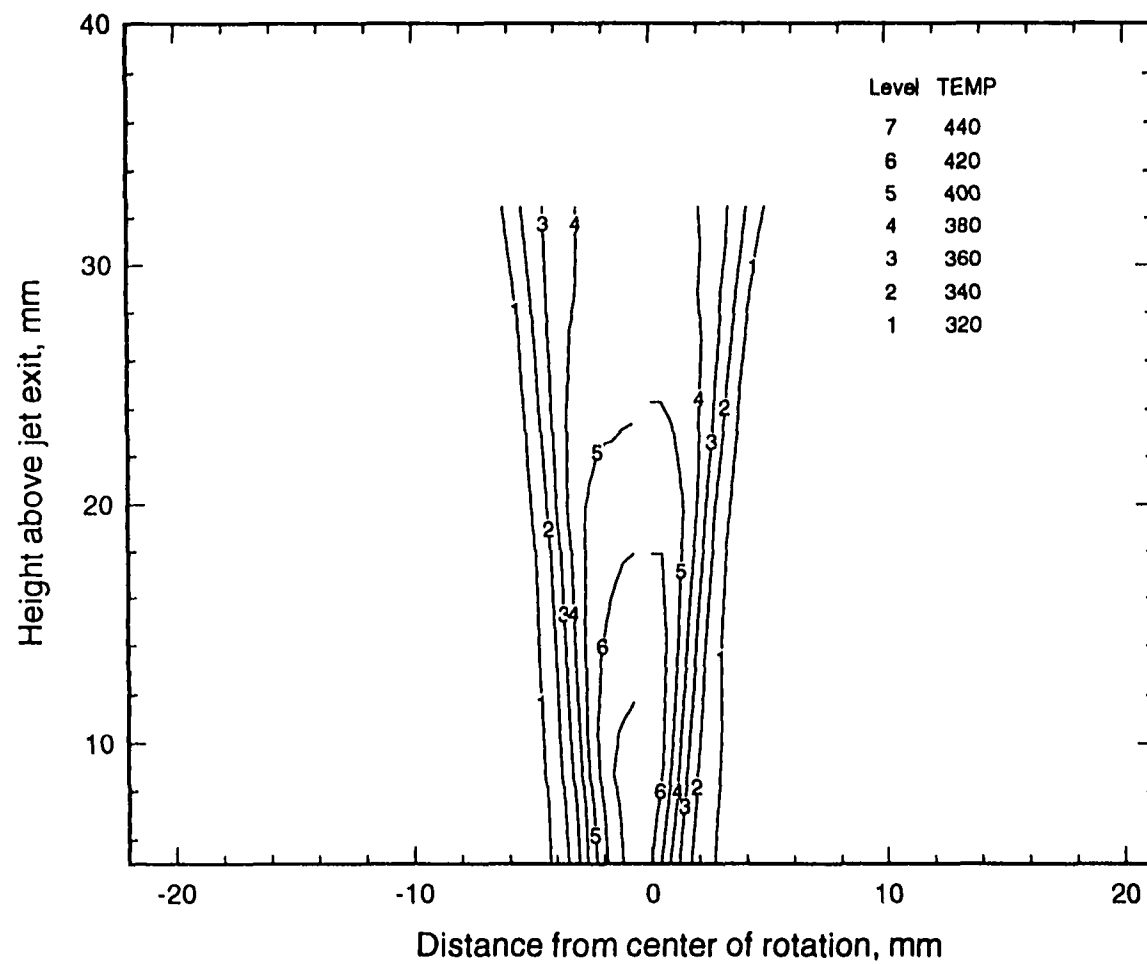


Figure5.19a Contours in vertical plane parallel to the major axis, at the center of the jet



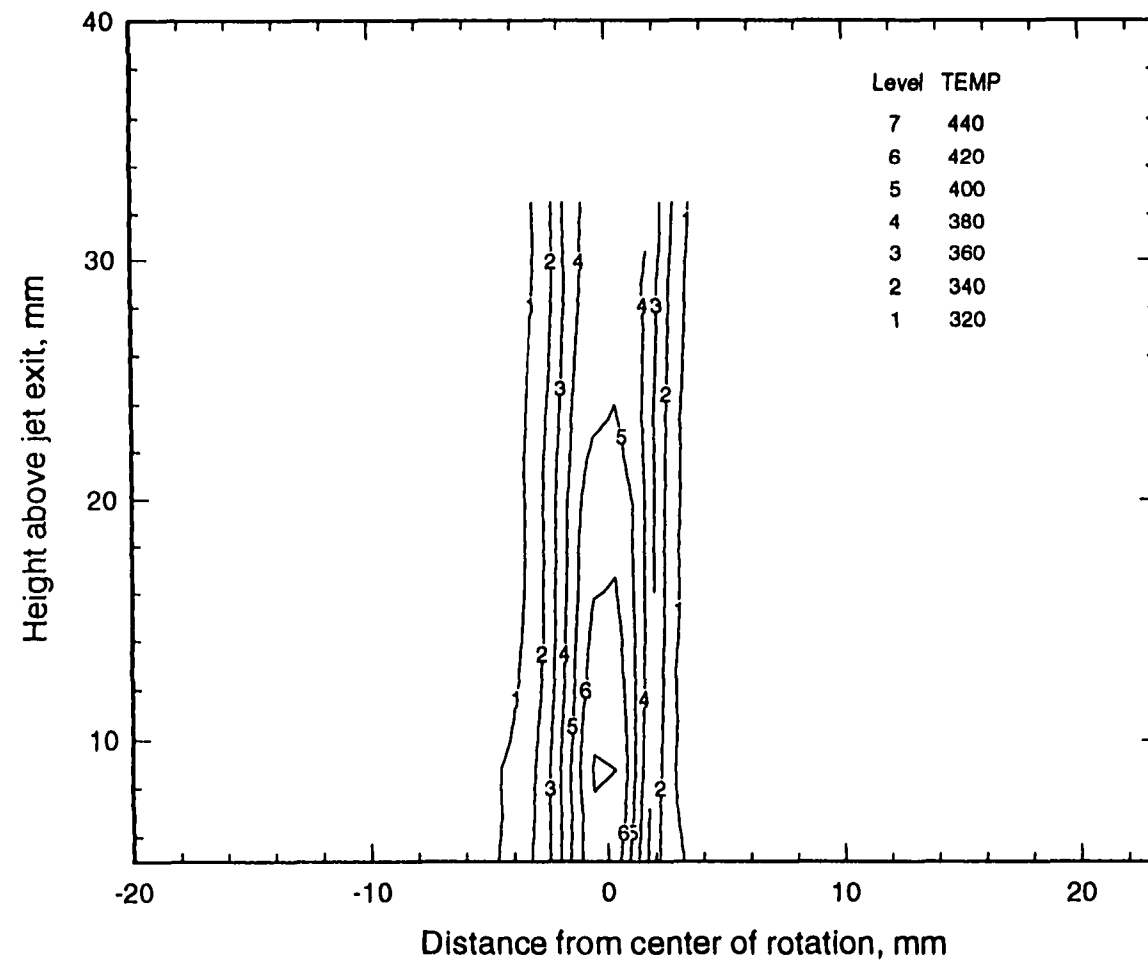


Figure5.19b Contour in vertical plane parallel to the minor axis, at the center of the jet.

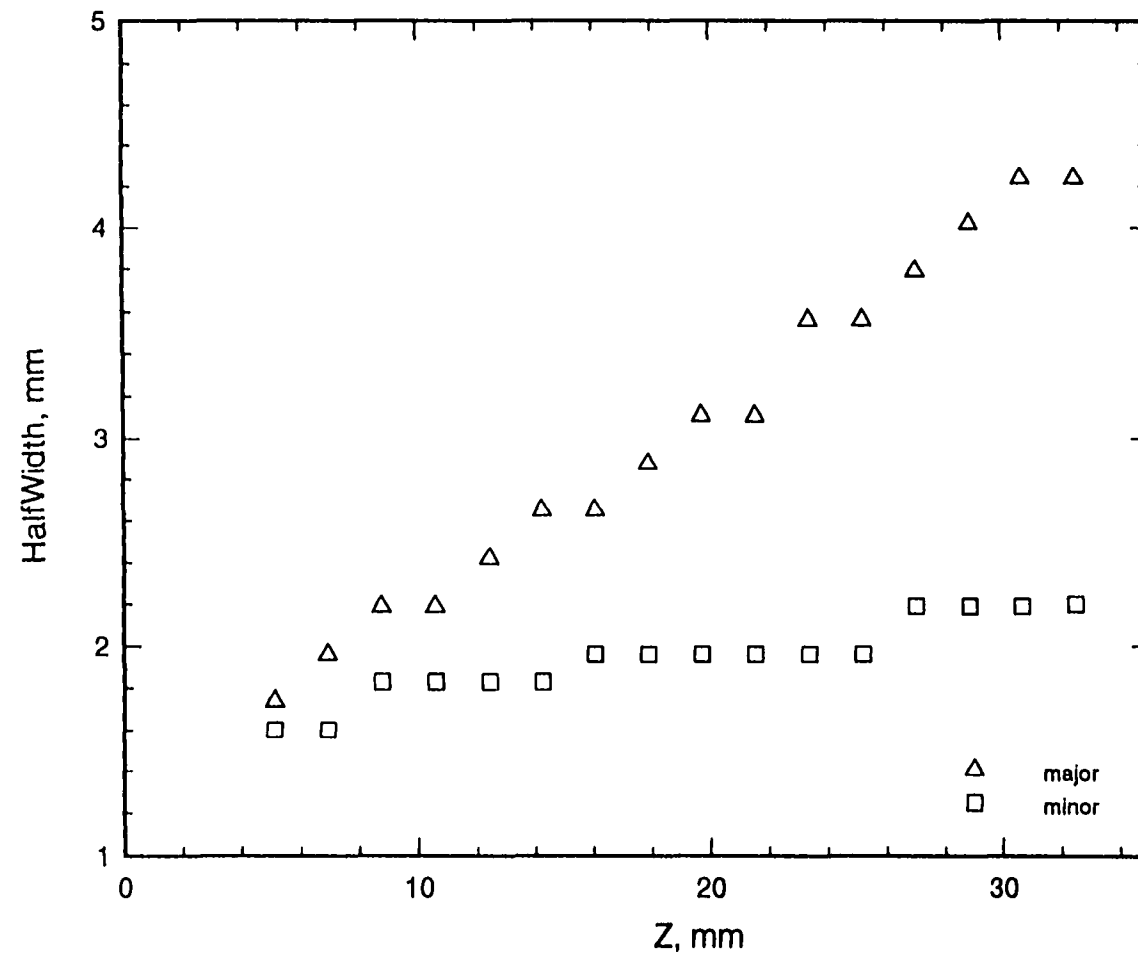


Figure5.20a Plot of jet half-widths for both minor and major axis

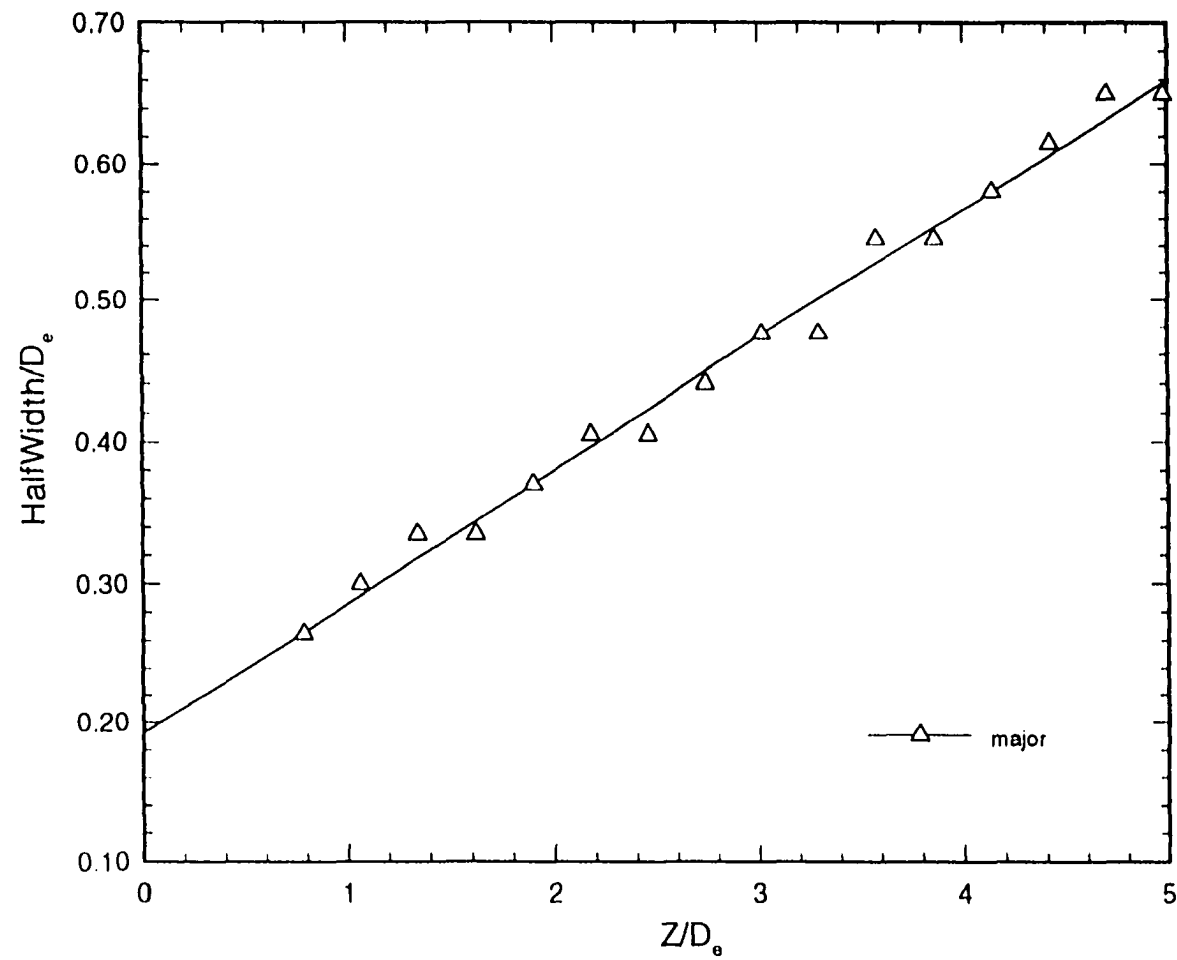


Figure5.20b Plot of non-dimensionalized jet half-width for major axis

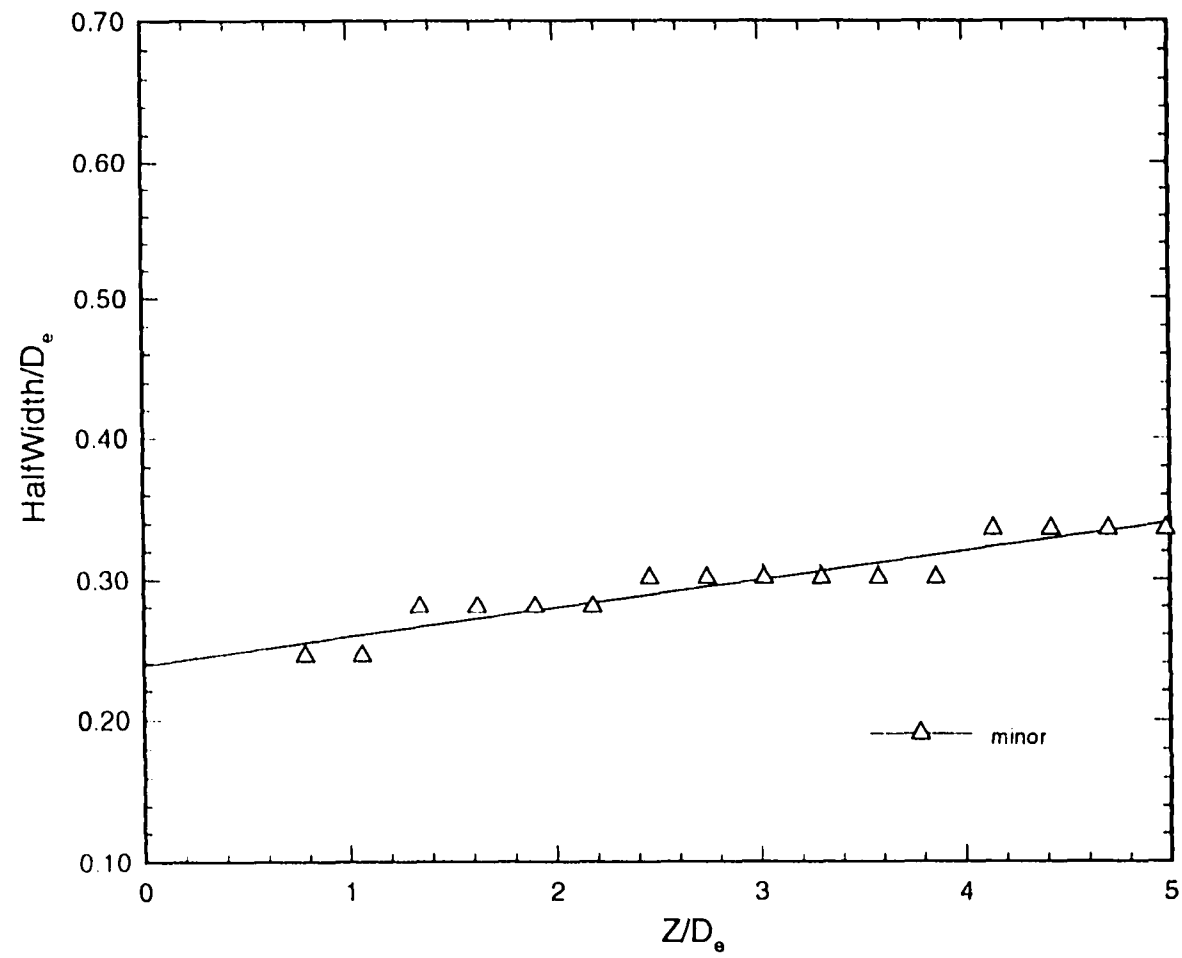


Figure5.20c Plot of non-dimensionalized jet half-width for minor axis

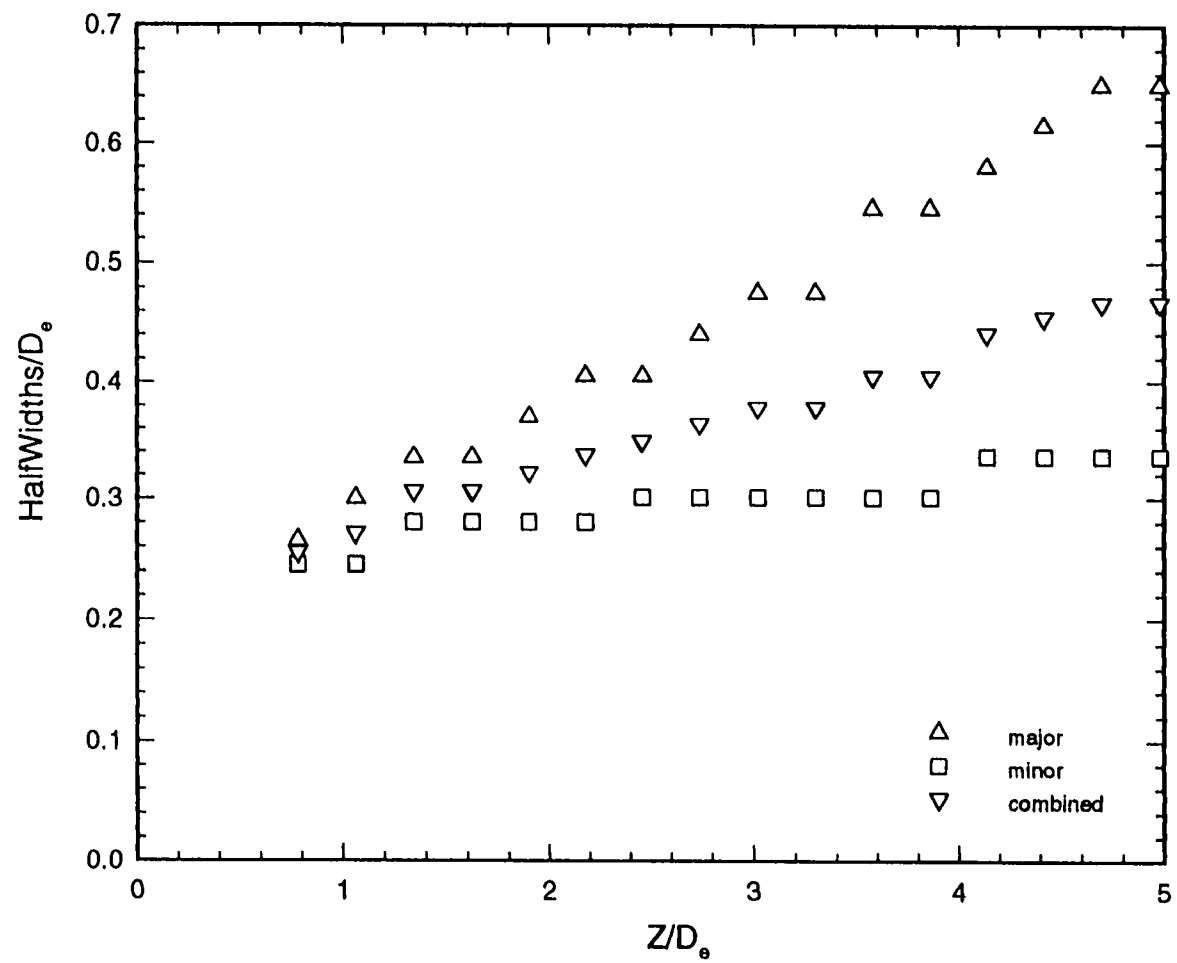


Figure5.21 Comparison of jet half-widths.

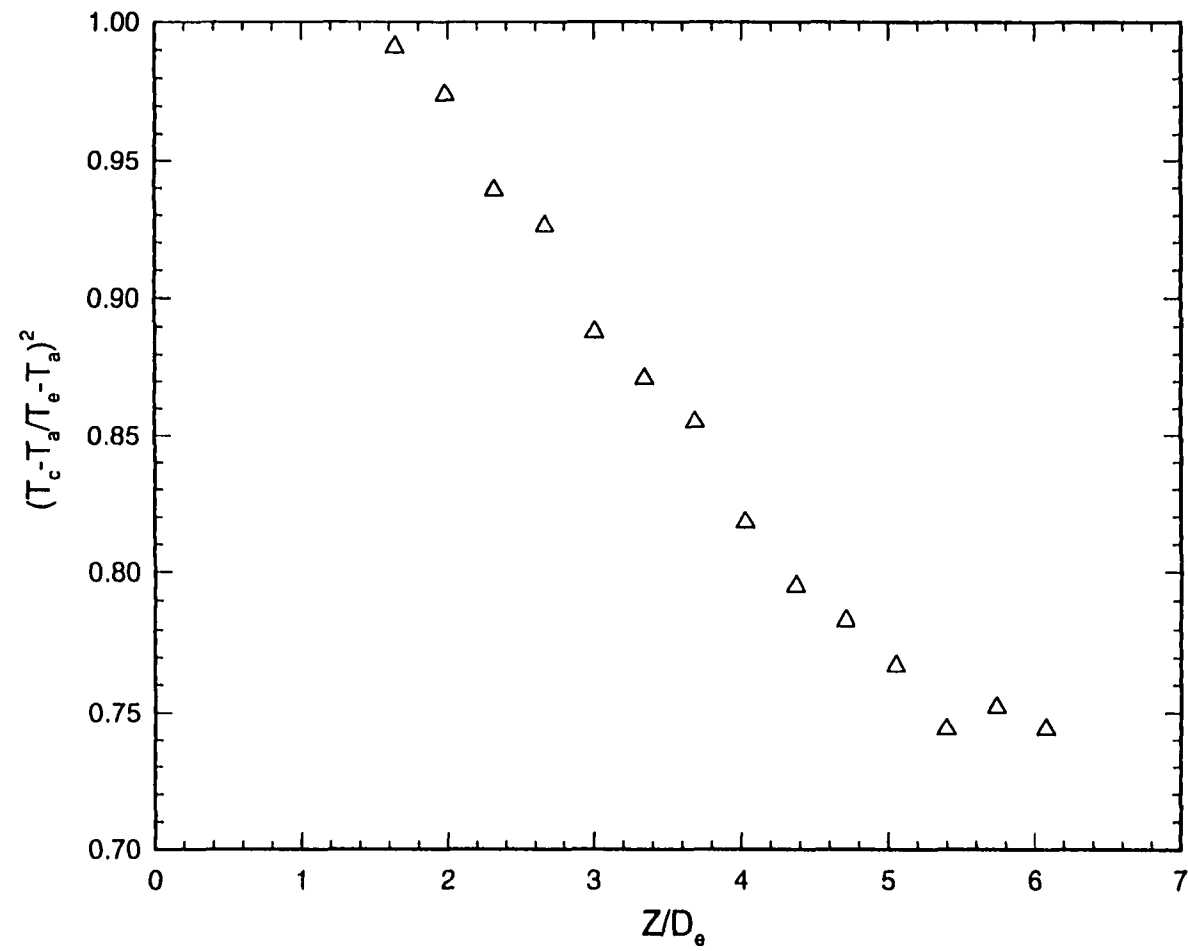


Figure5.22a Plot of decay of centerline temperature

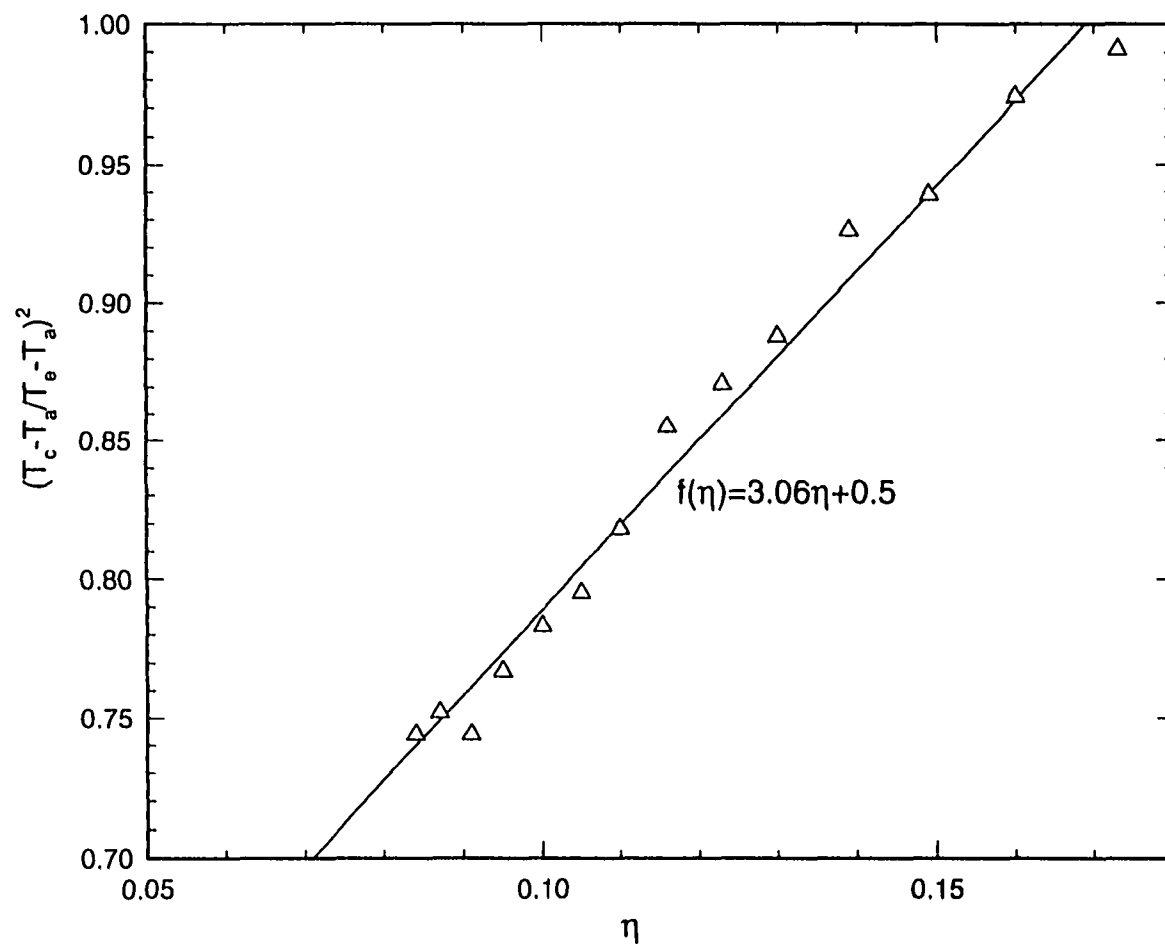


Figure5.22b Temperature decay fitted to equation suggested by Sfeir (1976).

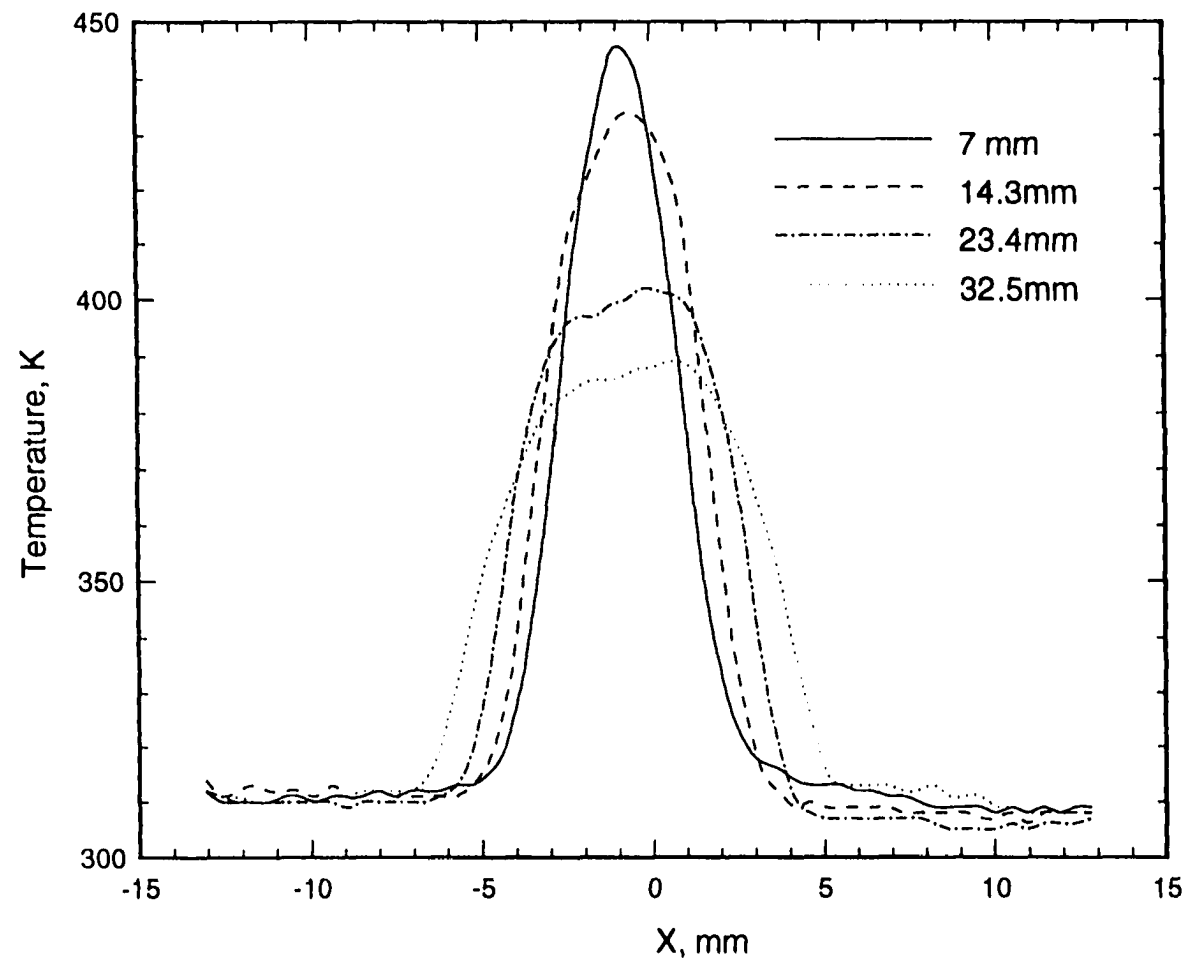


Figure 5.23a Temperature profiles across several z-locations for major axis.



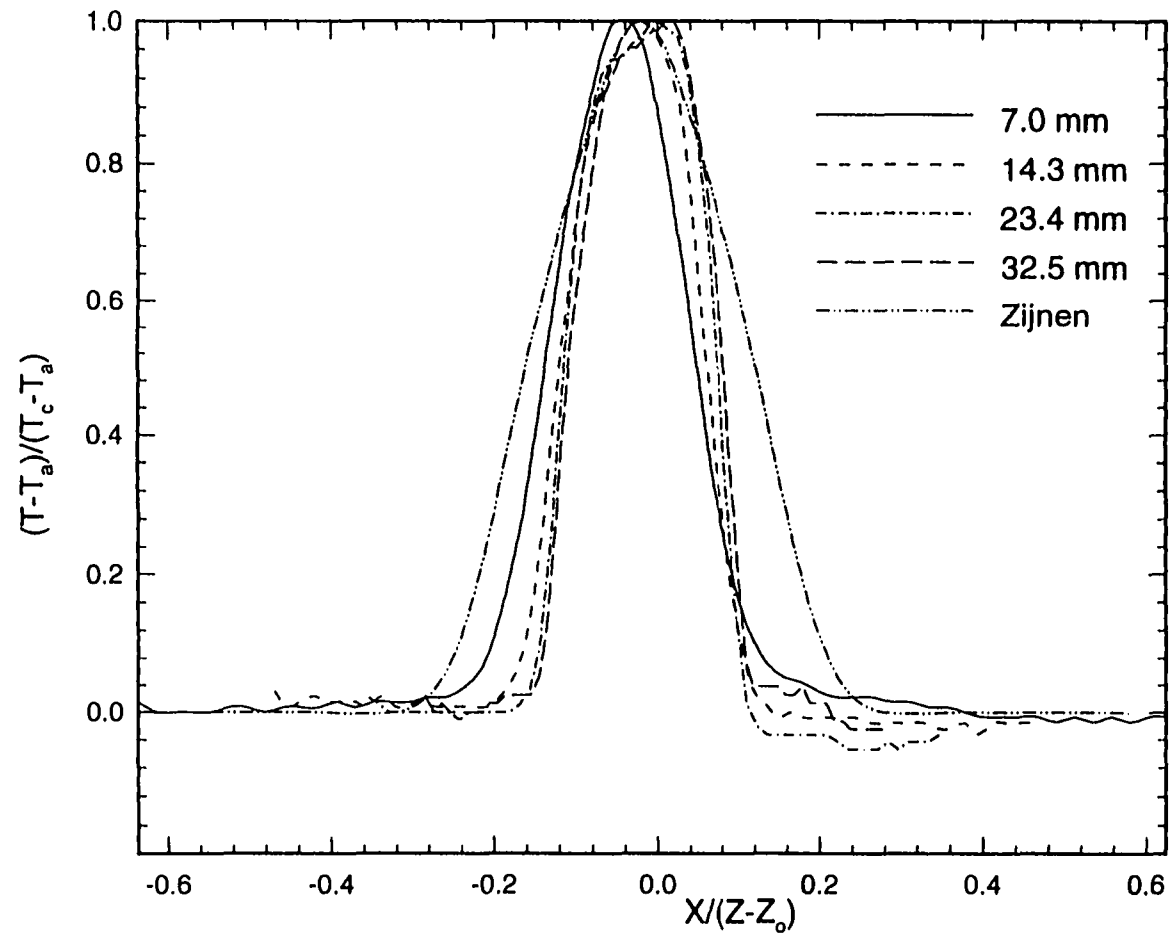


Figure5.23b Non-dimensionalized temperature profiles across several z-locations for major axis. Non-dimensionalized by similarity parameters.

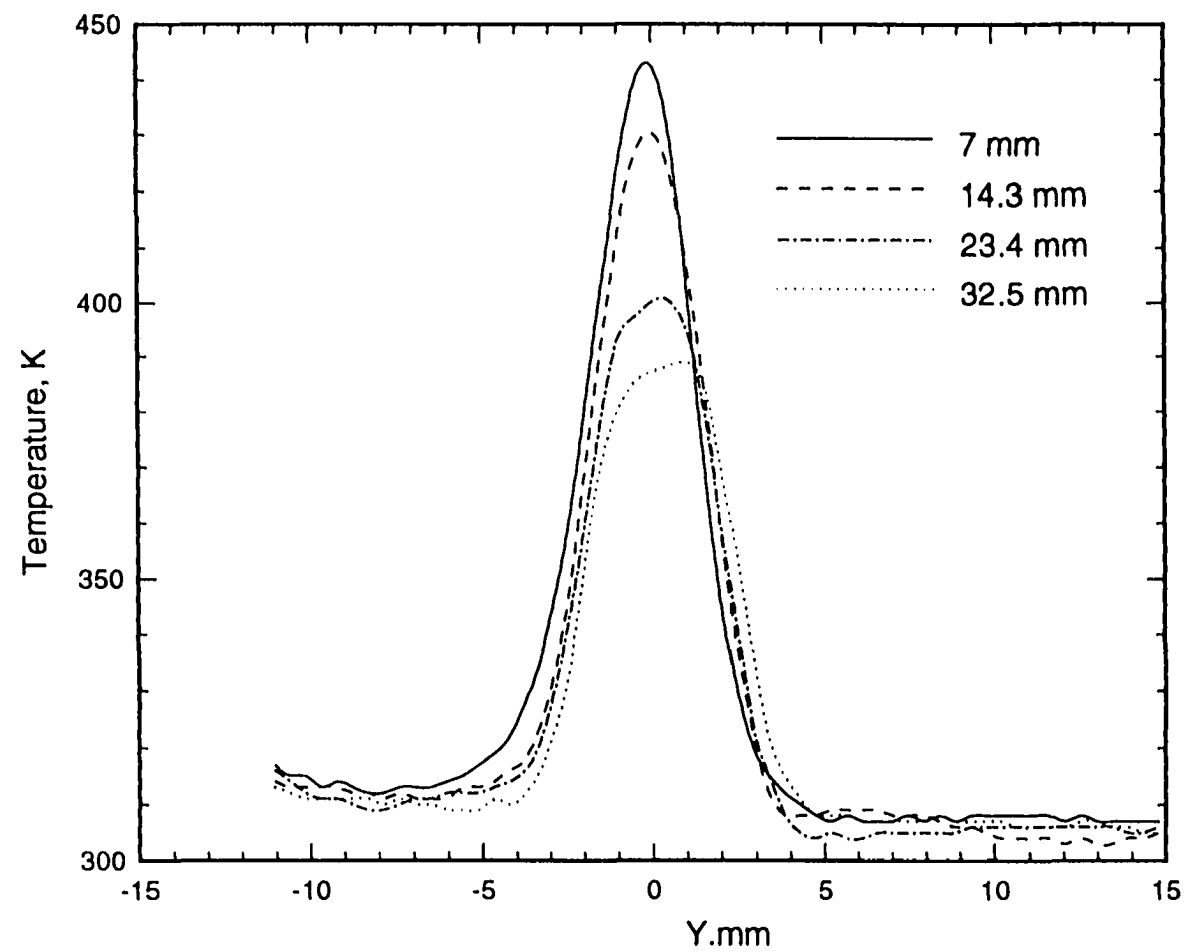


Figure 5.24a Temperature profiles across several z-locations for minor axis

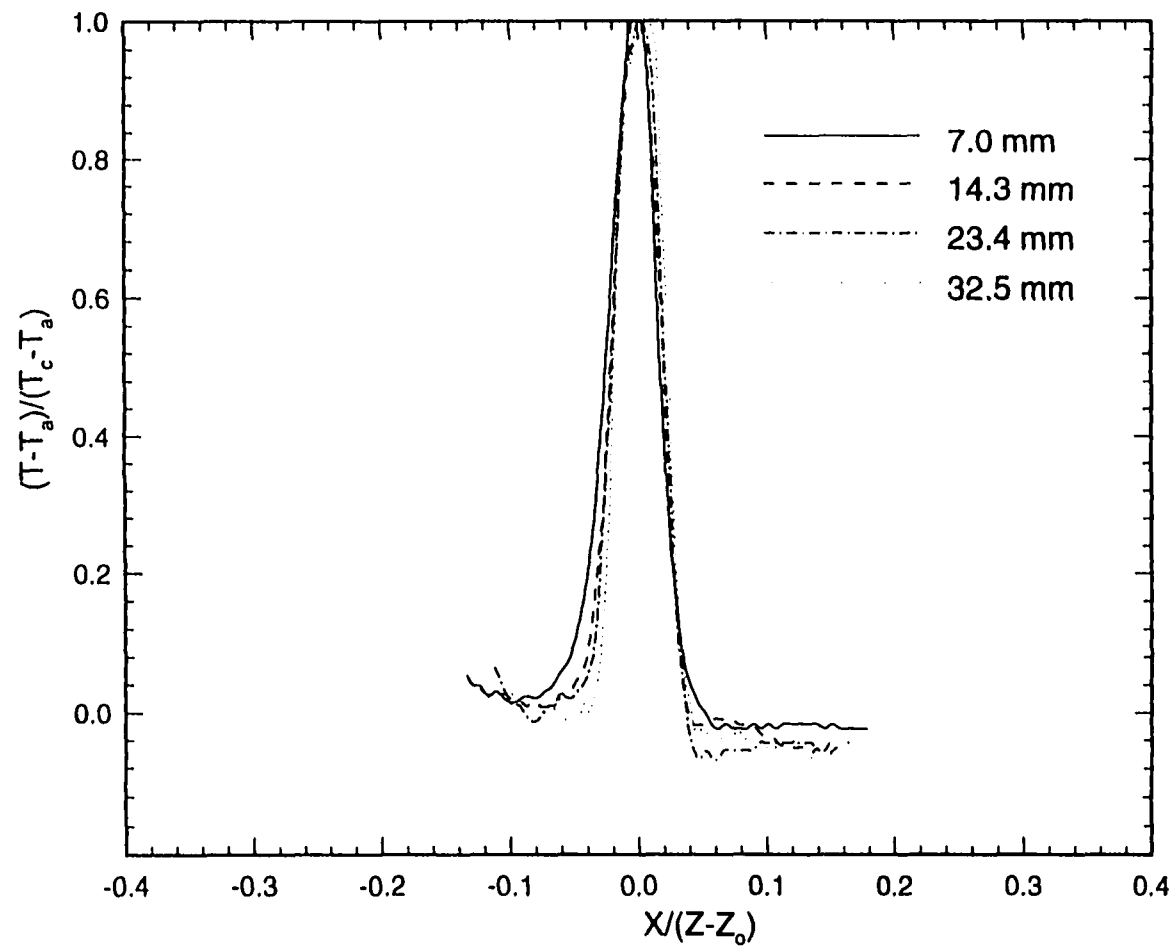


Figure 5.24b Non-dimensionalized temperature profiles across several  $z$ -locations for minor axis. Non-dimensionalized by similarity parameters.

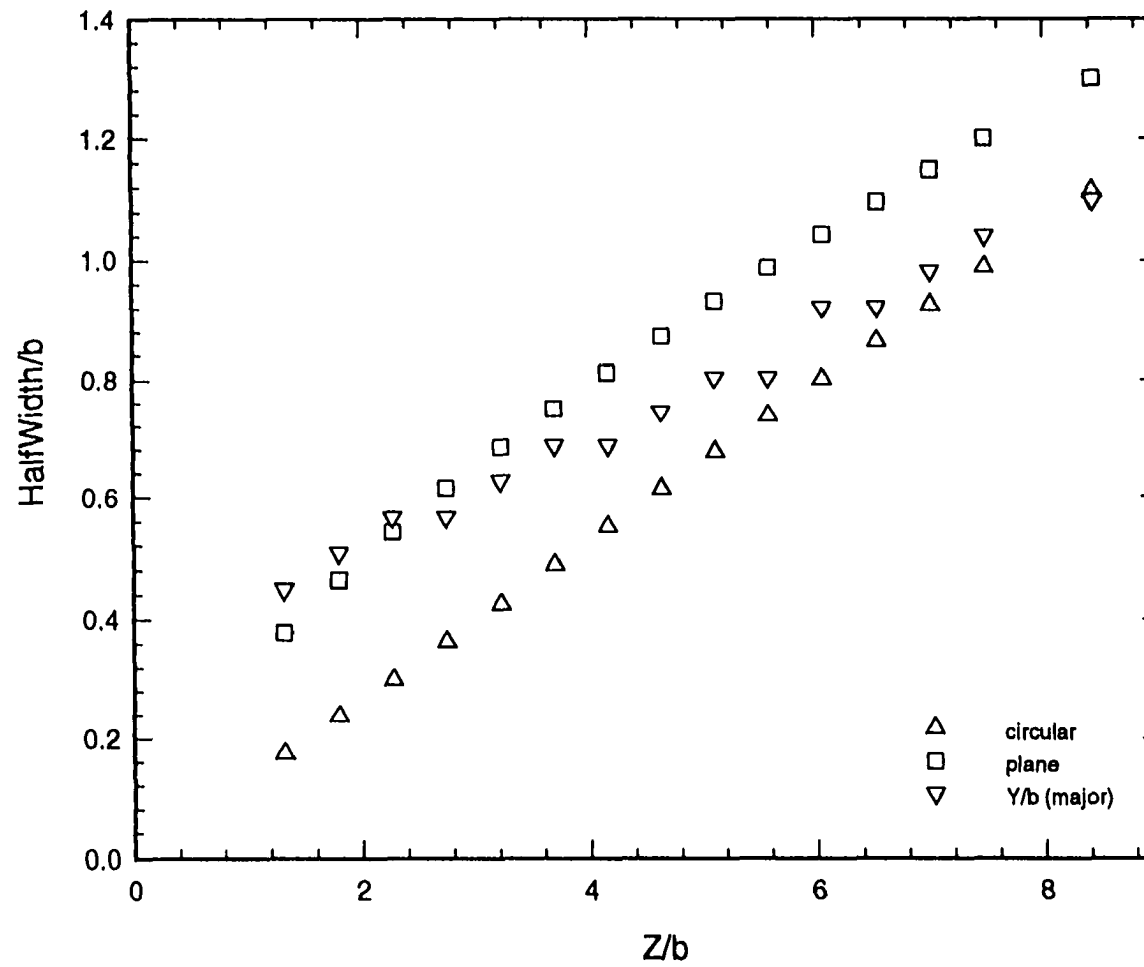


Figure5.25 Comparison of growth rate of round jet, plane jet and present rectangular jet.

## **Chapter 6**

### **CONCLUSIONS AND RECOMMENDATIONS**

We have demonstrated an application of the rainbow schlieren technique for measurements of temperature in 3-D flow fields. The tomographic algorithm of convolution-backprojection modified for beam deflection measurements was successfully used to invert the data measured by rainbow schlieren. The technique was tested on an axisymmetric heated air jet. The results of the temperature reconstructions above the axisymmetric jet at several axial locations were shown to agree with thermocouple measurements to within experimental errors. The agreement validated the technique which could be used for measurements in a variety of flow processes with refractive index gradients.

The technique was successfully used for measurements of temperature in an asymmetric flow field created by an inclined heated air jet. The flow field was 3-D and the data acquired by the rainbow schlieren technique was successfully inverted using beam deflection tomography. The results were shown to agree with thermocouple measurements at various locations. We have also shown that the technique could be used to nonintrusively study the evolution of a physical phenomenon.

A discussion of the evolution of the laminar heated rectangular jet has been presented. The temperature profiles along the minor and major planes of the rectangular jet were shown to agree with thermocouple measurements within the experimental

errors. We have shown that the trend of the development of the laminar jet was consistent with published results on three dimensional jets. It was found that the spreading rate of the thermal shear layer of the jet in the plane of the major axis was higher than that in the plane of the minor axis.

It is recommended that this work be extended to study turbulent flows. To do this it will be necessary to acquire multiple images simultaneously. Since the number of these images will be limited, the ART algorithm (which is suitable for limited view data) could be used to invert the measured data. When using the ART reconstruction algorithm, the rays need not be parallel. The ray paths can be integrated into the algorithm via ray tracing techniques. In this way the normal Z configuration of the schlieren arrangement can be used with non off-axis mirrors.

Also, to take advantage of higher sensitivity of mirror based schlieren systems (longer focal lengths), the fan-beam reconstruction algorithm should be tested with data obtained from fan beam schlieren arrangements as described by Schardin (1942). With mirror systems, wider fields of view are possible than with lens systems. With fan beam rays through a test object, it is not necessary to have specially designed off-axis mirrors (designed to create parallel rays).

The rainbow schlieren technique can be applied to generally asymmetric fields. The optical arrangement of the system is highly flexible and can be modified to suit a particular application. The technique can be used, for example, to study, wakes, mixing layers, and hostile combustion environments.

## REFERENCES

1. Antonia, R.A., Rajagopalan, S., and Fululachier, L., 1984, "Comparison of Temperature and Velocity Spectra in a Slightly Heated Turbulent Plane Jet," *AIAA Journal*., Vol. 22, pp. 311-313.
2. Attal-Tretout, B., Bouchardy, P., Magre, P., Pealat, M. and Taran, J.P., 1990, "CARS in Combustion: Prospects and Problems," *Applied Physics Section B*, Vol. 50, pp. 445-447.
3. Blevins, R.D., 1984, *Applied Fluid Dynamics Handbook*, Van Nostrand Reinhold Company, Princeton, New Jersey.
4. Brand, R.S. and Lahey, F.J., 1967, "The Heated Laminar Vertical Jet," *Journal of Fluid Mechanics*, Vol. 29, part 2, pp. 305-315.
5. Butuk, N. and Gollahalli, S.R., 1996, "Effects of Heating on Two Dimensional Mixing Layers," *ASME/API Emerging Energy & Technology, Energy Week Conference & Exhibition*, January 29th-31st, Houston, Texas.
6. Censor, Y., 1983, "Finite Series Expansion Reconstruction Methods," *Proceedings of the IEEE*, Vol. 71, No.3, pp. 409 - 418.
7. Crow, S.C. and Champagne, F.H., 1971, "Orderly Structures in Jet Turbulence," *Journal of Fluid Mechanics*, Vol. 48, pp. 547-591.
8. Dasch, C. J., 1992, "One-Dimensional Tomography: A Comparison of Abel, Onion-Peeling, and Filtered Backprojection Methods," *Applied Optics*, Vol. 31, pp. 1146-1152.
9. Deans, S.R., 1983, *The Radon Transform and Some of its Applications*, John Wiley & Sons, New York.
10. Decker, A.J., 1994, "Tomographic Methods in Flow Diagnostics," in *Optical Diagnostics for Flow Processes*, (L. Lading, G. Wigley, and P. Buchhave, Eds.), Plenum Press, New York, pp. 337-353.
11. Dixon-Lewis, G., 1954, "Temperature Distribution in Flame Reaction Zones," *4th Symposium (International) on Combustion*, pp. 263-265.
12. Dudgeon, D.E. and Mersereau, R.M., 1984, *Multidimensional Digital Signal Processing*, Prentice-Hall, New Jersey.

13. Dufong, S., Shaohua, C., Wang, R., and Xudong, X., 1995, "An Automatic Image Processing System and Fast-Reconstruction Techniques for Holographic Interferometry Computer Tomography," *Applied Optics*, Vol. 34, pp. 3064-3068.
14. Eckbreth, A.C. "Recent Advances in Laser Diagnostics for Temperature and Species Concentration in Combustion," *18th Symposium (International) on Combustion*, pp. 1471-1487.
15. Eckbreth, A.C., Dobbs, G.M., Stufflebeam, J.H., and Tellex, P.A., 1984, "CARS Temperature and Species Measurements in Augment Jet Engine Exhaust," *Applied Optics*, Vol. 23, pp. 1328 - 1339.
16. Ekstrom, M.P., 1984, *Digital Image Processing Techniques*, Academic Press, New York.
17. Emmerman, P.J., Goulard, R., Santoro, R.J., and Semerjian, H.G., 1980, "Multiangular Absorption Diagnostics of a Turbulent Argon - Methane Jet," *Journal of Energy*, Vol. 4, No.2, pp. 70 -77.
18. Everett, W.K. and Robins, G.A., 1978, "The Development and Structure of Plane Jets," *Journal of Fluid Mechanics*. Vol. 88, pp. 563-584.
19. Faris, G.W., 1986, *Quantitative Optical Tomographic Imaging of Fluid Flows and Flames*, Ph.D Dissertation, Stanford University, Stanford, California.
20. Farrel, P.V. and Hofeldt, D.L., 1984, "Temperature Measurement in Gases Using Speckle Photography," *Applied Optics*, Vol. 23, pp. 1055-1059.
21. Farris, G.W. and Byer, R.L., 1988, "Three Dimensional Beam Deflection Optical Tomography of a Supersonic Jet," *Applied Optics*, Vol. 27, pp. 5202-5212.
22. Fristrom, R.M., 1995, *Flame Structure and Processes*, Oxford University Press, New York.
23. Gebhart, B., 1986. *Heat Transfer*, McGraw-Hill Book Company, New York.
24. Givi, P., 1989, "Model Free Simulations of Turbulent Reactive Flows," *Progress in Energy and Combustion Science*, Vol. 15, No.1, pp. 31-37.
25. Goldstein, R.J. and Kuehn, T.H., 1996, "Optical Systems for Flow Measurement: Shadowgraph, Schlieren, and Interferometric Techniques," in *Fluid Mechanics Measurements*, (R.J., Goldstein, Taylor and Francis, Eds.), Washington DC.
26. Gordon, R., Bender R., and Herman, G. T., 1970, "Algebraic Reconstruction Techniques (ART) for Three-Dimensional Electron Microscopy and X-ray Photography," *Journal of Theoretical Biology*, Vol. 29, pp. 471-481.



27. Gouldin, F.C., Schefer, R.W., Johnson, S.C., and Kollamann, W., 1986, "Nonreacting Turbulent Mixing Flows," *Progress in Energy and Combustion Science*, Vol. 12, pp. 257-303.
28. Greenberg, P.S., Klinel, R.B., and Buchele, D.R., 1995, "Quantitative Rainbow Schlieren Deflectometry," *Applied Optics*, Vol. 34, pp. 3810 -3822.
29. Grinstein, F. F. and Kailasanath, K., 1995, "Three-Dimensional Numerical Simulations of Unsteady Reactive Square Jets," *Combustion and Flame*, Vol. 100, pp. 2-10.
30. Hall, E.L., 1979, "*Computer Image Processing and Reconstruction*," Academic Press, New York.
31. Hall, R.J. and Bouczyk, P.A., 1990, "Sooting Flame Thermometry Using Emission/Absorption Tomography," *Applied Optics*. Vol. 29 pp. 4591-4598.
32. Hanson, R.K., Seitzman, J. M., and Paul, P.H., 1990, "Planar Laser Fluorescence Imaging of Combustion Gases," *Applied Physics Section B*, Vol. 50, pp. 441-454.
33. Heffernan, P.B., and Robb, R. A., 1985, "Non-destructive Testing," *Applied Optics*, Vol. 24, pp. 4105-4109.
34. Herman, G.T., 1980, "*Image Reconstruction From Projections: The Fundamentals of Computer Tomography*," Academic Press, New York.
35. Hesselink, L., 1988, "Digital Image Processing in Flow Visualization," *Annual Review of Fluid Mechanics*, Vol. 20 pp. 421-485.
36. Hiller, B. and Hanson, R.K., 1988, " Simultaneous Planar Measurements of Velocity and Pressure Field in Gas Flows Using Laser Induced Fluorescence," *Applied Optics*, Vol. 27, pp. 33-48.
37. Ho Chih-Ming and Gutmark, E., 1987, "Vortex Induction and Mass Entrainment in a Small Aspect-Ratio Elliptic Jet," *Journal of Fluid Mechanics*, Vol. 179, pp. 383-405.
38. Holman, J.P., 1994, *Experimental Methods for Engineers*, Sixth Edition, McGraw Hill, New York.
39. Howes, W.L., 1984, "Rainbow Schlieren and its Applications," *Applied Optics*, Vol. 23, pp. 2449 - 2460.
40. Hughey, B.J. and Santavicca, D.A., 1982, "A Comparison of Techniques for Reconstructing Axisymmetric Reacting Flow Fields from Absorption Measurements," *Combustion Science and Technology*, Vol. 29 pp. 167-190.

41. Hussain, F. and Hussain, H.S., 1989., "Elliptic Jets part 1. Characteristics of Unexcited and Excited Jets," *Journal of Fluid Mechanics*, Vol. 208, pp. 257-320.
42. Kak, A.C. and Slaney, M.,1988, *Principles of Computerized Tomographic Imaging*, IEEE Press, New York.
43. Kamal, A.,1995, *Turbulent Diffusion Gas Jet Flames from Circular and Elliptic Nozzles*, PhD. Dissertation, University of Oklahoma, Norman, Oklahoma.
44. Kanury, M.A.,1975, *Introduction to Combustion Phenomenon*, Gordon and Breach Science Publishers, New York.
45. Karen, E., Bar-Ziv, E., Glatt, I., and Kafri, O.,1996, "Measurements of Temperature Distribution of Flames by Moire Deflectometry," *Applied Optics.*, Vol. 20, pp. 4263-4266.
46. Kohse-Honinghaus, K.,1990 "Quantitative Laser-Induced Fluorescence: Some Recent Developments in Combustion Diagnostics," *Applied Physics Section B.*, Vol. 50, pp. 455-461.
47. Krothapalli, A., Baganoff, D., and Karamcheti, K., 1981, "On The Mixing of a Rectangular Jet," *Journal of Fluid Mechanics*, Vol. 107, pp. 201-220.
48. Kwoh, Y.S. and Reed, I.S.,1977,"A Generalized 1 $\omega$ 1-Filter for 3-D Reconstruction," *IEEE Transactions on Nuclear Science*, NS-24, No. 5, pp. 1990-1998.
49. Kwoh, Y.S., and Reed, I.S.,1977, "Backprojection Speed Improvement for 3-D Reconstruction," *IEEE Transactions on Nuclear Science*, NS-24, No. 5, pp.1999-2005.
50. Lapp, M. and Penney, C.M.,1977, "Raman Measurements in Flames," in *Advances in Infrared and Raman Spectroscopy*, (R.J.H. Clark, and R.E. Hester, Eds.), Hayden and Sons Ltd. London, pp. 204-210.
51. Laurendeau, L. A.,1991, "Temperature Measurements by Light Scattering Methods," in *Combustion Measurements*, (N. Chigier Ed.), Chapter 4. Hemisphere, Washington DC.
52. Lira, I.,1995, "Measurements of an Axisymmetric Temperature Field by Speckle Photography Methods," *Experiments in Fluids*, Vol. 20, pp. 100-105.
53. McGuirk, J. J. and Rodi, W., 1977, "The Calculation of Three-Dimensional Turbulent Free Jets," in *Turbulent Shear Flows I* (F. Durst, B.E. Launder, F.W. Schmidt, and J. H. Whitelaw, Eds.), Springer Verlag, New York.

54. Mersereau, R. M. and Oppenheim, A.V.,1974, "Digital Reconstruction of Multidimensional Signals from their Projectons," *Proceedings of the IEEE*, Vol. 62, No.10, pp. 1319-1338.
55. Merzkirch, W., 1987, *Flow visualization*, Academic Press, New York.
56. Mewes, D. and Fellholter, A.,1995, "Mixing Processes in Fluids," in *Process Tomography: Principles Techniques and Applications*, (R. A.William. and M. S. Beck, Eds.), Butterworth, New York, pp. 487-508.
57. Meyer- Arendt, J. R., 1984, *Introduction to Classical and Modern Optics*, Printice - Hall Inc., New Jersey.
58. Miller, R.S., Madnia, C.K., and Givi, P.,1995, "Numerical Simulations of Non-Circular Jets," *Computers and Fluids*, Vol. 24, No.1, pp. 1-25.
59. Oppenheim, B.E.,1977, *Reconstruction Tomography From Incomplete Projections*, University Park Press, Baltimore, Maryland, pp. 155-183.
60. Pai, S. I., 1954, *Fluid Dynamics of Jets*, D. Van Nostrand Company Inc., Princeton, New Jersey.
61. Peters, T.M.,1981, "Algorithms for Fast Back and Re-Projection in Computer Tomography," *IEEE Transactions On Nuclear Science*, Vol. NS-28, No. 4, pp. 3641-3643.
62. Ramachandran, G. N. and Lakshminarayanan, A.V.,1971,"Three-Dimensional Reconstruction from Radiographs and Electron Micrographs: Applications of Convolutions instead of Fourier Transforms," *Proceeding of the National Academy of Sciences, USA* Vol. 68, pp. 2236-2240.
63. Ray, S.R. and Semerjan, H.G., 1984, "Laser Tomography for Simultaneous Concentration and Temperature Measurement in Reacting Flows," in *Combustion Diagnostics by Non Intrusive Methods: Progress in Astronautics and Aeronautics*, Vol. 92, (T.D. McCoy, and J.A. Roux, Eds.), pp. 490-501.
64. Rubinstein, R. and Greenberg, P.S., 1994, "Rapid Inversion of Angular Deflection Data for Certain Axisymmetric Refractive Index Distributions," *Applied Optics*, Vol. 33 pp.1141 -1144.
65. Santoro, R.J., Semerjian, H.G., Emmerman, P.J., and Goulard R., 1981, "Optical Tomography for Flow Field Diagnostics," *International Journal of Heat and Mass Transfer*, Vol. 24, No. 7, pp. 1139 - 1150.
66. Schadow, K.C., Gutmark, E., and Parr, T.P., 1984, "Study of Combusion Dynamics for Passive and Active Control," in *Combustion Diagnostics by Non Intrusive*

- Methods: Progress in Astronautics and Aeronautics*, Vol. 92, (T.D. McCoy, and J.A. Roux, Eds.), pp. 339-444.
67. Schardin, H., 1942, *Schlieren Methods and Their Applications*, NASA TT-F-12731, (Apr. 1970), [Translation from *Ergeb.Exakten Naturewiss* 20, 303].
  68. Schlichting, H., 1968, *Boundary Layer Theory*, McGraw Hill, New York.
  69. Semerjian, H.G., Santoro, R.J., Gouland, R., and Emmerman, P.J., 1981, "Optical Tomography for Diagnostics in Combusting Flows," in *Fluid Mechanics of Combustion Systems*, (T. Morel, R.P. Lohman, and J.M. Rackley, Eds.), ASME, New York, pp. 119-129.
  70. Settles, G.S., 1985, "Color-Coding Schlieren Techniques for the Optical Study of Heat and Fluid Flow," *International Journal of Heat and Fluid Flow*, Vol. 6, pp. 3-15.
  71. Sfeir, A. A., 1976, "The Velocity and Temperature Fields of Rectangular Jets," *International Journal of Heat and Mass Transfer*, Vol. 19, pp. 1289-1297.
  72. Shepp, L.A., and Logan, B.F., 1974, "The Fourier Reconstruction of a Head Section," *IEEE Transactions on Nuclear Science*, Vol. NS-21, pp. 228-236.
  73. Snyder, R. and Hesselink, L., 1984, "Optical Tomography for Flow Visualization of the Density Field Around Revolving Helicopter Rotor Blade," *Applied Optics*, Vol. 23, pp. 3650-3656.
  74. Snyder, R. and Hesselink, L., 1988, "Measurement of Mixing Fluids Flows with Optical Tomography," *Optics Letters*, Vol. 13, pp. 87-91.
  75. Song Yaozu, and Guo Z., 1993, "Application of Laser Speckle Photography in Study of Convective Heat Transfer," in *Optical Diagnostics in Fluid and Thermal Flow*, (S.S. Cha, and J.D. Trolinger, Eds.), Proceedings SPIE the International Society for Optical Engineering, San Diego, California.
  76. Steiglitz, K., 1974. *An Introduction to Discrete Systems*, John Wiley and Sons New York.
  77. Stricker, J, Keren, E, and Kafri, O., 1983, "Axisymmetric Density Field Measurements Using Moire Deflectometry," *AIAA Journal*, Vol. 21 pp. 1767-1769.
  78. Stricker, J., 1984, "Analysis of 3-D Phase Objects by Moire Deflectometry," *Applied Optics*, Vol. 23, pp. 3657-3659.

79. Sweeney, D.W. and Vest C. M., 1973, "Reconstruction of 3-D Refractive Index Fields from Multidirectional Interferometric Data," *Appl. Opt.* vol 12 pp2649- 2664
80. Tarasov, S.B. and Toleuov, G., 1993, "Heat Transfer Processes in Coherent Structures in Three-Dimensional Jets," *Heat Transfer Research*, Vol. 25, No.3, pp. 352-355.
81. Vasil'ev, L.A., 1971, *Schlieren Methods*, Keter Publishers, London.
82. Verhoeven, D., 1993, "Limited-Data Computed Tomography- Algorithms for the Physical Sciences," *Applied Optics*, Vol. 32, pp.3736-3754.
83. Vest, C.M., 1979, *Holographic Interferometry*, John Wiley and Sons, New York.
84. Weaver, H.J., 1983, *Application of Discrete and Continuous Fourier Analysis*, John Wiley and Sons, New York.
85. Weinberg, F.J., 1963, *Optics of Flames*, Butterworth Inc., Washington DC.
86. William, C.S. and Becklund, Q. A., 1972, *Optics A short Course for Engineers and Scientists*, Wiley-Interscience, New York.
87. Williams, R.A. and Beck, M.S., (eds), 1995, "*Process Tomography: Principles Techniques and Applications*," Butterworth, New York.
88. Xie, C.G., 1995, "Image Reconstruction" in *Process Tomography: Principles Techniques and Applications*, (R. A. William, and M. S. Beck, Eds.), Butterworth, New York.
89. Zijnen Van Der Hegge, B.G., 1958, "Measurement of the Distribution of Heat and Matter in a Plane Turbulent Jet of Air," *Applied Science Research. Section A*, Vol. 7 pp. 277-292.

## APPENDIX A.1

### Sample Calculation of Error:

For a point the following temperatures were reconstructed from 10 images: 415, 398, 387, 395, 414, 384, 421, 399, 406, and 386K. From these we calculate:

$$mean = 400.5 K$$

$$std. deviation, \sigma = 13.10$$

$$c = \pm \frac{t\sigma}{\sqrt{n}}$$

$$= \pm \frac{2.228 \times 13.10}{\sqrt{10}}$$

$$= 9.23$$

## APPENDIX A.2

### Calculation of Grashof Number (Gr.) of Rectangular Jet:

The Grashof number is defined as:

$$Gr = \frac{g\beta\rho^2 z^3 \Delta T}{\mu^2}$$

where

- g      the gravitational constant
- $\beta$       coefficient of thermal expansion
- $\rho$       density
- z      distance downstream of jet exit
- $\Delta T$     temperature deficit
- $\mu$       viscosity

The table below shows the calculation of Gr at various locations downstream of the rectangular jet:

Label	Z,m	Tmax, K	Tc-Ta, K	mean, T, K	beta(1/T)	Grashof #
1	0.00146	451	141	380.5	0.003	21.072
2	0.00511	441	131	375.5	0.003	850.581
3	0.00694	445	135	377.5	0.003	2184.171
4	0.00877	449	139	379.5	0.003	4514.329
5	0.01059	445	135	377.5	0.003	7760.614
6	0.01242	437	127	373.5	0.003	11903.353
7	0.01425	434	124	372	0.003	17624.416
8	0.01607	425	115	367.5	0.003	23729.005
9	0.0179	421	111	365.5	0.003	31826.295
10	0.01973	417	107	363.5	0.003	41309.698
11	0.02155	408	98	359	0.003	49918.882
12	0.02338	402	92	356	0.003	60347.981
13	0.02521	399	89	354.5	0.003	73499.385
14	0.02703	395	85	352.5	0.003	87014.041
15	0.02886	389	79	349.5	0.003	99279.662
16	0.03068	391	81	350.5	0.003	121942.322
17	0.03251	389	79	349.5	0.003	141913.012

### APPENDIX A.3

#### Reconstruction Algorithm:

$P(\theta, t)$  projections;  $b(\theta, t)$  convolved projections;  $\tilde{n}(x, y)$  reconstruction;  $N$  number of view angles;  $M$  number of rays in each projection.

1. Initialize  $\tilde{n}(x, y) = 0$
2. For each view angle do  
    Begin
3. Calculate  $P(\theta, t)$  for  $t = 1, M$   
    End
4. For each view angle do  
    Begin
5. Pass  $P(\theta, t)$  through the convolution function to find  $b(\theta, t)$
6. For each  $(x, y)$  do:  
    Begin
7.  $\tilde{n}(x, y) = \tilde{n}(x, y) + b(\theta, y \cos \theta - x \sin \theta)$  (b found by interpolation)  
    End
- End
8. For each  $(x, y)$  do:  
    Begin
9.  $\tilde{n}(x, y) = (1/N - 1) * \tilde{n}(x, y)$   
    End
10. Stop



## APPENDIX A.4

### Derivation of the light ray deflection angle equation

The path of the light ray in the  $xy$  plane is given by the following equation as discussed in Chapter 3:

$$\frac{\partial^2 y}{\partial x^2} = \frac{1}{n} \frac{\partial n}{\partial y}$$

The total angular deflection in the  $y$  direction at the exit of the test section can be determined as follows: For small deflections, it can be shown that the angle of the light beam as it traverses the test section is the slope  $\partial y/\partial x$  [Goldstein (1996)]. If this angle is denoted  $\epsilon'$  then the above equation can be integrated within the test section limits to obtain

$$\epsilon' = \int \frac{1}{n} \frac{\partial n}{\partial z} dx$$

Now at the interface of the test object and the surrounding, the light ray will undergo an additional deflection. If  $\epsilon$  is the angle of the light beam after it has exited the test section, then from Snells's law

$$n_o \sin \epsilon = n \sin \epsilon'$$

where  $n_o$  is the refractive index of the air surrounding the test object, and  $n$  that in the test object. Thus for small angles

$$\epsilon = \frac{n \epsilon'}{n_o}$$

and on substituting for  $\epsilon'$  from above we obtain

$$\epsilon \simeq \frac{1}{n_v} \int \frac{\partial n}{\partial y} dx \quad (3.1)$$

## APPENDIX A.5

### Sample Calculations

Below is shown the steps used in the calculation of temperature of the heated jets. The center point of the round jet will be used to show sample calculations. From Fig. 5.1a, hue at the center point is 279.5 degrees. When the calibration curve (Fig. 3.2), is used this corresponds to a y position on the filter of 0.97mm. The background hue is 277 degrees which gives a y position of 0.96mm on the filter. Therefore,

$$\Delta y = 0.01mm$$

Equation 3.2 gives the relationship between deflection angle and displacement distance on the filter plane

$$d = \Delta y = f_c \tan \epsilon \simeq f_c \epsilon \tag{A.5.1}$$

$$\epsilon = \frac{\Delta y}{f_c}$$

$$= \frac{0.01}{490}$$

$$\simeq 2.04 \times 10^{-5} \text{ radians}$$

This value is the same as that shown in Fig. 5.1b. Now using equation 3.25

$$\frac{n - n_o}{n_o} = \tilde{n}(x, y) = \sum_{n=1}^N \frac{\pi}{N-1} \sum_{m=1}^M \epsilon(ma, \frac{n\pi}{N-1}) q(y \cos \theta - x \sin \theta - ma) a \tag{A.5.2}$$

for N=50 views and M=278 rays, the normalized refractive index difference was calculated by the reconstruction program. The results are shown in Fig. 5.1c. The center point normalized refractive index difference was evaluated as  $-4.8 \times 10^{-5}$ .

To evaluate the temperature, the Gladstone-Dale relation of equation 3.28 was used.

$$n - 1 = K\rho \quad \text{A.5.3}$$

where  $K$  is the Gladstone-Dale constant and  $\rho$  is the density. For background refractive index we have

$$n_o - 1 = K\rho_o$$

and for the refractive index within the jet

$$n - 1 = K\rho$$

Dividing these two equations we obtain:

$$\frac{n_o - 1}{n - 1} = \frac{\rho_o}{\rho} \quad \text{A.5.4}$$

Since

$$T \sim \frac{1}{\rho}$$

we have

$$\frac{T}{T_o} = \frac{n_o - 1}{n - 1} \quad \text{A.5.5}$$

From the reconstruction equation A.5.2 we obtain  $n - n_o/n_o$ , this is related to  $n - 1$  by

$$n - 1 = n_o - 1 + \frac{n - n_o}{n_o}(1 + n_o - 1)$$

For air at  $T=288\text{K}$  and  $0.5097\mu\text{m}$  wavelength, the Gladstone-Dale constant is given as  $K=0.0002274 \text{ m}^3/\text{kg}$  [Merzkirch (1987)].

$$n_o - 1 = 0.0002274m^3/kg \times 1.202kg/m^3$$

$$=0.0002733$$

Substituting in equation A.5.5 we obtain the center temperature T as

$$T = \frac{320 \times 0.0002733}{0.0002733 + -4.8 \times 10^{-5}(1 + 0.0002733)}$$

$$=388.2K$$

This is shown in Fig. 5.1d.

## APPENDIX A.6

### Uncertainty Analysis

Given a function  $f$  of several experimentally measured independent variables  $f=f(x_1, x_2, x_3, \dots, x_n)$ , the variables  $x_1, x_2, x_3, \dots, x_n$  are subject to uncertainty. If these uncertainties are known, then the uncertainty in the result  $f$  can be evaluated using the equation [Holman (1994)]:

$$w_f = \left[ \left( \frac{\partial f}{\partial x_1} w_1 \right)^2 + \left( \frac{\partial f}{\partial x_2} w_2 \right)^2 + \dots \left( \frac{\partial f}{\partial x_n} w_n \right)^2 \right]^{\frac{1}{2}} \quad \text{A.6.1}$$

where  $w_f$  is the uncertainty in the result and  $w_i$  ( $i=1..n$ ) are the uncertainties in the independent measured variables.

This procedure is to be applied to determine the uncertainty in temperature measurements obtained by the rainbow schlieren technique. To do this, we need to consider the equations used in evaluating the temperature. The procedure of obtaining temperature was described in Chapter 3 and the results discussed in Chapter 5. The key parameter that was measured using the rainbow technique was the deflection angle. This was then used to evaluate the refractive index from which the temperature was calculated using the Gladstone-Dale relation of equation 3.28.

The deflection angles were measured using the hue calibration curve shown in Fig. 3.2 and equation 3.2

$$d = \Delta y = f_c \tan \epsilon \simeq f_c \epsilon \quad \text{A.6.2}$$

The refractive index was calculated from equation 3.25 written below as:

$$\frac{n - n_o}{n_o} = \bar{n}(x, y) = \sum_{n=1}^N \frac{\pi}{N-1} \sum_{m=1}^M \epsilon\left(ma, \frac{n\pi}{N-1}\right) q(y\cos\theta - x\sin\theta - ma)a \quad \text{A.6.3}$$

The temperature was determined from

$$T = T_o \frac{n_o - 1}{n - 1} \quad \text{A.6.4}$$

where

$$n - 1 = n_o - 1 + \bar{n}(1 + n_o - 1)$$

Using equations A.6.2, A.6.3 and A.6.4, the uncertainties in the measurements of temperature was determined as described below.

First the uncertainty in measuring the deflection angle, using the filter calibration curve (Fig. 3.2) was determined. During filter calibration, the filter was translated laterally in the y-direction in equal increments across its entire width. At each step of translation, an image of the undisturbed test section was captured at the recording plane (CCD camera). The hue that was transmitted by the filter and recorded corresponded to the hue on the filter, covering an area equivalent to the size of the slit source at that particular y position. This transmitted hue which is assigned to the current y position on the filter, is obtained by averaging the hue of all the pixels in the recorded image covering an appropriate central area on the image; see Fig. A.6.1 below.

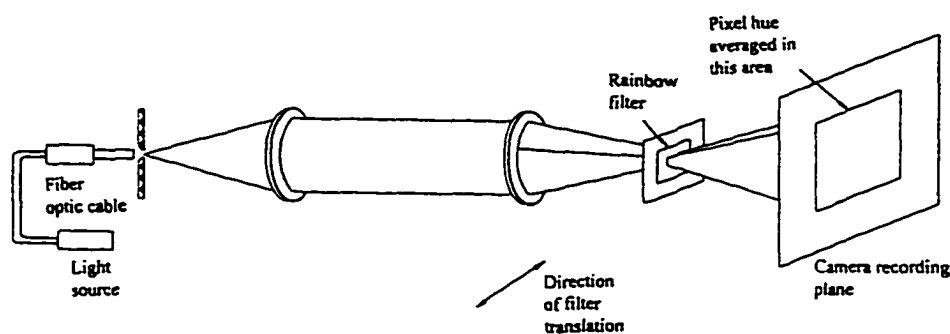


Figure A.6.1 Filter calibration showing the area of hue averaging at the recording plane.

Ideally the hue that is recorded at each translation step should be uniform. In practice this is not so because of fluctuations attributable to the light source and also fluctuations in the spatial transmissivity function of the filter. When the mean of all the pixel hues in the recorded image covering an appropriate central area of the image is calculated, the standard deviation is also calculated over the same area of the image at each y position. The standard deviation gives us a measure of the non-uniformity in the hue. This standard deviation is a useful parameter when evaluating the performance of the rainbow schlieren apparatus. At each y-position on the filter the standard deviation represents the minimum distance, a light ray will have to be deflected in order to measure an unambiguous change in the value of the hue. In other words this is the least count of the rainbow schlieren apparatus [Greenberg (1995)].

Figure A.6.2 below is a plot of the standard deviations of the hue as a percentage of full scale hue at each filter y position. Also shown is the filter calibration curve with hue



plotted in radians. An average standard deviation of 1.11% of full scale is calculated from the plot data;

1.11% of full scale

$$= \frac{1.11}{100} \times 5.6$$

$$= 0.0621 \text{ radians}$$

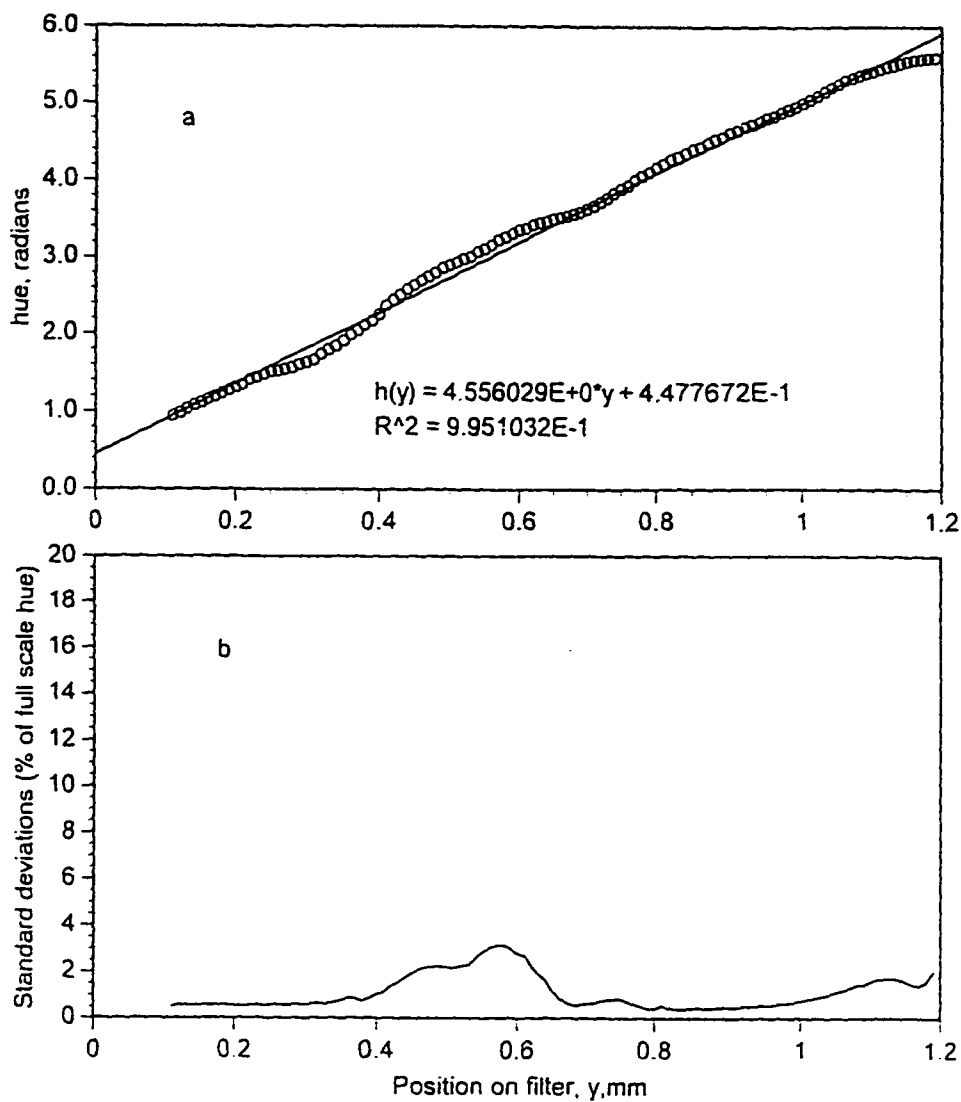


Figure A.6.2 a. Calibration curve b. Plot of standard deviations of the hue as a percentage of full scale hue

The spatial transmissivity function of the filter is given by

$$h = K'y + C'$$

where  $K'$  and  $C'$  are constants. From the calibration curve, the best least squares linear fit equation is given by

$$h = 4.556y + 0.448$$

for a change in hue of 0.0621 radians, a change in  $y$  ( $\Delta y$ ) is calculated as  $\Delta y = 0.013$  mm.

Equation A.6.2 relates deflection angles to deviations on the filter. i.e.

$$y = f_c \epsilon$$

where  $f_c$  is the focal length of the decollimating lens. The deflection angle becomes

$$\epsilon = \frac{y}{f_c} \quad \text{A.6.5}$$

The uncertainty in deflection angle is then:

$$\begin{aligned} \Delta \epsilon &= \left[ \left( \frac{\partial \epsilon}{\partial y} \cdot \Delta y \right)^2 \right]^{\frac{1}{2}} \\ &= \frac{1}{f_c} \cdot \Delta y \end{aligned}$$

$\Delta y$  is the uncertainty in the measurement of  $y$ , which is taken as two times the standard deviation evaluated above.

$$\begin{aligned} \Delta \epsilon &= \frac{1}{490} \cdot 2 \cdot 0.013 \\ &= 0.0000531 \text{ radians} \end{aligned}$$

This is then the uncertainty in determining the deflection angle.

Next consider the reconstruction equation A.6.3 above. This can be broken down into two steps, the convolution step and the backprojection step. The convolution step is

$$b(\theta, t) = \sum_{k=1}^M \epsilon(\theta, t) q(t - k)$$

A.6.6

the uncertainty in  $b(\theta, t)$  is given as

$$\Delta b = \frac{\partial b}{\partial \epsilon} \cdot \Delta \epsilon$$

$$\frac{\partial b}{\partial \epsilon} = \sum_{k=1}^M q(t - k)$$

$$= q(t - 1) + q(t - 2) + \dots$$

$q(t)$  is given by equation 3.23b as

$$q(t) = \frac{1}{\pi^2 t} \sin^2(\pi t \omega_{\max})$$

A.6.7

where  $\omega_{\max} = 1/2a$  and  $a$ =sampling spacing which is 1 pixel. A plot of this function is shown in Figure A.6.3 below. The term in the series with the maximum absolute value is used as an approximate uncertainty estimate [Holman (1994)]. This value is 0.1. A more accurate analysis will require evaluation of the entire series. Even then the value will be less than 0.1.

$$\Delta b = 0.1 \times 5.31 \times 10^{-5}$$

$$\approx 5.31 \times 10^{-6}$$

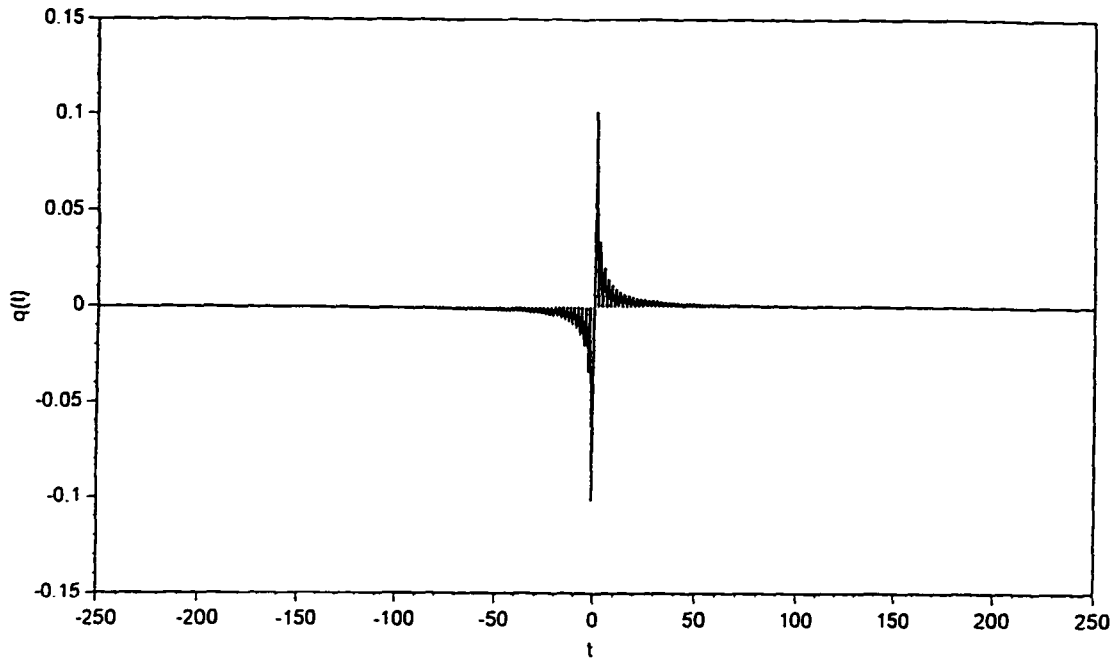


Figure A.6.3 Plot of the convolution function  $q(t)$  vs. distance from center of object in pixels

The backprojection equation is

$$\bar{n} = \frac{\pi a}{N-1} \sum_{n=1}^N b\left(\frac{n\pi}{N-1}, t\right) \quad \text{A.6.8}$$

the uncertainty in refractive index becomes

$$\begin{aligned} \Delta \bar{n} &= \frac{\partial \bar{n}}{\partial b} \cdot \Delta b \\ &= 1 \times 5.31 \times 10^{-6} \\ &= 5.31 \times 10^{-6} \end{aligned}$$

The temperature uncertainty can now be determined. The temperature is obtained from equation A.6.4 above

$$T = T_o \frac{n_o - 1}{n - 1}$$

the uncertainty in temperature is determined as

$$\Delta T = \sqrt{\left(\frac{\partial T}{\partial(n-1)} \Delta \bar{n}\right)^2}$$

$$\frac{\partial T}{\partial(n-1)} = -\frac{T_o \cdot (n_o - 1)}{(n-1)^2}$$

At the center of the round jet, the calculated normalized refractive index ( $\bar{n}$ ) was  $-4.8 \times 10^{-5}$

$$n - 1 = n_o - 1 + \bar{n}(1 + n_o - 1)$$

$$= 2.733 \times 10^{-4} + -4.8 \times 10^{-5}(1 + .0002733)$$

$$= 0.0002253$$

$$\frac{\partial T}{\partial(n-1)} = -\frac{320 \times 0.0002733}{0.0002253^2}$$

$$= -1722928$$

$$\Delta T = 1722928 \times 5.31 \times 10^{-6}$$

$$= 9.148 \text{K}$$

The temperature at the center is calculated as 388K therefore,  $\Delta T/T$  is about 0.023 or 2.3%.

The uncertainties at the other temperatures were calculated as:

normalized index	T, K	$\Delta T, \text{K}$	$\Delta T/T$	%
$-1 \times 10^{-5}$	332	6.7	0.02	2
$-2 \times 10^{-5}$	339	7.24	0.021	2.1
$-3 \times 10^{-5}$	352	7.85	0.022	2.2
$-4 \times 10^{-5}$	380	8.53	0.022	2.2
$-5 \times 10^{-5}$	394	9.31	0.024	2.4



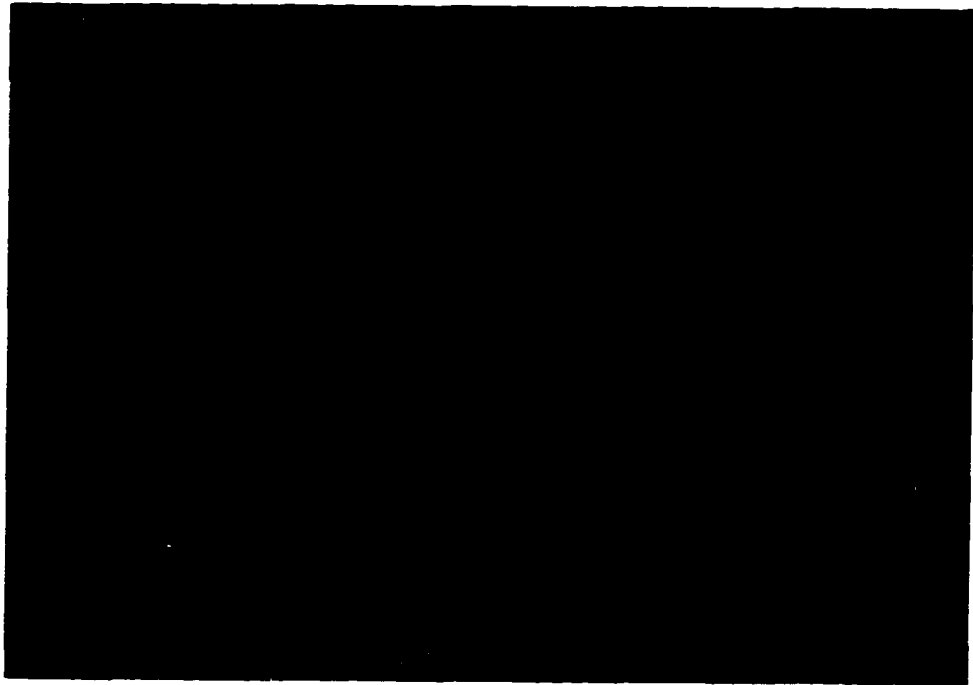
Appendix B.1. Filter hue distribution

← 17.9mm →



Appendix B.2 Schlieren photograph of the round jet

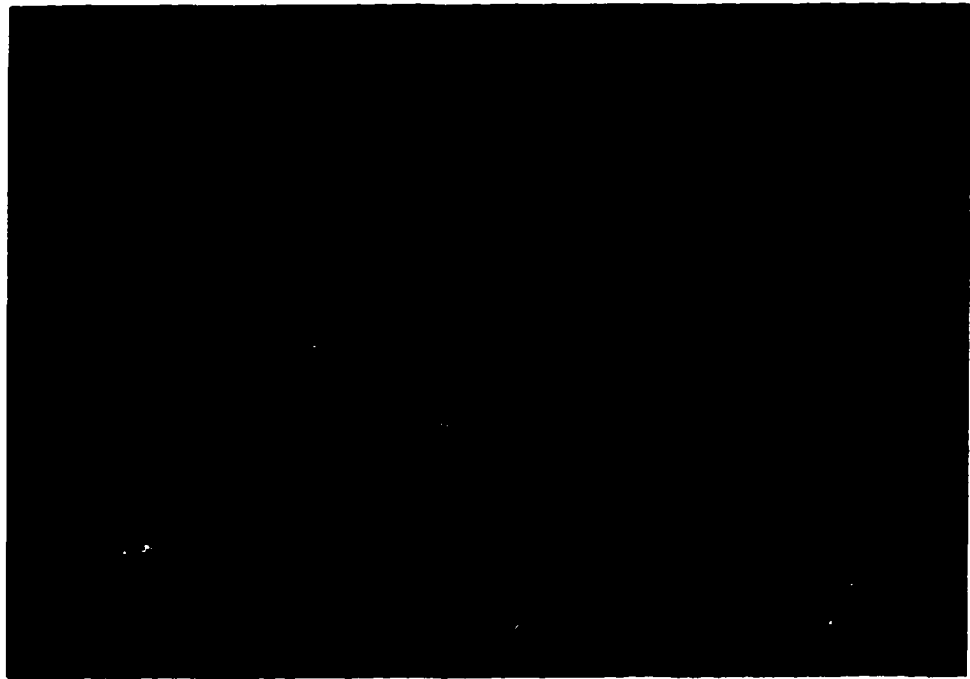
← 17.9mm →



Appendix B.3 The inclined jet at view angles of  $70^\circ$  upper photograph and  $110^\circ$  lower photograph



← 17.9mm →



Appendix B.4 The rectangular jet at view angles of  $0^\circ$  upper photograph and  $90^\circ$  lower photograph